Segmentation of cardiac structures in 3-dimensional echocardiography

Jørn Bersvendsen

Series of dissertations submitted to the
Faculty of Mathematics and Natural Sciences, University of Oslo
No. 1748

ISSN 1501-7710

Cover: Hanne Baadsgaard Utigard.
Print production: Reprosentralen, University of Oslo.

Preface

This thesis is submitted to the Department of Informatics, Faculty of Mathematics and Natural Sciences, University of Oslo, as partial fulfillment of the requirements for the degree of Philosophiae Doctor. The research has been funded by an industrial Ph.D. program at the Research Council of Norway and GE Vingmed Ultrasound. The work was carried out under the supervision of Prof. Eigil Samset at GE Vingmed Ultrasound and the Department of Informatics, University of Oslo, and the co-supervision of Profs. Knut Mørken and Martin Reimers at the Department of Informatics, University of Oslo, between June 2012 and October 2015.

Acknowledgments

I want to thank GE Vingmed Ultrasound and the Research Council of Norway for financing my research through the industrial Ph.D. program, and the Department of Informatics at the University of Oslo for giving me the chance to pursue my Ph.D. The collaboration between industry and academia that I have experienced during my research has been tremendously rewarding.

A special thanks goes to my main supervisor Prof. Eigil Samset. No student could hope for a more engaged and insightful supervisor, and I am grateful for our close collaboration, your thorough discussions and reviews of my work, and for pushing me forward when I needed it. I would also like to thank my co-supervisors Profs. Knut Mørken and Martin Reimers for your insight and discussions of geometrical modeling and guidance during my research.

I have been fortunate to have a large number of colleagues in a wide range of research groups. A special thanks goes to Fredrik Orderud at GE Vingmed Ultrasound for your insight and help with the segmentation framework, Stig Urheim of the Oslo University Hospital for sharing your clinical expertise and always showing a great interest in my research, Raúl San José Estépar at Brigham and Women's Hospital for your support and discussions during my time as a visiting researcher, and finally my great team of colleagues and fellow students at GE Vingmed Ultrasound, University of Oslo, and the Center for Cardiological Innovation.

Last, but certainly not least, I would like to thank my wife Emma Isaksen for her love, support, and great patience throughout my work, as well as my parents Tone and Jim, and my brother Tore Bersvendsen, for their continued encouragement and motivation.

Abstract

Cardiac ultrasound is a key component in modern cardiology, and is widely used to assess and quantify the heart's anatomy and function. In the past two decades, real-time 3-dimensional ultrasound has emerged as a promising modality, allowing a more accurate appreciation of the heart's complex geometry, compared to the more conventional 2-dimensional ultrasound. However, the huge increases in information within volumetric images demand accurate and efficient methods for automatically analyzing and quantifying the heart.

One of the fundamental problems in the processing of cardiac images is segmentation; the process of extracting a geometric model from the image, describing the shape and motion of an anatomical structure. A framework has previously been proposed for solving this problem in 3D ultrasound images, in which the segmentation is expressed as a state-estimation problem and solved with a Kalman filter. This framework is generic, and allows for incorporating different surface representations, image measurements and prior information on shape and motion, and it has been applied to the left ventricle.

The main goal of this thesis has been to apply the existing Kalman filter segmentation framework to different anatomical structures, in particular the aortic root and right ventricle, and to develop a method for biventricular segmentation. Four main contributions have been made.

Firstly, a method providing fully automatic quantification of the aortic valve size from 3D ultrasound images has been developed and its feasibility demonstrated. This is a key measurement to be made prior to procedures on diseased valves, and performing manual measurements is time-consuming and subject to inter-observer variation.

Secondly, two methods have been developed for automated segmentation of the Right Ventricle (RV). Historically, the importance of the RV has been underestimated. Although the RV's role in cardiovascular diseases has been more widely recognized in recent years, few methods for segmentation of the RV have been proposed. Because the RV has a more complex and asymmetrical shape compared to the left ventricle, the existing segmentation framework is not immediately applicable to the RV. Therefore, the method was extended with a geometric model learned from statistical analysis on a set of manual segmentations, as well as prior information on the appearance of the ultrasound images.

Thirdly, one of the two RV methods uses a novel geometric surface representation to simultaneously segment the endocardial and epicardial borders of both ventricles. The surface is parameterized such that myocardial volume conservation is used within the Kalman filter segmentation process, which leads to a much more complete model of the heart and allows one to study the interaction between the ventricles.

Finally, a robust and fully automatic method for spatio-temporal fusion of two ultrasound images has been developed. This is important as it is unrealistic to capture both ventricles in the same imaging sector. Furthermore, the method is able to perform the spatial registration with no assumption on the relationship between the recordings.

Contents

Chapter 1

Introduction

1.1 Background and motivation

Cardiovascular disease is by far the world's most prevalent cause of death, accounting for a staggering 46 % of all deaths in Europe by one estimate [1]. To combat this, there is a clear need for accurate tools to assess the cardiac anatomy and function, in order to perform proper diagnosis and treatment.

Medical imaging is a key component in understanding the state of the patient's heart. Of the available imaging modalities, cardiac ultrasound, or *echocardiography*, has a central role in cardiology, allowing real-time imaging of the beating heart, and offering rapid assessment of anatomy and function. Because ultrasound equipment is portable, comparatively inexpensive, and widely available, echocardiography is often considered the "cardiologist's tool of choice", with a long history of improving the diagnosis and treatment of cardiovascular disease.

The classical ultrasound approach produces an image of the patient's anatomy in a 2-Dimensional (2D) cross section. However, in the early 2000's, Real-Time 3-Dimensional Echocardiography (RT3DE) emerged as a promising technology, allowing the clinician to capture a volumetric 3D image of the patient's anatomy. This technology has since been improving rapidly, and is gaining an important role in clinical practice. A 3D acquisition is, in theory, ideally suited to capture the heart's complex structure and motion, and allows a much more realistic view than the standard 2D approach. However, going from a 2D to a 3D image massively increases the amount of image information. This means that the clinician, to a much larger extent than before, has to rely on the ultrasound system to extract useful information from the images, and to help visualize and quantify the heart.

One of the fundamental problems in the field of medical image processing, and the focus of this thesis, is *image segmentation*. In the context of 3D echocardiography, we will define image segmentation as the extraction of patient-specific surface models, which describe the geometry and motion of anatomical structures, from within the image. These models can then be used for a multitude of purposes, such as calculating the size of the heart's chambers, detecting irregularities in the heart's shape, or assisting visualization

by automatically aligning standard views within the 3D dataset.

A large number of methods have been proposed and validated to solve the segmentation problem for different anatomical structures in 3D echocardiographic images. One of the approaches, which forms the basis for all segmentation methods presented in this thesis, is a Kalman filter state estimation framework presented by Orderud *et al.* [2]–[4]. This is a very generic framework, which can be extended with different mathematical models for the geometry and motion of the target structure, and integrate different types of image measurements.

Most of the cardiac segmentation methods presented in the literature focus on one of the heart's four chambers, the *Left Ventricle* (LV), which can be considered the "main chamber", as it is responsible for pumping blood to the systemic circulatory system. A large parts of this thesis, however, focus on the *Right Ventricle* (RV), which pumps blood to the pulmonary circulatory system. Historically, the importance of this chamber in cardiovascular disease has been underestimated [5], [6], and compared to the LV, studies of the RV are less frequently reported in the literature. However, with the recent advancements in 3D echocardiography, interest in segmentation of the RV is growing.

1.2 Aims of study

The main goal of this thesis has been to apply the existing Kalman filter segmentation framework to different anatomical structures, in particular the aortic root and right ventricle, and to develop a method for biventricular segmentation.

Quantification of the aortic root is of high interest for patients with a diseased aortic valve. In particular, aortic stenosis is a disease where calcification on the valve is preventing proper blood flow out of the heart. For these patients, there are effective surgical and minimally invasive procedures that can be performed to either repair the patient's valve or insert a prosthetic valve. However, these procedures require accurate measurements of the geometry of the valve and its surrounding tissues to be made in advance. This thesis aims to assist such interventions by providing a method for automatic quantitative assessment of the geometry of the aortic root.

Although the existing segmentation framework has been extensively evaluated for the Left Ventricle (LV) [4], [7], it is not immediately applicable to the Right Ventricle (RV), as the RV has a more complex and asymmetrical shape, large inter-patient variation, as well as thinner walls with more pronounced trabeculations. Thus, for the framework to be applied, a suitable surface representation and motion model for the right ventricle must be found.

Although it is known that the heart chambers interact with each other, the vast majority of cardiac segmentation methods presented in the literature operate on a single cardiac structure, most commonly the LV. It is the aim of this thesis to develop a joint segmentation of both the left and right ventricles, which will provide a more complete anatomical description of the heart, as well as allow one to study the interaction between the ventricles. In addition to the challenges present for right ventricle segmentation, two more obstacles must be overcome for a biventricular segmentation. Firstly, since the ven-

tricles share a common wall, the septum, a surface representation must be developed that can express the spatial relationship between the ventricles, and utilize prior information on the physical characteristics of the septum. Secondly, as it is unfeasible to capture both ventricles in the same ultrasound sector, while maintaining adequate spatial and temporal resolution, a registration method must be developed to fused two or more 3D ultrasound sequences together to extend the field of view.

In summary, this thesis aims to:

1. Assist the assessment for aortic valve repair by developing an automatic method to measure the geometry of the aortic root.
2. Extend the existing segmentation framework to provide an automated method for right ventricle segmentation.
3. Extend the segmentation framework with a surface parameterization suitable to represent both the left and right ventricles, and develop an automated biventricular segmentation method.

1.3 Context of the project

This project has been a cooperation between the University of Oslo and GE Vingmed Ultrasound, in an *industrial Ph.D.* program sponsored by the Research Council of Norway. The aim for the industrial Ph.D. program is to bring together the academic and industrial communities, in order to perform applied research that is both academically relevant and lends itself to commercialization. In such a project, there is a balance to be struck between academic and industrial endeavors. Therefore, obtaining clinically applicable solutions has been more central to this thesis than making theoretical contributions. In fact, one of the methods developed in the course of this research (paper I) has already been made commercially available (4D Auto AVQ, GE Vingmed Ultrasound).

The project has also been part of the Center for Cardiological Innovation, a research consortium of academic and industrial partners, sponsored by the Norwegian Research Council and hosted by Oslo University Hospital. Finally, 6 months of the research was spent at the Surgical Planning Laboratory at Brigham and Women's Hospital, Harvard Medical School, in Boston, USA, a laboratory performing research on a wide range of medical image analysis topics.

Chapter 2

Background

This chapter aims to give the relevant background information necessary to understand the research done in this project. Two main topics are discussed; the human heart, including ultrasound imaging of the heart, and segmentation of the heart chambers. Because these are both huge areas of study, this presentation will be limited to information relevant for the papers contained in this thesis, as well as their discussion. However, references to helpful introductions and surveys are given throughout the text.

2.1 The Human Heart

2.1.1 Anatomy

Cardiac chambers

The human heart consists of four chambers; two upper cambers called *atria* and two lower chambers, called *ventricles*. The chambers form two atrium-ventricle pairs, splitting the heart into *left* and *right* sides. In a healthy heart, the left and right sides are separated by a wall, called the *septum*, such that no blood flows directly between the right and left sides. The right ventricle is responsible for pumping blood trough the *pulmonary* circulatory system, where the blood is oxygenated by the lungs and returns to the left atrium. From there, the left ventricle pumps the blood trough the *systemic* circulatory system, feeding the whole body with oxygen and nutrients, and returning to the right atrium to be oxygenated again. An overview of the structure and blood flow or the heart is shown in figure 2.1.

The left and right halves have two valves each, making a total of four, which are used to prevent the blood from flowing in the wrong direction. One set of valves sit between the atria and ventricles, often referred to as the Atrio-Ventricular (A-V) valves, and the other sit between the ventricles and outgoing arteries, called the outflow valves. On the left side, the A-V valve is the *mitral* valve, and the outflow valve is the *aortic* valve. The corresponding valves on the right side are the *tricuspid* and the *pulmonary* valves. All valves

are mostly passive, opening and closing as a result of the pressure differences between the atria, ventricles, and arteries.

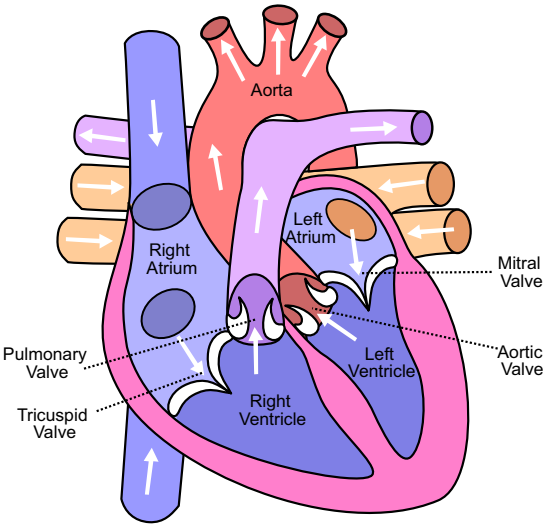

Figure 2.1: Diagram of the heart. The arrows indicate the direction of the blood flow. Image courtesy of Eric Pierce.

Myocardium

The heart's wall is made up of three layers; the *endocardium* which is in direct contact with the blood inside the chambers, the *myocardium* which is made up of the muscle fibers responsible for the actual contraction, and the *pericardium* which envelopes the heart, separating it from surrounding tissues.

The myocardium consists of sheets of muscle fibers that swirl around the ventricles, as illustrated in figure 2.2(a). This structure results in a shortening in the long- and radial axes of the heart when the fibers contract, as well as a torsion around the long axis, as illustrated in figure 2.2(b). The combined effect is a remarkably energy efficient pumping function [8].

2.1.2 Function

Cardiac cycle

During every heartbeat, the heart undergoes two main phases; *systole* and *diastole*. In systole, the ventricles contract, pumping blood into the circulatory systems, while the atrias are filled with blood. In this phase, the outflow valves open, and the A-V valves are

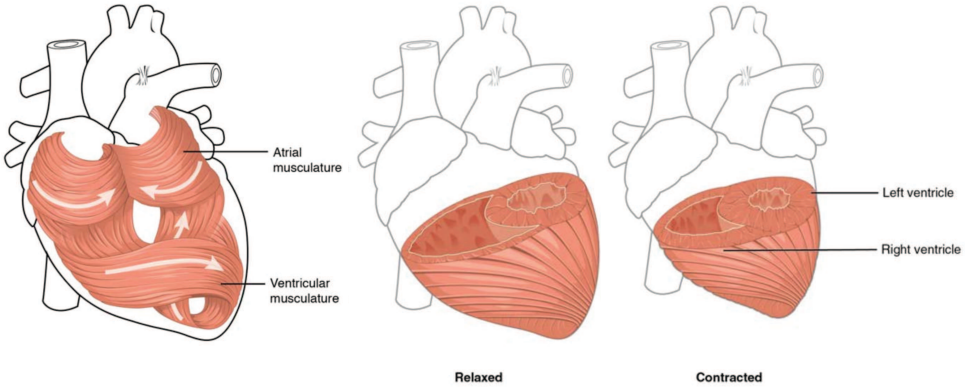

Figure 2.2: Fiber structure of the heart *(a)*, and resulting contraction pattern *(b)*, consisting of longitudinal and radial shortening, as well as circumferential torsion. Images: Betts *et al.* [8].

closed to prevent blood flowing backwards into the atria. Once the ventricles have been emptied, the outflow valves close, as a result of the falling pressure inside the ventricles. The heart then enters diastole, where the A-V valves open and the ventricles are filled with blood from the atrias and relax in preparation for the next heartbeat.

Clinical indicators

In clinical practice, it is necessary to derive some indicators to quantify the global pumping function of the heart. The most common way of quantifying the heart's function is to look at the amount of blood that is pumped with each heartbeat. For both the left and right ventricles, four measurements are widely used for this assessment; End Diastolic Volume (EDV), End Systolic Volume (ESV), Stroke Volume (SV), and Ejection Fraction (EF). EDV and ESV are essentially the maximum and minimum volumes of the ventricle. The SV is the difference between EDV and ESV, which, in a healthy heart with no blood leaks, measures the amount of blood that was actually pumped into the circulatory systems. The EF is a combination of the previous volumes, and measures the amount of blood pumped as a percentage of the EDV,

$$\mathrm{EF} = \frac{\mathrm{EDV}-\mathrm{ESV}}{\mathrm{EDV}} \times 100\% \tag{2.1}$$

$$= \frac{\mathrm{SV}}{\mathrm{EDV}} \times 100\%. \tag{2.2}$$

EF is a very important measurement of global function, and is commonly used as a tool for diagnosis and prediction of adverse events such as heart failure [9].

2.1.3 Differences between the left and right ventricles

It is important to note that the left and right ventricles are not simply mirror images of each other, but are different in shape, function and operating conditions.

Because the Left Ventricle (LV) has to pump blood into the whole body, while the Right Ventricle (RV) only needs to pump blood into the lungs, the LV typically operates at significantly higher pressures than the RV. This results in a thicker myocardium and a simpler, ellipsoid shape, compared to the RV which has a complex crescent shape which "wraps around" the LV [10]. The complex shape makes the RV hard to image, and impossible to appreciate with any single 2D view [9]. Figure 2.3 shows a cross sectional view of the ventricles, illustrating the differences in shape and myocardial thickness of the two ventricles.

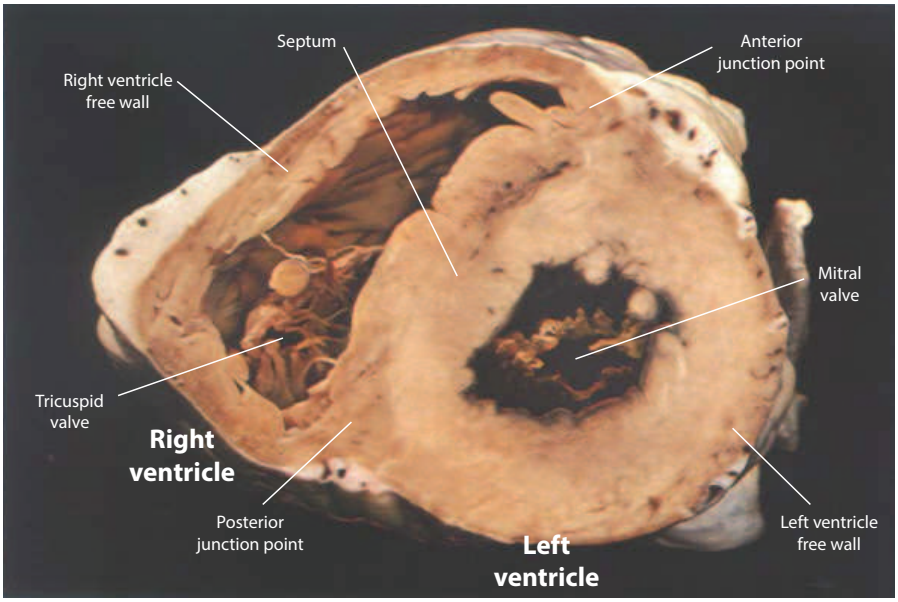

Figure 2.3: Short axis cross section heart, illustrating the differences between the left and right ventricle geometries. Image (unannotated): Anderson *et al.* [11].

Although the ventricles are often considered separately, they certainly interact with each other to perform the pumping function. In fact, it has been demonstrated that about 30 % of the contractile energy of the RV is generated by the LV [12]. Furthermore, the RV relies more heavily on longitudinal shortening to pump blood, and less on the circumferential shortening of the free wall [13].

Since the LV is responsible for the systemic circulation, disease in the left heart is typically more serious. For this reason, the LV has historically received much more attention in the medical literature than the RV [5], [6]. However, in the last decade or two, there

has been a wider recognition of the RV's role in the circulatory system and its impact on cardiovascular disease. In combination with the advancement of 3D medical imaging modalities, making it possible to more accurately appreciate the shape and function of the RV, interest in the right heart, from clinical and technical perspectives, is growing.

2.1.4 Echocardiography

Ultrasound imaging of the heart, known as *echocardiography*, or simply *echo*, is an essential tool used to assess and quantify the heart's structure and function, as well as to perform diagnosis and assist intervention. This section gives a very brief and practical introduction to echocardiography, focusing on the appearance and properties of the ultrasound images, as well as the challenges associated with ultrasound image processing.

Compared to other imaging modalities such as Magnetic Resonance Imaging (MRI) and Computed Tomography (CT), echocardiography has a particular set of benefits resulting in a wide use all over the world. It provides real-time images with a very high frame rate, which is important for assessing the moving heart, and especially the valves. It is also portable, which means that it can be brought to the bed side where the clinician has direct contact with the patient. Finally, it is significantly cheaper than alternative modalities, does not use harmful ionizing radiation, and has essentially no contraindications.

Examples of 3D ultrasound images of the left and right ventricles are shown in figures 2.4 and 2.5.

Image formation

Ultrasound images are generated by transmitting a high-frequency sound wave, way too high in pitch for humans to hear (hence the *"ultra"*), and then record the echoes which are generated when the wave hits anatomical structures within the body. The wave is transmitted and the echoes are recorded all in a single device, called the *transducer*. The transducer is typically a hand-held device placed on the chest of the patient, forming a *Transthoracic Echocardiogram* (TTE). However, specialized transducers exist, that are placed inside the esophagus, forming a *Transesophageal Echocardiogram* (TEE). This modality typically gives higher quality images, as the transducer is closer to the heart, and the sound wave does not have to penetrate the skin.

When the transmitted ultrasound wave hits a local perturbation in tissue characteristics, part of the wave will be scattered, forming an echo traveling back towards the transducer, and part will continue propagating. The transmitted ultrasound beam is focused in a single direction, and the image along this direction is formed by measuring the amount of energy reflected back to the transducer over time. This process is then repeated, with the focus of the ultrasound beam sweeping across the desired image region.

This image formation process is physically limited by the speed of sound, as the transducer has to wait for the wave to propagate to the end of the imaging sector and back, in order to receive the echoes. This means that there is a relationship between the number

of beams fired, i.e. the *spatial resolution* and sector size, and the number of images that can be generated each second, i.e. the *temporal resolution*.

This limitation is very apparent in 3-Dimensional ultrasound, where the transmitted beam has to be swiped over an additional dimension, vastly increasing the time it takes to generate a single frame. Therefore, a compromise has to be made by reducing the spatial and temporal resolution of the 3D image, as well as the sector size. To compensate for this, it is common to perform a *multibeat* acquisition. In such an acquisition, multiple separate and small sectors are acquired from different heartbeats, and then stitched together to form a single 3D image. Because the heart's motion is cyclical, the stitched image will appear as if it was formed from a single heartbeat, with high spatial and temporal resolution. This process can introduce stitching artifacts however, and is only an option if the patient has a steady heart rhythm.

Image processing of echocardiographic images

The nature of ultrasound images poses several challenges for image processing methods. Unlike some modalities, such as X-Ray Computed Tomography (CT), the relationship between ultrasound image intensities and physical tissue properties is very complex. The observed intensities are a combined result of ultrasound reflection, interference and absorption, which means that the absolute gray levels have no inherent physical interpretation. Furthermore, the amount of reflected energy is dependent on the angle between the ultrasound beam and the tissue fiber directions. This means that regions like the myocardium are typically less well-defined in parts of the image where the transducer is parallel to the fibers.

As most echocardiographic images are taken through the thorax, the transducers have to be narrow enough to fit in between the ribs, and the ultrasound beams are spread in a "V shape" in order to cover the heart, as seen in figures 2.4 and 2.5. This means that the image voxels are highly anisotropic, and the image has high resolution in the depth direction, but a low lateral resolution, especially deep into the tissue. Furthermore, the ribs, sternum, and lungs can all give acoustic shadows, causing parts of the image to be empty of information.

Finally, there are several additional image artifacts that are common to observe in ultrasound images, such as reverberations and side-lobes. These make it hard to interpret and process the images without enough prior information on the target anatomical structure.

2.2 Segmentation by state-estimation

2.2.1 The segmentation problem

Segmentation is one of the fundamental problems in image analysis. Fundamentally, the segmentation problem is to separate an image into distinct segments by assigning a *label*

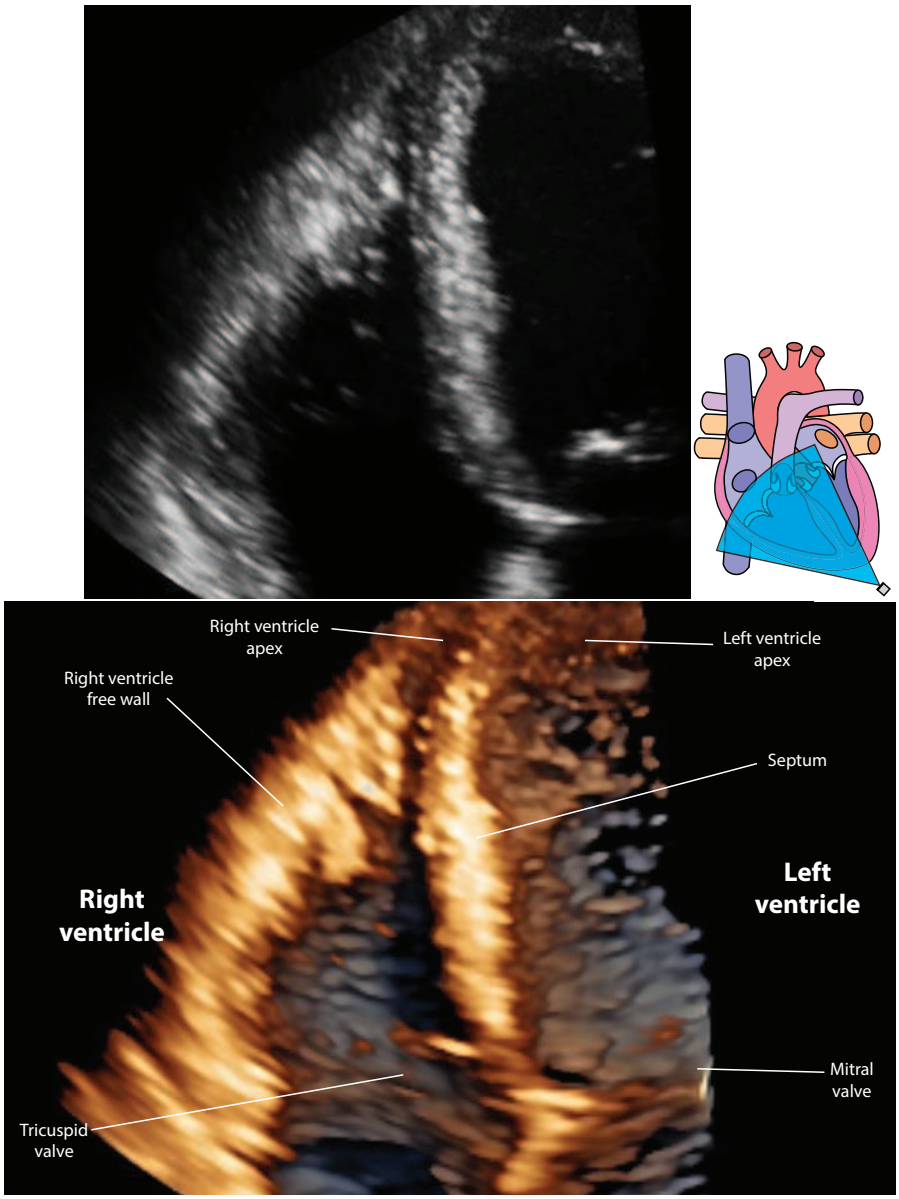

Figure 2.4: 3D ultrasound recording of the right ventricle, taken from an apical position. *Top:* 2D slice through the volumetric data. *Bottom:* 3D rendering of the image.

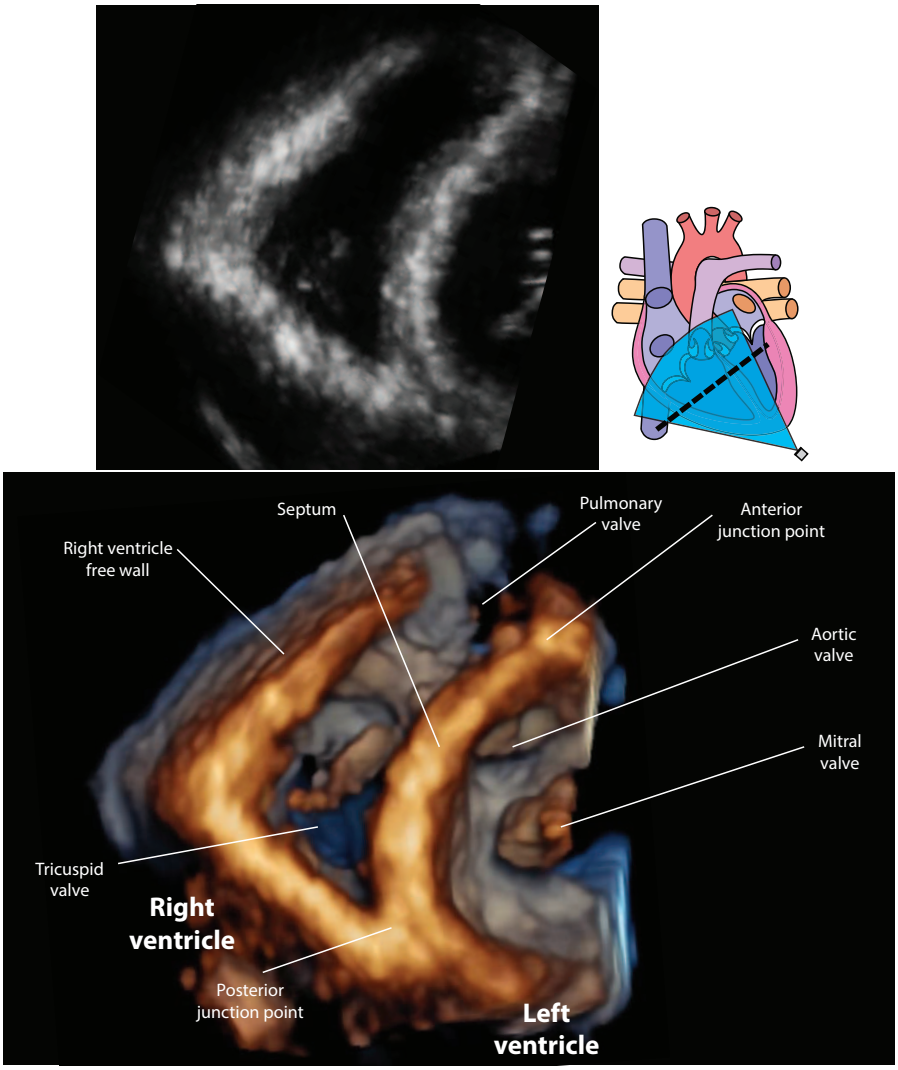

Figure 2.5: Cross sectional view of the same image as in figure 2.4, showing the same view as the figure 2.3. *Top:* 2D slice through the volumetric data. *Bottom:* 3D rendering of the image.

to each pixel. In medical imaging, one typically tries to label parts of the image as belonging to certain organs or anatomical structures, in the case of this thesis the ventricles and myocardium.

A large number of segmentation methods have been proposed and applied for solving different segmentation problems on ultrasound images. This section will focus on the particular segmentation framework used throughout this thesis, and provide background information on its two major components; deformable surfaces and Kalman filters. For a more complete overview of segmentation methods applied in echocardiography and related modalities, the reader is referred to some of the great surveys available on this topic [14]–[17].

2.2.2 Deformable surfaces

A large portion of the echocardiographic segmentation methods presented in the literature can be categorized as using *deformable surfaces*. These methods follow the same overall approach of;

1. declaring a mathematical *model* for the target structure to be segmented, consisting of a *surface representation* and a *deformation space*,

2. identifying certain features of the image, such as strong gradients or clusters of homogeneous appearance, and

3. fitting the model to the image by utilizing the identified feature measurements in some form of a *fitting* algorithm.

One of the reasons for the success of such model-based segmentation methods, compared to simpler image-driven segmentation approaches, is that they allow for a natural incorporation of prior knowledge in a variety of forms, including information on shape, position, orientation, appearance, physiological function, and motion. These priors typically make the deformable surface methods robust to image noise and artifacts, something which is especially important when operating on ultrasound images. However, having a too strong prior can also mean that the model lacks the necessary degrees of freedom to accurately represent the target anatomical structure. This means that there is typically a trade-off to be made between expressiveness of the model and robustness of the segmentation, and a number of surface representations and regularization schemes have been proposed to address this. In this section, a brief overview of different surface types used for ultrasound segmentation is given. For a comprehensive overview of deformable model types, the reader is referred to a more in depth review available on this topic [17], [18].

Model representations

A large number of surface representations have been used for segmentation in ultrasound images, and it is hard to present a complete overview. However, Montagnat *et al.* catego-

rize the most common deformable surfaces into three main categories; discrete meshes, explicit continuous models, and implicit continuous models [18].

Discrete meshes The most common discrete surface is a polygon mesh, which is defined by a set of vertices, edges and faces. Deformation of the mesh is performed by moving the vertices. However, this typically leads to a very large number of degrees of freedom, as it is necessary to introduce a large number of vertices to represent smooth and high-detailed surfaces. It is therefore typically necessary to reduce the deformation space [18], for instance with statistical shape information [19], to provide a well-behaved segmentation.

Non-parametric surface models Non-parametric surfaces, otherwise known as *implicit* surfaces, are formulated by the solution of an implicit function. The most popular implicit surface segmentation method for medical images is the *level-set* method introduced by Osher *et al.* [20]. With this approach, a surface $\mathcal{C}$ is represented as the zero-crossing of a higher-dimensional function ϕ,

$$\mathcal{C} = \left\{ \mathbf{x} \in \Omega \,|\, \phi(\mathbf{x}) = 0 \right\}, \tag{2.3}$$

where $\mathbf{x} \in \Omega$ is a position in the image domain. To fit the model into the image, the implicit surface is evolved from an initial state by minimizing an energy function $E(\mathcal{C})$. This energy function typically contains terms for the global intensities inside and outside the segmented region, as well as some terms used to regularize the surface. These regularization terms can be associated with surface area for smoothing the surface, or associated with an estimation of shape plausibility by statistical knowledge [21]. An example of the level-set framework applied in 3D echocardiography is the approach by Angelini *et al.* for individual segmentation of the left and right ventricles [22]. Historically, the clinical applicability of 3D level-set methods has been limited by their inherent computational complexity. However, Galluzzo *et al.* [23] have demonstrated that this can be mitigated to some extent by combining an efficient GPU implementation of the level-set optimization with a fast explicit deformable surface segmentation [24] for initialization.

Parametric surface models Parametric surfaces, otherwise known as *explicit* surfaces, are defined by a set of shape parameters. In general, the Euclidean position $\mathbf{p} \in \mathbb{R}^3$ of a local point $\mathbf{u} \subset \mathbb{R}^2$ on a parametric surface is given by some explicit function

$$\mathbf{p}(\mathbf{u}) = f(\mathbf{u}, \mathbf{x}), \tag{2.4}$$

where $\mathbf{x}$ is a vector of shape parameters. Examples of parametric surfaces used for ultrasound segmentation include simplex meshes [25], [26], B-spline explicit surfaces [24], active contours[27], and subdivision models [4].

A group of parametric surfaces, called *basis-surfaces*, are parameterized by the position of a set of *control vertices* $\mathbf{q}_i$, such that the surface is given by

$$\mathbf{p}(\mathbf{u}) = \sum_i b_i(\mathbf{u}) \mathbf{q}_i(\mathbf{x}) \tag{2.5}$$

where $b_i(\mathbf{u})$ are the basis functions of the surface. An illustration of such a surface is shown in figure 2.6. Examples of basis-surfaces include B-Spline surfaces and subdivision schemes such as Doo-Sabin [4], [28], Catmull-Clark [29], [30], and Loop [31], [32].

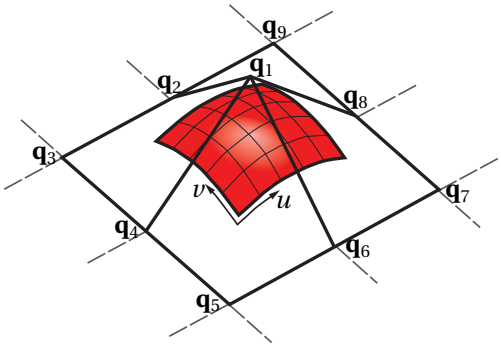

Figure 2.6: Illustration of a basis surface defined by control vertices $\mathbf{q}_1, \mathbf{q}_2, \cdots, \mathbf{q}_9$ (figure III.1 of paper III).

Using a coarse control mesh, one can generate a smooth surface using only a few degrees of freedom, which helps to increase the robustness of the segmentation. Depending on the specific basis functions used, the surface can be made to guarantee continuity of both surface points and normal vectors, leading to a well-behaved segmentation. As with discrete meshes, it is possible to employ different deformation spaces to limit the degrees of freedom of the surface, for instance by statistical learning.

2.2.3 Kalman filter state estimation

The Kalman filter [33] is a fundamental component in state estimation, with applications in numerous technological fields, and is used as a fitting algorithm in the segmentation approach applied in this thesis. Fundamentally, the Kalman filter is a method to estimate the current state of a system, where a subset of the states are measured, in the presence of process and measurement noise.

Original Kalman filter

Process model In the original Kalman filter, the process to be estimated is on the following iterative form, where at time point k, the current state $\mathbf{x}_k$ is given by

$$\mathbf{x}_k = \mathbf{F}_k \mathbf{x}_{k-1} + \mathbf{B}_k \mathbf{u}_k + \mathbf{w}_k \,, \tag{2.6}$$

where $\mathbf{u}_k$ is the control input vector, and $\mathbf{w}_k$ is the process noise. At each time point, a subset $\mathbf{z}_k$ of the state vector is observed,

$$\mathbf{z}_k = \mathbf{H}_k \mathbf{x}_k + \mathbf{v}_k \,, \tag{2.7}$$

where $\mathbf{v}_k$ is the measurement noise. $\mathbf{F}$, $\mathbf{B}$, and $\mathbf{H}$ are time-varying matrices describing the process and observation dynamics. This type of model is known as a continuous hidden Markov model, as the process is "memoryless", i.e. $\mathbf{x}_k|\mathbf{x}_{k-1}, \mathbf{x}_{k-2}, \cdots, \mathbf{x}_0 = \mathbf{x}_k|\mathbf{x}_{k-1}$, and only a subset of the states is observed. A block-diagram of the model is shown in figure 2.7.

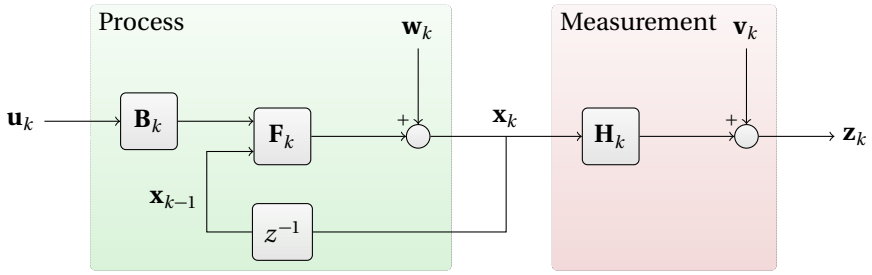

Figure 2.7: Model of the process to be estimated by Kalman filter.

Typically, the process and measurement noises are assumed to be normally distributed with zero mean,

$$\mathbf{w}_k \sim \mathcal{N}(0, \mathbf{Q}_k) \tag{2.8}$$
$$\mathbf{v}_k \sim \mathcal{N}(0, \mathbf{R}_k), \tag{2.9}$$

where $\mathbf{Q}_k$ and $\mathbf{R}_k$ are the process and measurement noise covariance matrices.

Estimation process The Kalman filter estimation pipeline is illustrated in figure 2.8, and figure 2.9 shows a more complete block diagram.

For each new time point, the state is estimated in three stages;

1. a prediction $\hat{\mathbf{x}}_{k|k-1}$ of the current state, called the *a priori* estimate, is calculated based on the model evaluated on the previous estimate $\hat{\mathbf{x}}_{k-1|k-1}$ and current control input $\mathbf{u}_k$,
2. some combinations of the states are measured, and the difference between the measurement vector $\mathbf{z}_k$ and the predicted measurement based on $\hat{\mathbf{x}}_{k|k-1}$ is calculated, called the *measurement residual*,
3. the updated state estimate $\hat{\mathbf{x}}_{k|k}$, called the *a posteriori* estimate, is calculated by combining the prediction and measurements, based on the state and measurement covariance estimates.

With the system specified in (2.6) and (2.8), the prediction step is

$$\hat{\mathbf{x}}_{k|k-1} = \mathbf{F}_k\hat{\mathbf{x}}_{k-1|k-1} + \mathbf{B}_k\mathbf{u}_k \tag{2.10}$$
$$\mathbf{P}_{k|k-1} = \mathbf{F}_k\mathbf{P}_{k-1|k-1}\mathbf{F}_k^\top + \mathbf{Q}_k, \tag{2.11}$$

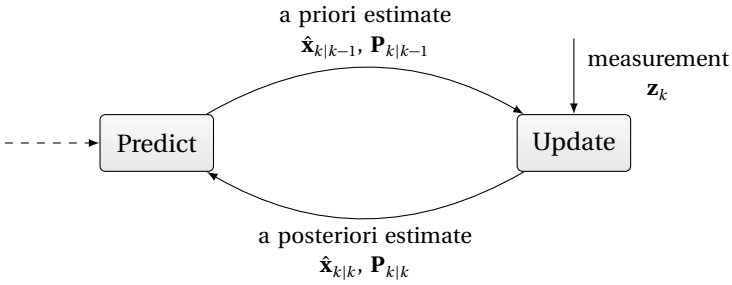

Figure 2.8: Kalman filter estimation loop.

where $\mathbf{P}_{k|k-1}$ is the predicted covariance matrix of the estimate. The measurement vector $\mathbf{z}_k$ is then observed, and the measurement residual $\tilde{\mathbf{y}}_k$ is calculated by

$$\tilde{\mathbf{y}}_k = \mathbf{z}_k - \mathbf{H}_k\hat{\mathbf{x}}_{k|k-1} \tag{2.12}$$

$$\mathbf{S}_k = \mathbf{H}_k\mathbf{P}_{k|k-1}\mathbf{H}_k^\top + \mathbf{R}_k\,, \tag{2.13}$$

where $\mathbf{S}_k$ is the residual covariance. Finally, the prediction and measurement residuals are combined by

$$\mathbf{K}_k = \mathbf{P}_{k|k-1}\mathbf{H}_k^\top\mathbf{S}_k^{-1} \tag{2.14}$$

$$\hat{\mathbf{x}}_{k|k} = \hat{\mathbf{x}}_{k|k-1} + \mathbf{K}_k\tilde{\mathbf{y}}_k \tag{2.15}$$

$$\mathbf{P}_{k|k} = (\mathbf{I} - \mathbf{K}_k\mathbf{H}_k)\mathbf{P}_{k|k-1}\,, \tag{2.16}$$

where the *Kalman gain* $\mathbf{K}_k$ of (2.14) is derived by minimizing the prediction state error in the least squares sense,

$$\mathbf{K}_k = \arg\min_{\mathbf{K}_k} \mathrm{E}\left[\|\mathbf{x}_k - \hat{\mathbf{x}}_{k|k}\|^2\right]. \tag{2.17}$$

Note that this only holds true when the assumptions of the model, e.g. (2.8)-(2.7), are met.

Extended Kalman filter

The *extended Kalman filter* is an extension where the model (2.6)-(2.7) is no longer assumed to be linear. Instead, the model is continuously linearized around the most recent estimate. In general, let the system be on the form

$$\mathbf{x}_k = \mathbf{f}(\mathbf{x}_{k-1}, \mathbf{u}_k) + \mathbf{w}_k \tag{2.18}$$

$$\mathbf{z}_k = \mathbf{h}(\mathbf{x}_k) + \mathbf{v}_k\,, \tag{2.19}$$

The state prediction and measurement residual are calculated directly based on the model,

$$\hat{\mathbf{x}}_{k|k-1} = \mathbf{f}(\hat{\mathbf{x}}_{k-1|k-1}, \mathbf{u}_k) \tag{2.20}$$

$$\tilde{\mathbf{y}}_k = \mathbf{z}_k - \mathbf{h}(\hat{\mathbf{x}}_{k|k-1}), \tag{2.21}$$

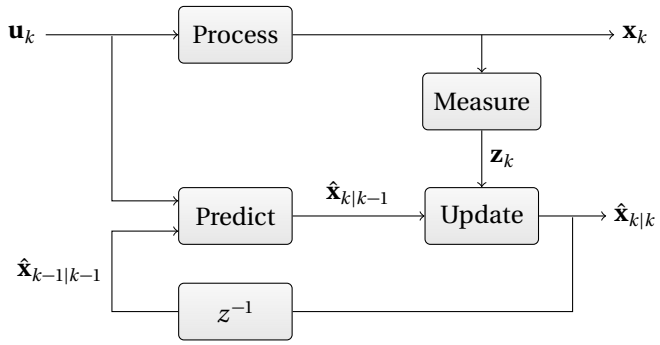

Figure 2.9: Block diagram describing a single iteration of the Kalman filter. The process and measurement blocks are shown in figure 2.7.

and all other steps are the same as in the original Kalman filter (2.12)-(2.16), using a linearization of the model on the form (2.6)-(2.7) where $\mathbf{F}$ and $\mathbf{H}$ are the Jacobian matrices

$$\mathbf{F}_k = \left.\frac{\partial \mathbf{f}}{\partial \mathbf{x}}\right|_{\substack{\hat{\mathbf{x}}_{k-1|k-1} \\ \mathbf{u}_{k-1}}} \tag{2.22}$$

$$\mathbf{H}_k = \left.\frac{\partial \mathbf{h}}{\partial \mathbf{x}}\right|_{\hat{\mathbf{x}}_{k|k-1}} . \tag{2.23}$$

Although other Kalman filter extensions exist to deal with non-linear systems, such as the unscented Kalman filter [34], the extended Kalman filter is a useful and widely used approach for when the Jacobian matrices in (2.22)-(2.23) are known and are a fair approximation.

Information filter

The *information filter* is algebraically equivalent to the Kalman filter, but expressed in a particular form that can be useful in some cases, for instance when the number of measurements are much higher than the number of states. In such systems, the matrix inversion in (2.14) can be problematic as the matrix has dimensions equal to the number of measurements. The information filter is formulated such that an inversion of a matrix with dimension equal to the number of states is required instead.

The prediction step is identical to the original Kalman filter. However, it can be shown [35], [36] that the update step (2.14)-(2.16)can be reformulated to

$$\mathbf{P}_{k|k}^{-1} = \mathbf{P}_{k|k-1}^{-1} + \mathbf{H}_k^\top \mathbf{R}_k^{-1} \mathbf{H}_k \tag{2.24}$$

$$\hat{\mathbf{x}}_{k|k} = \hat{\mathbf{x}}_{k|k-1} + \mathbf{P}_{k|k} \mathbf{H}_k^\top \mathbf{R}_k^{-1} \tilde{\mathbf{y}}_k . \tag{2.25}$$

If one assumes that all measurements are scalar and independent, such that

$$\mathbf{R}_k = \begin{bmatrix} r_{k,1} & 0 & 0 & 0 \\ 0 & r_{k,2} & 0 & 0 \\ & & \ddots & \\ 0 & 0 & & 0 \\ 0 & 0 & 0 & r_{k,N} \end{bmatrix}, \tag{2.26}$$

the form (2.24)-(2.25) simplifies to

$$\mathbf{P}_{k|k}^{-1} = \mathbf{P}_{k|k-1}^{-1} + \sum_{i=1}^{N} \mathbf{h}_{k,i}\, r_{k,i}^{-1} \mathbf{h}_{k,i}^{\top} \tag{2.27}$$

$$\hat{\mathbf{x}}_{k|k} = \hat{\mathbf{x}}_{k|k-1} + \mathbf{P}_{k|k} \sum_{i=1}^{N} \mathbf{h}_{k,i}\, r_{k,i}^{-1}\, \tilde{y}_{k,i}\,, \tag{2.28}$$

where $\mathbf{h}_{k,i}$ is the i'th column of $\mathbf{H}_k$. Note that in this case, the only matrix inversion required is of $\mathbf{P}$, which has dimension equal to the number of states. This is a very computationally efficient method, and trivially extends to any number of independent measurements by simple summation.

Kalman smoother

The Kalman filter assumes a hidden Markov model, meaning that the next state is assumed to be given exclusively by the previous state and current control inputs. Furthermore, it only considers measurements from a single frame at the time. This approach is natural for real-time processing, since the state can be estimated continuously as new data is gathered. In the case of cardiac image segmentation, however, both of these assumptions are slightly misplaced. Firstly, cardiac image sequences are typically recorded over one or more heartbeats, which results in a cyclic motion. Secondly, all frames in the heartbeat sequence are typically available at the time of segmentation, which means that the segmentation could be improved by utilizing more of the available information.

Kalman smoothing is a way of using the Kalman filter such that the state for any frame is estimated on the basis of all available information, from frames before and after. One way of formulating the Kalman smoother is to combine two independent Kalman filters, one iterating forwards over frames $k = 1, 2, \ldots, N$ to produce estimates $\mathbf{x}_{f,k}$ with covariance matrices $\mathbf{P}_{f,k}$, and another iterating backwards over frames $k = N, N-1, \ldots, 1$ producing $\mathbf{x}_{b,k}$ and $\mathbf{P}_{b,k}$. The two estimates can then be assimilated by the maximum likelihood combination [37],

$$\mathbf{P}_k = \left(\mathbf{P}_{f,k}^{-1} + \mathbf{P}_{b,k}^{-1}\right)^{-1} \tag{2.29}$$

$$\hat{\mathbf{x}}_k = \mathbf{P}_k \left(\mathbf{P}_{f,k}^{-1} \hat{\mathbf{x}}_{f,k} + \mathbf{P}_{b,k}^{-1} \hat{\mathbf{x}}_{b,k}\right). \tag{2.30}$$

This smoother will help to enforce a cyclic segmentation, as well as to prevent the segmentation lagging behind the image as a result of temporal regularization.

2.2.4 Segmentation framework overview

The segmentation approach used throughout this thesis is based on a state-estimation framework proposed by F. Orderud [35] and applied to the left ventricle [2]–[4], [7], [27], [38], [39]. In short, this approach performs the segmentation by fitting a parametric deformable surface to the image by combining prior shape information, motion prediction, and edge detection, using a Kalman filter. The framework has been further studied in detail by S. R. Snare who focused on computationally efficient segmentation on pocket-sized ultrasound devices [40], and E. Dikici who focused on improving the edge detection criteria [41].

In this section, a general overview of the framework is presented, focusing on how the framework is applied in this thesis. For reference, an overview of the processing chain is shown in figure 2.10.

Model

In all the segmentation methods proposed in this thesis, a Doo-Sabin subdivision surface [28] is used. This is essentially a generalization of a uniform B-spline for arbitrary topology. The surface is defined by a set of control vertices, and is expressed on the form (2.5). The model is then parameterized by deformation of the control vertices to allow local deformation.

In addition to the local deformation, a global transform is introduced, which includes translation, scaling, and rotation of all the control vertices. This transform is used to place the model in the image, and to capture global movement during the heart cycle.

Initialization

Because the Kalman filter state estimation is an iterative approach, it is important that the initial state of the model is fairly close to the optimal solution. Therefore, the model is aligned in the image before segmentation. This can be done by manually or automatically identifying anatomical landmarks in the image. If the image acquisition is controlled, it may also be safe to assume an initial location and orientation of the model.

Segmentation process

Following the Kalman filter approach, the segmentation is performed iteratively, each iteration consisting of three steps; prediction, measurement, and assimilation.

The prediction step consists of two parts; a regularization towards a known and well-behaved state, and a motion model taking into account the time point within the cardiac cycle.

Measurements are done by sampling 1D image profiles normal to the surface at a number of locations, and detecting edges in the profiles. However, it is also possible to introduce speckle tracking [38] which can capture torsion of the ventricle. For simplicity

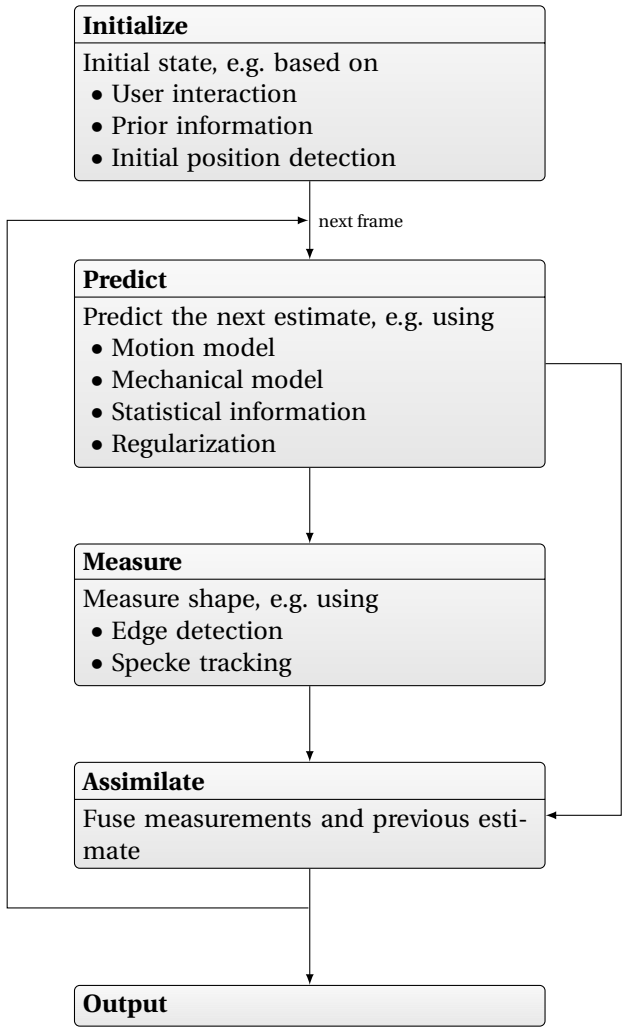

Figure 2.10: Overview of the state estimation processing pipeline.

and computational efficiency, the measurements are assumed to be independent, leading to the assimilation step (2.27-2.28).

Smoothing and two-pass segmentation

The segmentation pipeline is typically run more than once. Firstly, the Kalman smoother (2.29-2.30) is applied to improve the segmentation, and to prevent the model from lagging behind in the cardiac cycle.

Secondly, in order to increase the capture range and robustness of the method, a two-pass segmentation may be introduced. In this approach, the segmentation is run twice, estimating a subset of the states each time. For instance, one can first estimate the global transform states alone, and then estimate the local surface deformations.

Chapter 3

Summary of presented work

I Automatic Measurement of Aortic Annulus Diameter in 3-Dimensional Transoesophageal Echocardiography

Jørn Bersvendsen, Jan O. Beitnes, Stig Urheim, Svend Aakhus and Eigil Samset, *BMC Medical Imaging, 2014,* 14*:31.*

In this paper, we assess the first of the aims of study laid out in section 1.2, by adapting the state estimation segmentation framework of Orderud *et al.* [3], [4] to fully automatically measure the size of the aortic valve. The context of the study is a specific procedure, Transcatheter Aortic Valve Implantation (TAVI), that is done to treat patients with severe Aortic Stenosis (AS), a disease where calcification of the aortic valve is preventing normal blood flow out of the heart. During this procedure, a prosthetic valve is inserted by a catheter, without opening the chest. Because the procedure is minimally invasive, it is a viable option for a large portion of patients that are at too high risk to undergo the conventional open chest surgery.

TAVI requires an accurate measurement of the size of the patient's valve, as inserting a prosthetic valve that is too small can lead to blood leakages, while a valve that is too large can rupture the surrounding tissues [42]. It is well known that conventional 2D echocardiography underestimates the size of the valve, as it fails to appreciate the 3D structure of the valve anatomy [43]–[45]. However, performing measurements on 3D images is both time consuming and subject to inter-observer variation, so an automated tool to assist clinicians is preferred.

Within the state estimation segmentation framework, we use a deformable surface shaped like a cylinder to represent the aortic root and outflow tract of the left ventricle, with a disk placed in the middle to represent the valve plane. In order to make the segmentation fully automatic, we employ the Kalman filter state estimation in two phases. In the first phase, the surface is positioned according to a priori knowledge on the specific imaging sector used in the acquisition. The Kalman filter estimation is then performed

using a stiff model that allows for global translation, scaling and rotation, but no deformation, which captures the global location and motion of the valve. In the second phase, the Kalman filter is used to estimate only the local deformation of the cylindrical surface, applied on top of the motion tracking from the first phase. The geometry of the valve plane is then extracted from the resulting segmentation, and clinically relevant measurements are calculated.

The algorithm was evaluated by comparing measurements of the valve perimeter, area and diameters against manual measurements done by two independent clinical experts in 16 patients with varying degrees of aortic valve disease. The method achieved diameter agreements (mean±SD) of -0.3 ± 1.6 and -0.2 ± 2.3 mm with respect to the two manual observers, compared to an inter-observer agreement of -0.1 ± 2.1 mm, with a mean computation time of 10 s.

II Automated Segmentation of the Right Ventricle in 3D Echocardiography: A Kalman Filter State Estimation Approach

Jørn Bersvendsen, Fredrik Orderud, Richard J. Massey, Kristian Fosså, Olivier Gerard, Stig Urheim and Eigil Samset, *IEEE Transactions on Medical Imaging, 2016,* 35*:1.*

In this paper, assess the second study aim, and adapt the state estimation segmentation previously applied in paper I to the Right Ventricle (RV). Because of the Left Ventricle's (LV) central role in cardiac function and disease, it has, historically, received the majority of attention in the literature, with image processing methods for the RV infrequently reported. However, as the RV's role in cardiovascular disease is being more widely recognized, interest in RV function and imaging is growing.

Segmentation methods proposed for the LV, as well as the method used in I, are not immediately applicable to the RV, as the ventricles differ in certain aspects, making RV segmentation a challenging task. For instance, where the LV has a simple and symmetric shape, with a thick myocardium resulting in well-defined endocardial borders, the RV has a complex shape that bends around the LV, and a thin myocardium. Furthermore, the RV has more pronounced trabeculations than the LV, especially in the apical region, making the definition of the endocardial border a challenge. Finally, acquiring images of the complete RV with ultrasound is often not possible, as part of the sound wave is typically shadowed by the lungs or sternum.

To overcome the challenges specific to the right heart, we introduce a strong shape prior in the form of a statistical shape model. The RV shape variation is learned by analyzing manual segmentations in 280 Magnetic Resonance Imaging (MRI) frames from 14 patients with different heart diseases. By decomposing the space of all these shapes into a subset, using principle component analysis, we were able to account for 95 % of the shape variation using only 12 shape parameters. This statistical shape model was used in the Kalman filter framework to provide an automated segmentation method for the RV.

The method was evaluated by comparing clinical indices and surface distance metrics against manual measurements from both echocardiography and MRI in 17 clinical cases. A mean absolute distance between the proposed and manual segmentations of 3.6 ± 0.7 mm was achieved, as well as end-diastolic volume agreements of 7 ± 30 mL and -26 ± 24 mL compared to echocardiography and MRI respectively. The method achieved a mean computation time of 2 s per case.

III Automated Bi-Ventricular Segmentation in 3-Dimensional Echocardiography by Coupled Deformable Surfaces

Jørn Bersvendsen, Fredrik Orderud, Øyvind Lie, Richard J. Massey, Kristian Fosså, Raúl San José Estépar, Stig Urheim and Eigil Samset, *Submitted for peer review.*

With the method presented in paper II, together with previous applications [4], [46], the segmentation framework has been demonstrated to work on both ventricles independently. However, as the ventricles interact with each other to perform the pumping function, and share a wall, the septum, which is of high importance in assessing cardiac disease, there is a need to assess both ventricles simultaneously.

In this paper, we present a method for automated biventricular and epicardial segmentation, operating on the fusion of two separate 3D ultrasound images. The most important contribution of the paper is a novel surface representation that is able to represent the endo- and epicardial borders of both ventricles in a natural and anatomically correct way, while both maintaining the desired properties of the subdivision surfaces used in papers I and II, and enabling the introduction of mechanical properties of the myocardium within the segmentation framework.

Because the myocardial volume remains roughly constant throughout the cardiac cycle [17], [47], [48], a distinct thickening of the myocardium is visible as the ventricles contract. This information is introduced to the segmentation method by regularizing the myocardial volume in the Kalman filter motion model, which gives a natural and physiologically correct surface representation.

The method was validated against manual measurements and segmentations in 16 clinical cases, a subset of the data used in paper II. Mean absolute distances of 2.8 ± 0.4 mm, 3.1 ± 0.6 mm, and 3.1 ± 0.5 mm between the proposed and reference segmentations were observed for the LV endocardium, RV endocardium and LV epicardium respectively. The method was computationally efficient, with a computation time of 2.1 ± 0.4 s per case.

IV Robust Spatio-Temporal Registration of 4D Cardiac Ultrasound Sequences

Jørn Bersvendsen, Matthew Toews, Adriyana Danudibroto, William M. Wells III, Raúl San José Estépar, Stig Urheim and Eigil Samset, *Proc. SPIE 9790, Medical Imaging 2016: Ultrasonic Imaging and Tomography.*

The biventricular segmentation method presented in paper III operates on a fused image created by manual registration of two separate real-time 3D echocardiographic images. This manual fusion is necessary because it is very hard to capture both ventricles in the same ultrasound image while maintaining satisfactory temporal and spatial resolutions. However, manually fusing 3D images in space and time is time-consuming and subject to inter-observer variation, which limits the appeal of the segmentation method for clinical application.

Here, we assess this problem by presenting a fully automatic spatio-temporal registration method for real-time 3D cardiac ultrasound sequences. The method is based on the previous work of Toews *et al.* for extraction of distinct features from 3D images, and using these features for image alignment [49], [50]. In the case of the biventricular segmentation, the goal is to register two ultrasound sequences taken of the same patient during the same exam. One can therefore assume that the true alignment between the sequences is rigid and static during the cardiac cycle. This assumption leads to a novel feature-based alignment method, in which features extracted from all frames are compared to each other simultaneously with no a priori assumption on their temporal alignment. The result is a fully automatic, robust and accurate registration method.

The method was validated on the same dataset as in paper III, by manually annotating anatomical landmarks and valve events. After registration, the mean distances between manually identified landmarks in the two images were 4.3 ± 1.2 mm compared to a ground truth error of 2.8 ± 0.6 mm with manual registration. For the temporal alignment, the absolute errors in valvular event times were 14.4 ± 11.6 ms for Aortic Valve (AV) opening, 18.6 ± 16.0 ms for AV closing, and 34.6 ± 26.4 ms for mitral valve opening, compared to a mean inter-frame time of 29 ms.

Chapter 4

Discussion

4.1 Contributions

4.1.1 Aortic root segmentation

In this thesis, four main contributions have been made. Firstly, a method for segmenting the Left Ventricular Outflow Tract (LVOT) and aortic root in 3D Transesophageal Echocardiographic (TEE) images has been developed, and its feasibility of fully automatically quantifying the aortic valve annulus size has been demonstrated (paper I). This is a key assessment to make prior to Transcatheter Aortic Valve Implantation (TAVI), a procedure which is gaining popularity worldwide as excellent improvements in the quality of life have been thoroughly demonstrated for a very high risk patient group [51], [52]. It is well known that regular 2D TEE fails to accurately describe the 3D structure of the Aortic Valve (AV), leading to an underestimation of the valve size [43]–[45], which has been shown to increase the incidence rate of post operational valve leakage [53]. 3D TEE is therefore better suited for this assessment. However, as performing manual measurements in these 3D images is time-consuming and subject to inter-observer variation [44], the presented automatic method has the potential to make a very valuable contribution to clinical practice. In fact, the method has already been commercialized and is now available in the 4D Auto AVQ tool on the newest release of GE Vingmed Ultrasound's E95 systems.

Though AV segmentation in 3D TEE images is not extensively studied, methods for this purpose have been presented previously. Ionasec *et al.* reported a method for automatic fitting of a comprehensive model of the coupled mitral and aortic valves, applied to both Computed Tomography (CT) and 3D TEE images [54]. The method is fully automatic and consists of three main steps, all solved with machine learning techniques. Firstly, the global location and rigid motion of the valve apparatus are estimated using a trained classifier and marginal space learning [55]. Secondly, the motion of key anatomical landmarks are estimated using a novel trajectory spectrum learning technique. Finally, a surface is fitted to the landmarks using a learning-based boundary detector together with Statistical Shape Model (SSM). A clinical validation of this method was performed by

Calleja *et al.* [56], which included some manual interaction and adjustment. The reported diameter agreements were comparable to the results of our proposed method.

Pouch *et al.* reported a method for segmentation of the aortic leaflets [57], using a deformable model in combination with multi-atlas label fusion. The specific surface representation, a continuous medial representation, was later extended to allow the inclusion of the aortic root [58]. Interestingly; this representation incorporates locally varying leaflet thickness. Although the authors do not discuss the motivation for this in particular, it may have potential clinical use as aortic sclerosis, i.e. local leaflet thickening with preserved function, is the first macroscopic change in the leaflets observable in patients with calcified aortic valve disease [59].

Finally, Queiros *et al.* recently reported a method for deformable model-based segmentation of the LVOT and aortic root [60]. The method extends the B-Spline Explicit Active Surface (BEAS) [24] framework for deformable model segmentation with statistical information on the longitudinal profile of the aortic structure. In the BEAS framework, the surface is given by an explicit function in cylindrical coordinates, where the radius is parameterized with B-spline. Based on manually annotated pints in the LVOT and ascending aorta, the statistical mean model is initialized in the image. The surface is then evolved by energy minimization, incorporating regularization based on the SSM.

Our proposed method is based on the state-estimation framework described in section 2.2, where a deformable smooth surface is fitted to the image sequence. Similar to the methods presented by Ionasec *et al.* [54] and Queiros *et al.* [60], we employ a two-step approach. The global position, size and motion of the model are estimated first, before refining the segmentation by locally deforming the surface.

All of the three discussed related methods [54], [57], [60] include some information from manually annotated images in some form, either in learned classifiers, multi-atlas label fusion or statistical shape models. In contrast, our method does not include such prior information. While this eliminates the need for large databases of ground-truth segmentations, it also means that segmentation can not be expected to achieve the same level of accuracy in some cases, particularly in the presence of acoustic shadowing due to calcifications on the valve. In paper II we show how statistical shape information can be introduced to the segmentation framework, which would likely increase robustness in these cases.

Although we focused on the aortic valve annulus, other measurements are also of interest for assessing the AV morphology for TAVI. Some measurements are directly available from the proposed method, such as diameters at LVOT, sinus of Valsalva and sinotubular junction. However, because we do not model the leaflets, we can not assess the aortic valve at the same level of detail as some proposed methods [54], [57], [58].

In clinical practice, the annulus diameter is typically measured in a single systolic frame [42]. In our proposed method however, we perform a dynamic assessment of the aortic root. Because we combine information from different frames, this helps increase the robustness of the segmentation, and prevent over-fitting of noisy determination of image edges. Furthermore, dynamic assessment of the aortic root is of some clinical relevance in the context of TAVI. For instance, Masri *et al.* found aortic annulus deformation during the cardiac cycle to be a predictor for post-procedural aortic regurgitation [61],

which is associated with worse outcome and increased mortality [62].

4.1.2 Segmentation of the right ventricle

The major part of the research in this thesis has focused on the Right Ventricle (RV), with two methods developed for automated RV segmentation (papers II and III). Historically, the importance of the RV has been underestimated [5], [6], with the Left Ventricle (LV) receiving most of the attention in both the clinical and technical literatures. However, as the RV's role in cardiovascular diseases is being more widely recognized, interest in RV function and imaging is growing. For instance, RV function has been shown to be a major determinant of clinical outcome [5], and accurate assessment of the RV is especially important in patients with pulmonary hypertension [63], [64] and congenital heart disease [65]. Furthermore, RV ejection fraction represents a strong and independent indicator of mortality in left heart failure patients [6], [66].

Because of its complex shape, imaging the RV with regular 2D ultrasound is very challenging [9], and 3D echocardiography is considered theoretically ideal for quantifying the RV volumes and ejection fraction [67]. As described in section 2.1.3, the two ventricles are different in shape and appearance; the RV has a more complex and asymmetrical shape, large inter-patient variation, thin walls with pronounced trabeculations, and a challenging acquisition. These factors make RV segmentation a difficult task, and methods developed for the LV are not necessarily applicable to the RV. In particular, acquisitions of the RV often suffer from acoustic shadowing of the RV outflow tract and free wall [68].

Compared to the LV, the field of RV segmentation is largely unexplored, for echocardiography in particular [22], [69] but also for other imaging modalities [70]. For segmentation of the RV in 3D Transthoracic Echocardiography (TTE), Angelini *et al.* have presented a level-set framework for chamber segmentation, applied to both the LV and the RV [22]. In this level-set method, the ventricle surfaces are represented implicitly as the zero-intersection of a higher order function, which is fitted to individual image frames by energy minimization. Recently, Stebbing *et al.* have described a segmentation method using an explicit Loop subdivision surface model of the RV and solving the fitting problem with energy minimization [69]. This method also includes prior shape information in order to cope with missing boundaries. Contrary to our proposed method, however, where prior shape statistics are incorporated in the shape representation, Stebbing *et al.* [69] instead perform joint segmentation of multiple image sequences while at the same time optimizing the underlying statistical model. The image sequences for joint segmentation can either be of multiple patients, or multiple views of the same patient. This removes the need for manually annotated training data, which indeed is challenging to generate in itself, precisely because of missing boundaries. However, it also means that there is a lack of desired expert knowledge input to the method, and it requires simultaneous segmentation in multiple images, which is computationally expensive and undesired in clinical applications.

The validation presented in paper II was performed on patients with aortic insufficiency. This is not a patient population where the RV is of particular interest, and it would have been preferable to perform the analysis on patients with diseases that have impact

on RV shape and motion, such as pulmonary hypertension. Unfortunately, this was not possible with the retrospective data set of 3D TTE images of the RV that were available to us.

4.1.3 Biventricular segmentation

One of the two RV methods presented in this thesis (paper III) is a biventricular segmentation method, which uses a geometric model consisting of three coupled surfaces; LV endocardium, RV endocardium and LV/RV epicardium. This is an extension of a previous approach by Orderud *et al.* for joint LV endocard and epicard segmentation, where two separate deformable surfaces share a global rigid transform and has a fixed spatial relationship with each other [46]. In the presented extension, the control mesh is shared between the endocardial and epicardial surfaces, and their relationship is expressed with myocardial volume states. This allows us to incorporate the incompressibility of the myocardium [17], [48] into the segmentation framework, which has been shown to be an effective regularization for segmentation in 3D echocardiography [47] and MRI [71].

This biventricular model allows one to study the interaction between the ventricles. Because, the coupled surface formulation can be used with any number of surfaces, the method also makes a good candidate for a four-chamber segmentation method. In addition to supporting the endocardial segmentation, identifying both endo- and epicardial borders allows one to measure the myocardial thickness and volume, and from there estimate the myocardial mass. Assessment of LV mass is done routinely, and LV mass is an important risk factor for, and predictor of, cardiovascular events [72]. Although LV mass is often measured by 2D echo in current clinical practice, 3D echo is, theoretically, better suited, as it is the only echocardiographic method that measures the myocardial volume directly [72].

4.1.4 Spatiotemporal registration

A robust method for fully automatic spatio-temporal registration between two ultrasound sectors has been presented (paper IV). Although the main motivation is the fusion of apical LV and RV images to solve a limitation in the biventricular segmentation method, the method is a valuable contribution to the general problem of extended field of view.

The method is an extension of the work by Ni *et al.* who used 3D SIFT features to create a panorama image from several 3D ultrasound images of the liver by rigid registration [73], and Perperidis *et al.* [74] and Zhang *et al.* [75] who used Normalized Cross Correlation (NCC) over time for temporal alignment of Magnetic Resonance Imaging (MRI) sequences and between MRI and ultrasound respectively. The method is able to perform the spatial registration with no assumption on the relationship between the recordings, neither in time nor space. Although a manual registration was used for the evaluation of the presented biventricular segmentation, this method could have been used instead, which would greatly reduce the required user input, though it is not clear to what degree an increased error in registration would affect the segmentation.

4.1.5 Clinical applicability and theoretical contributions

As this has been a joint academic and industrial endeavor, research in this thesis has been focused more on obtaining clinically applicable solutions than on making theoretical contributions. As such, existing methodologies have been adapted and applied to different problems, in particular the Kalman filter segmentation framework [2]–[4].

This framework operates by fitting smooth surfaces to the endocardial border. The use of such smooth surfaces introduces robustness to the algorithm, and prevents overfitting of noisy determination of the endocardial boundary. Robustness is a key aspect of the method when considering clinical applicability. In reality, however, the endocardium is not smooth. It is trabeculated, and contains structures, such as the papillary muscles and the moderator band of the right ventricle. Although the presented methods could incorporate these structures and irregularities to some extent by increasing the resolution of the surface representation, ultimately, these methods may not be well suited for this level of detail. However, for global and segmental quantification of shape and function in clinical practice, one must make a trade-off between accuracy and robustness. Furthermore, current 3D echocardiography often fails to visualize some of these irregularities in the first place.

Another key motivator for the method selection in this thesis is the low computational complexity. Echocardiography is routine and very much hands-on, and a fast quantification is vital for clinical adoption.

4.2 Evaluation of the Kalman filter state estimation approach

All of the three segmentation methods presented in this thesis use the same underlying Kalman Filter (KF) state estimation approach. This general-purpose framework was originally developed by Blake *et al.* [76]–[78], applied to 2D echocardiographic sequences by Jacob *et al.* [79], [80], and extended to 3D echo by Orderud *et al.* [2]–[4].

Since its introduction by R. E. Kalman in 1960 [33], the KF has found numerous applications in technology, including vehicle guidance and navigation, signal processing, and robotic motion control. However, it should be noted that the KF assumes certain aspect of the process to be estimated that are typically not held in practical applications [81]. Firstly, the process is assumed to satisfy the Markov property, meaning that the future state is assumed to be given exclusively by the current state. Secondly, the process is assumed to be linear, or locally linear in the case of the Extended KF (EKF). Finally, the process is assumed to be subject to additive Gaussian noise.

In the case of cardiac segmentation, the Markov process is not an accurate description, especially since the cardiac motion is cyclical. The deformable model is typically also non-linear, for instance when a global rotation is used, for which a linearized model is a fair approximation for only small rotations. Furthermore, in the formulation of Orderud *et al.* [3], [4] used in this thesis, the measurement noise for each of the edge detec-

tors are assumed to be independent of each other, which is used to make the segmentation computationally efficient with a large number of edge detections. This assumption clearly does not hold, as neighboring edge detections are correlated with each other, and all edge detectors are influenced by the global image quality.

However, the use of the KF segmentation approach can be justified by the following considerations. Firstly, the method has been previously demonstrated to give accurate segmentations of 3D echocardiographic images. It is also a very elegant solution, allowing for an intuitive integration of prior shape information, motion model, regularization and measurements. Furthermore, it is easily adapted to a wide range of shape parameterizations, such as spline surfaces and statistical shapes, and a wide range of data measurements, such as edge detections, speckle tracking, tissue Doppler, and manual landmark locations. Finally, it is very computationally efficient, with a tracking time on the order of a few milliseconds per frame.

4.3 Differences in methodologies for right ventricle segmentation

Two methods have been presented for cardiac chamber segmentation in this thesis, both based on the Kalman filter state estimation approach; the first (paper II) using a Statistical Shape Model (SSM) of the RV alone, and the second (paper III) using coupled surfaces representing the RV, LV, and epicardium, with a myocardial volume conservation constraint. Although the scopes of the two presented methods differ significantly, from the RV endocardium alone to a joint biventricular and epicardium segmentation, it is still natural to compare the two approaches for the purpose of RV segmentation.

4.3.1 Considerations of statistical shape models

The use of Statistical Shape Models (SSM) in medical image analysis has shown great promise across modalities, including echocardiography, MRI and CT, and across target anatomy, including bone, brain, abdominal and cardiac structures [19]. The SSM approach to segmentation has some key advantages. Firstly, it behaves as a very effective prior, limiting the deformation and search spaces to statistically plausible shapes. This means that the segmentation method can give a design guarantee never to produce an unrealistic result, even in the presence of heavy image noise and artifacts. Using a SSM prior also introduces robustness against missing image information, such as acoustic shadowing of the anterolateral RV free wall, by assuming in these regions a statistically plausible shape, deduced from all available shape information.

However, introducing a SSM has certain consequences that must be considered. Firstly, the quality of any statistical model is limited by the quality and quantity of the data from which it was deduced, which is true for the SSM as well. In order to create a SSM, one needs a training set of manual segmentations. If the training set is not extensive enough, or does not cover the true range of shapes in the target population, the SSM

will typically be too restrictive, and fail to capture the true shape variation observed in clinical practice. This can lead to wrong segmentations even in images where the endocardial borders are well visualized.

Secondly the SSM differs from conventional deformable models in that its parameterization is *global* as opposed to *regional*. With deformable models, the deformation of one part of the model is typically mostly given by the image information in that region. Although this approach may produce globally implausible shapes, from a user perspective it is intuitive and natural. With the global parameterization of SSMs, however, the shape is influenced by all image information at the same time, and changing any parameter has a global effect. Although the approach is mathematically sound and can guarantee a globally plausible shape, the user is no longer able to reason locally about the segmentation.

4.3.2 Considerations of the biventricular segmentation

The method presented for biventricular segmentation differs from the RV segmentation in that it does not use a SSM, and hence does not require an extensive training set of manual segmentations. Instead, the method relies on added coupled surfaces of the LV endocardium and Epicardium (EPI), in addition to myocardial volume regularization. Furthermore, a "personalization" step is added, where the gross shape of the RV, including the width/height ratio and orientation of the LV outflow tract, is set up corresponding to manual user input prior to segmentation.

Although the method does not use a SSM, some, though not all, of the benefits of the SSM are captured to some extent with the additional surfaces, regularization and personalization. The LV and EPI surfaces will assist the RV segmentation in two important ways; through the shared global transform, including global translation, scale and rotation, and through the coupling of the RV with the LV and EPI surfaces through the shared deformation and volume states. However, one can not expect the biventricular segmentation method to perform as well as the RV SSM approach in the presence of significant missing edges.

It should be noted that the two ventricle segmentation approaches are not mutually exclusive. For instance, one could use the same SSM approach as done in the RV paper to derive a statistical deformation space for the mid-wall biventricular control mesh, which could be used alongside the myocardial volume regularization.

4.3.3 Considerations from a clinical perspective

The two methods differ in the amount of user interaction that is required to run the segmentation. The RV method requires the identification of three landmarks in both end diastole and end systole; RV apex, tricuspid valve center and pulmonary valve center. The biventricular method, on the other hand, requires manual identification of seven landmarks in end diastole only; LV apex, mitral, aortic and tricuspid valve centers, anterior and posterior RV-LV junctions, and a point on the lateral RV free wall.

While the alignment for the biventricular case is more involved and time consuming, it intentionally does not include manual identification of the pulmonary valve, which is

required in the RV method. The pulmonary valve is difficult to image from an apical position, and is often partially shadowed by the sternum or lungs [68], making it hard and cumbersome to identify in the ultrasound image. Instead, the position of the pulmonary valve is essentially deduced from the locations of the tricuspid and aortic valves, as well as the RV-LV junctions, which are typically much easier to identify in the image.

Chapter 5

Conclusions

In this thesis, four main bodies of work have been presented, concentrated on the three aims of study laid out in section 1.2.

Firstly, a fully automatic segmentation method of the left ventricular outflow tract and aortic root has been developed, designed to measure the aortic annulus diameter prior to aortic valve repair, such as Transcatheter Aortic Valve Implantation (TAVI) and Surgical Aortic Valve Replacement (SAVR). The method was validated and performed indistinguishable from manual measurements done by experienced cardiologists. This method solves a specific clinical need, and has been made commercially available on the newest GE Vingmed Ultrasound scanners.

Secondly, the existing state estimation segmentation framework of Orderud *et al.*, previously applied to the left ventricle, has been extended to the right ventricle. Segmentation of the right ventricle is a challenging task, and few methods tackling this problem have previously been presented in the literature. This work demonstrates the combination of a statistical shape model, learned from a database of manual segmentations, with the information fusion of the Kalman filter approach, resulting in an accurate and computationally efficient method.

Thirdly, two methods related to the biventricular segmentation problem have been presented. The biventricular segmentation method uses a novel surface representation to represent he endo- and epicardial borders of both ventricles in a natural and anatomically correct way. This parametric surface allows the incorporation of mechanical properties of the myocardium, i.e. the myocardial volume conservation, while maintaining the desired properties of the subdivision surfaces used in previous works, such as inherent regularization and low dimensionality.

Because it is unrealistic to capture both ventricles in the same ultrasound sector, a method has been developed for spatio-temporal registration of two 3D ultrasound sectors. The method is fully automatic, and does not have any a priori assumption on the alignment of the recordings. Furthermore, the method demonstrates that it is possible to perform a robust feature-based spatial alignment with no prior information on the temporal alignment.

References

[1] M. Nichols, N. Townsend, P. Scarborough, and M. Rayner, "Cardiovascular disease in europe 2014: Epidemiological update," *European Heart Journal*, vol. 35, pp. 2950–2959, 42 2014.

[2] F. Orderud, J. Hansgård, and S. I. Rabben, "Real-time tracking of the left ventricle in 3d echocardiography using a state estimation approach," in *Medical Image Computing and Computer-Assisted Intervention - MICCAI 2007*, ser. Lecture Notes in Computer Science, vol. 4791, Springer Berlin Heidelberg, 2007, pp. 858–865.

[3] F. Orderud, "A framework for real-time left ventricular tracking in 3d+t echocardiography, using nonlinear deformable contours and kalman filter based tracking," in *Computers in Cardiology, 2006*, IEEE, 2006, pp. 125–128.

[4] F. Orderud and S. I. Rabben, "Real-time 3d segmentation of the left ventricle using deformable subdivision surfaces," in *Computer Vision and Pattern Recognition, 2008. IEEE Conference on*, Norwegian Univ. of Sci. & Technol., Trondheim, IEEE, Jun. 2008.

[5] G. B. Bleeker, P Steendijk, E. R. Holman, C.-M. Yu, O. A. Breithardt, T. A. M. Kaandorp, M. J. Schalij, E. E. van der Wall, P Nihoyannopoulos, and J. J. Bax, "Assessing right ventricular function: the role of echocardiography and complementary technologies.," *Heart*, vol. 92, pp. i19–i26, Suppl 1 2006.

[6] F. Haddad, R. Doyle, D. J. Murphy, and S. A. Hunt, "Right ventricular function in cardiovascular disease, part ii: Pathophysiology, clinical importance, and management of right ventricular failure," *Circulation*, vol. 117, pp. 1717–1731, 13 2008.

[7] J. Hansegård, S. Urheim, K. Lunde, S. Malm, and S. Rabben, "Semi-automated quantification of left ventricular volumes and ejection fraction by real-time three-dimensional echocardiography," *Cardiovascular Ultrasound*, vol. 7, p. 18, 1 2009.

[8] J. G. Betts *et al.*, *Anatomy & Physiology*. OpenStax College, 2013.

[9] R. M. Lang, M. Bierig, R. B. Devereux, F. A. Flachskampf, E. Foster, P. A. Pellikka, M. H. Picard, M. J. Roman, J. Seward, J. Shanewise, S. Solomon, K. T. Spencer, M. St. John Sutton, and W. Stewart, "Recommendations for chamber quantification," *European Heart Journal - Cardiovascular Imaging*, vol. 7, pp. 79–108, 2 2006.

[10] F. Sheehan and A. Redington, "The right ventricle: Anatomy, physiology and clinical imaging," *Heart*, vol. 94, pp. 1510–1515, 11 2008.

[11] R. H. Anderson and A. E. Becker, *Slide Atlas of Cardiac Anatomy 3: The Ventricles I: Introduction - The Morphologically Right Ventricle*. Gower Medical Publishing inc., 1980.

[12] R. J. Damiano, P. Lafollette, J. L. Cox, J. E. Lowe, and W. P. Santamore, "Significant left ventricular contribution to right ventricular systolic function," *American Journal of Physiology*, vol. 261, H1514–H1524, 5, 2 1991.

[13] N. F. Voelkel, R. A. Quaife, L. A. Leinwand, R. J. Barst, M. D. McGoon, D. R. Meldrum, J. Dupuis, C. S. Long, L. J. Rubin, F. W. Smart, Y. J. Suzuki, M. Gladwin, E. M. Denholm, and D. B. Gail, "Right ventricular function and failure: Report of a national heart, lung, and blood institute working group on cellular and molecular mechanisms of right heart failure," *Circulation*, vol. 114, pp. 1883–1891, 17 2006.

[14] J. A. Noble and D. Boukerroui, "Ultrasound image segmentation: A survey," *IEEE Transactions on Medical Imaging*, vol. 25, pp. 987–1010, 8 2006.

[15] A. Hu, B. Grossberg, and C. Mageras, "Survey of recent volumetric medical image segmentation techniques," in *Biomedical Engineering*, InTech, 2009.

[16] S. Mazaheri, P. Binti Sulaiman, R. Wirza, F. Khalid, S. Kadiman, M. Dimon, and R. Tayebi, "Echocardiography image segmentation: A survey," in *Advanced Computer Science Applications and Technologies (ACSAT), 2013 International Conference on*, 2013, pp. 327–332.

[17] V. Tavakoli and A. A. Amini, "A survey of shaped-based registration and segmentation techniques for cardiac images," *Computer Vision and Image Understanding*, vol. 117, pp. 966 –989, 9 2013.

[18] J. Montagnat, H. Delingette, and N. Ayache, "A review of deformable surfaces: Topology, geometry and deformation," *Image and Vision Computing*, vol. 19, pp. 1023 –1040, 14 2001.

[19] T. Heimann and H.-P. Meinzer, "Statistical shape models for 3d medical image segmentation: a review," *Medical Image Analysis*, vol. 13, pp. 543–63, 4 Aug. 2009.

[20] S. Osher and J. A. Sethian, "Fronts propagating with curvature-dependent speed: Algorithms based on hamilton-jacobi formulations," *Journal of Computational Physics*, vol. 79, pp. 12–49, 1 Nov. 1988.

[21] D. Cremers, M. Rousson, and R. Deriche, "A review of statistical approaches to level set segmentation: Integrating color, texture, motion and shape," *International Journal of Computer Vision*, vol. 72, pp. 195–215, 2 2007.

[22] E. D. Angelini, S. Homma, G. Pearson, J. W. Holmes, and A. F. Laine, "Segmentation of real-time three-dimensional ultrasound for quantification of ventricular function: a clinical study on right and left ventricles," *Ultrasound in Medicine & Biology*, vol. 31, pp. 1143–58, 9 Sep. 2005.

[23] F. Galluzzo, D. Barbosa, H. Houle, N. Speciale, D. Friboulet, J. D'hooge, and O. Bernard, "A gpu level-set segmentation framework for 3d echocardiography," in *Ultrasonics Symposium (IUS), 2012 IEEE International*, 2012, pp. 2639–2642.

[24] D. Barbosa, T. Dietenbeck, J. Schaerer, J. D'hooge, D. Friboulet, and O. Bernard, "B-spline explicit active surfaces: An efficient framework for real-time 3-d region-based segmentation," *IEEE Transactions on Image Processing*, vol. 21, pp. 241–251, 1 2012.

[25] O. Gerard, A. Billon, J.-M. Rouet, M. Jacob, M. Fradkin, and C. Allouche, "Efficient model-based quantification of left ventricular function in 3-d echocardiography," *IEEE Transactions on Medical Imaging*, vol. 21, pp. 1059–1068, 9 2002.

[26] J. Montagnat and H. Delingette, "4d deformable models with temporal constraints: Application to 4d cardiac image segmentation," *Medical Image Analysis*, vol. 9, pp. 87 –100, 1 2005.

[27] J. Hansegård, F. Orderud, and S. I. Rabben, "Real-time active shape models for segmentation of 3d cardiac ultrasound," in *Computer Analysis of Images and Patterns*, ser. Lecture Notes in Computer Science, vol. 4673, Springer Berlin Heidelberg, 2007, pp. 157–164.

[28] D. Doo, "A subdivision algorithm for smoothing down irregularly shaped polyhedrons," in *Proceedings on Interactive Techniques in Computer Aided Design*, (Bologna, Italy), IEEE, 1978, pp. 157 –195.

[29] E. Catmull and J. Clark, "Recursively generated b-spline surfaces on arbitrary topological meshes," *Computer-Aided Design*, vol. 10, pp. 350 –355, 6 1978.

[30] J. Stam, "Exact evaluation of catmull-clark subdivision surfaces at arbitrary parameter values," in *Proceedings of the 25th Annual Conference on Computer Graphics and Interactive Techniques*, ser. SIGGRAPH '98, New York, NY, USA: ACM, 1998, pp. 395–404.

[31] C. Loop, "Smooth subdivision surfaces based on triangles," Master's thesis, The University of Utah, Aug. 1987.

[32] J. Stam, "Evaluation of loop subdivision surfaces," 1998.

[33] R. E. Kalman, "A new approach to linear filtering and prediction problems," *Journal of Basic Engineering*, vol. 82, pp. 35–45, 1960.

[34] S. J. Julier and J. K. Uhlmann, "A new extension of the kalman filter to nonlinear systems," in *Proc. of AeroSense: The 11th Int. Symp. on Aerospace/Defense Sensing, Simulations and Controls*, vol. 3, 1997, pp. 182–193.

[35] F. Orderud, "Real-time segmentation of 3d echocardiograms using a state estimation approach with deformable models," PhD thesis, Norwegian University of Science and Technology, 2009.

[36] R. G. Brown and P. Y. C. Hwang, *Introduction to Random Signals and Applied Kalman Filtering*, 3rd ed. Prentice Hall, 1996.

[37] D. Fraser and J. Potter, "The optimum linear smoother as a combination of two optimum linear filters," *IEEE Transactions on Automatic Control*, vol. 14, pp. 387–390, 4 1969.

[38] F. Orderud, G. Kiss, S. Langel, E. W. Remme, H. Torp, and S. I. Rabben, "Real-time left ventricular speckletracking in 3d echocardiography with deformable subdivision surfaces," in *MICCAI Workshop on Analysis of Functional Medical Images*, 2008, pp. 41–48.

[39] J. Hansegård, "Automated volume measurements in echocardiography by utilizing expert knowledge," PhD thesis, University of Oslo, 2008.

[40] S. R. Snare, "Quantitative cardiac analysis algorithms for pocket-sized ultrasound devices," PhD thesis, Norwegian University of Science and Technology, 2011.

[41] E. Dikici, "Ultrasound cardiac modeling, segmentation and tracking," PhD thesis, Norwegian University of Science and Technology, 2013.

[42] J. L. Zamorano, L. P. Badano, C. Bruce, K.-L. Chan, A. Gonçalves, R. T. Hahn, M. G. Keane, G. La Canna, M. J. Monaghan, P. Nihoyannopoulos, F. E. Silvestry, J.-L. Vanoverschelde, L. D. Gillam, A. Vahanian, V. Di Bello, and T. Buck, "Eae/ase recommendations for the use of echocardiography in new transcatheter interventions for valvular heart disease.," *European Heart Journal*, vol. 12, pp. 557–84, 8 Aug. 2011.

[43] A. C. T. Ng, V. Delgado, F. van der Kley, M. Shanks, N. R. L. van de Veire, M. Bertini, G. Nucifora, R. J. van Bommel, L. F. Tops, A. de Weger, G. Tavilla, A. de Roos, L. J. Kroft, D. Y. Leung, J. Schuijf, M. J. Schalij, and J. J. Bax, "Comparison of aortic root dimensions and geometries before and after transcatheter aortic valve implantation by 2- and 3-dimensional transesophageal echocardiography and multislice computed tomography.," *Circulation: Cardiovascular imaging*, vol. 3, pp. 94–102, 1 Jan. 2010.

[44] E. Altiok, R. Koos, J. Schröder, K. Brehmer, S. Hamada, M. Becker, A. H. Mahnken, M. Almalla, G. Dohmen, R. Autschbach, N. Marx, and R. Hoffmann, "Comparison of two-dimensional and three-dimensional imaging techniques for measurement of aortic annulus diameters before transcatheter aortic valve implantation.," *Heart*, vol. 97, pp. 1578–84, 19 Oct. 2011.

[45] D. Muraru, L. P. Badano, M. Vannan, and S. Iliceto, "Assessment of aortic valve complex by three-dimensional echocardiography: a framework for its effective application in clinical practice.," *European Heart Journal - Cardiovascular Imaging*, vol. 13, pp. 541–55, 7 Jul. 2012.

[46] F. Orderud, G. Kiss, and H. G. Torp, "Automatic coupled segmentation of endo- and epicardial borders in 3d echocardiography," in *Ultrasonics Symposium, 2008. IUS 2008. IEEE*, 2008, pp. 1749–1752.

[47] Y. Zhu, X. Papademetris, A. J. Sinusas, and J. S. Duncan, "A coupled deformable model for tracking myocardial borders from real-time echocardiography using an incompressibility constraint," *Medical Image Analysis*, vol. 14, pp. 429 –448, 3 2010.

[48] L. Glass, P. Hunter, and A. McCulloch, Eds., *Theory of Heart: Biomechanics, Biophysics, and Nonlinear Dynamics of Cardiac Function*, ser. Institute for Nonlinear Science. Springer-Verlag, 1991.

[49] M. Toews, W. M. Wells III, and L. Zöllei, "A feature-based developmental model of the infant brain in structural mri," in *Medical Image Computing and Computer-Assisted Intervention - MICCAI 2012*, ser. Lecture Notes in Computer Science, vol. 7511, Springer Berlin Heidelberg, 2012, pp. 204–211.

[50] M. Toews and W. M. Wells III, "Efficient and robust model-to-image alignment using 3d scale-invariant features," *Medical Image Analysis*, vol. 17, pp. 271–282, 3 2013.

[51] M. R. Reynolds, E. A. Magnuson, K. Wang, V. H. Thourani, M. Williams, A. Zajarias, C. S. Rihal, D. L. Brown, C. R. Smith, M. B. Leon, and D. J. Cohen, "Health-related quality of life after transcatheter or surgical aortic valve replacement in high-risk patients with severe aortic stenosis: Results from the partner (placement of aortic transcatheter valve) trial (cohort a)," *Journal of the American College of Cardiology*, vol. 60, pp. 548 –558, 6 2012.

[52] L. J. Boothroyd, M. Spaziano, J. R. Guertin, L. J. Lambert, J. Rodés-Cabau, N. Noiseux, M. Nguyen, E. Dumont, M. Carrier, B. de Varennes, R. Ibrahim, G. Martucci, Y. Xiao, J. E. Morin, and P. Bogaty, "Transcatheter aortic valve implantation: Recommendations for practice based on a multidisciplinary review including cost-effectiveness and ethical and organizational issues," *Canadian Journal of Cardiology*, pp. 718–726, 6 2013.

[53] H. Jilaihawi, M. Kashif, G. Fontana, A. Furugen, T. Shiota, G. Friede, R. Makhija, N. Doctor, M. B. Leon, and R. R. Makkar, "Cross-sectional computed tomographic assessment improves accuracy of aortic annular sizing for transcatheter aortic valve replacement and reduces the incidence of paravalvular aortic regurgitation," *Journal of the American College of Cardiology*, vol. 59, pp. 1275–1286, 14 Apr. 2012.

[54] R. Ionasec, I. Voigt, B. Georgescu, Y. Wang, H. Houle, F. Vega-Higuera, N. Navab, and D. Comaniciu, "Patient-specific modeling and quantification of the aortic and mitral valves from 4-d cardiac ct and tee," *IEEE Transactions on Medical Imaging*, vol. 29, pp. 1636–1651, 9 2010.

[55] Y. Zheng, A. Barbu, B. Georgescu, M. Scheuering, and D. Comaniciu, "Four-chamber heart modeling and automatic segmentation for 3-d cardiac ct volumes using marginal space learning and steerable features," *IEEE Transactions on Medical Imaging*, vol. 27, pp. 1668–1681, 11 2008.

[56] A. Calleja, P. Thavendiranathan, R. I. Ionasec, H. Houle, S. Liu, I. Voigt, C. Sai Sudhakar, J. Crestanello, T. Ryan, and M. A. Vannan, "Automated quantitative 3-d modeling of the aortic valve and root by 3-d transesophageal echocardiography in normals, aortic regurgitation and, aortic stenosis: Comparison to computed tomography in normals and clinical implications," *Circulation: Cardiovascular Imaging*, 2012.

[57] A. M. Pouch, H. Wang, M. Takabe, B. M. Jackson, C. M. Sehgal, J. H. Gorman, R. C. Gorman, and P. A. Yushkevich, "Automated segmentation and geometrical modeling of the tricuspid aortic valve in 3d echocardiographic images," in *Medical Image Computing and Computer-Assisted Intervention - MICCAI 2013*, Springer Berlin Heidelberg, 2013, pp. 485–492.

[58] A. M. Pouch, S. Tian, M. Takabe, H. Wang, J. Yuan, A. T. Cheung, B. M. Jackson, J. H. Gorman, R. C. Gorman, and P. A. Yushkevich, "Segmentation of the aortic valve apparatus in 3d echocardiographic images: Deformable modeling of a branching medial structure," in *Statistical Atlases and Computational Models of the Heart STACOM (Workshop)*, Springer International Publishing, 2015, pp. 196–203.

[59] N. M. Rajamannan, F. J. Evans, E. Aikawa, K. J. Grande-Allen, L. L. Demer, D. D. Heistad, C. A. Simmons, K. S. Masters, P. Mathieu, K. D. O'Brien, F. J. Schoen, D. A. Towler, A. P. Yoganathan, and C. M. Otto, "Calcific aortic valve disease: Not simply a degenerative process," *Circulation*, vol. 124, no. 16, pp. 1783–1791, 2011.

[60] S. Queiros, A. Papachristidis, D. Barbosa, K. C. Theodoropoulos, J. C. Fonseca, M. J. Monaghan, J. L. Vilaca, and J. D'hooge, "Aortic valve tract segmentation from 3d-tee using shape-based b-spline explicit active surfaces," *IEEE Transactions on Medical Imaging*, 2016 (In Press).

[61] A. Masri, P. Schoenhagen, L. Svensson, S. R. Kapadia, B. P. Griffin, E. M. Tuzcu, and M. Y. Desai, "Dynamic characterization of aortic annulus geometry and morphology with multimodality imaging: Predictive value for aortic regurgitation after transcatheter aortic valve replacement," *Journal of Thoracic and Cardiovascular Surgery*, vol. 147, pp. 1847–1854, 6.

[62] K. Hayashida, T. Lefèvre, B. Chevalier, T. Hovasse, M. Romano, P. Garot, E. Bouvier, A. Farge, P. Donzeau-Gouge, B. Cormier, and M.-C. Morice, "Impact of post-procedural aortic regurgitation on mortality after transcatheter aortic valve implantation," *JACC: Cardiovascular Interventions*, vol. 5, pp. 1247–1256, 12 2012.

[63] L. L. Mertens and M. K. Friedberg, "Imaging the right ventricle - current state of the art," *Nature Reviews Cardiology*, vol. 7, pp. 551–563, 10 Oct. 2010.

[64] E. R. Valsangiacomo Buechel and L. L. Mertens, "Imaging the right heart: The use of integrated multimodality imaging," *European Heart Journal*, vol. 33, pp. 949–960, 8 2012.

[65] H. B. van der Zwaan, W. a. Helbing, J. S. McGhie, M. L. Geleijnse, S. E. Luijnenburg, J. W. Roos-Hesselink, and F. J. Meijboom, "Clinical value of real-time three-dimensional echocardiography for right ventricular quantification in congenital heart disease: validation with cardiac magnetic resonance imaging," *Journal of the American Society of Echocardiography*, vol. 23, pp. 134–40, 2 Feb. 2010.

[66] J. Meluzin, L. Spinarová, P. Hude, J. Krejcí, V. Kincl, R. Panovský, and L. Dusek, "Prognostic importance of various echocardiographic right ventricular functional parameters in patients with symptomatic heart failure," *Journal of the American Society of Echocardiography*, vol. 18, pp. 435–444, 5 Sep. 2015.

[67] Y. J. Shimada, M. Shiota, R. J. Siegel, and T. Shiota, "Accuracy of right ventricular volumes and function determined by three-dimensional echocardiography in comparison with magnetic resonance imaging: a meta-analysis study," *Journal of the American Society of Echocardiography*, vol. 23, pp. 943–53, 9 Sep. 2010.

[68] E. Ostenfeld, M. Carlsson, K. Shahgaldi, A. Roijer, and J. Holm, "Manual correction of semi-automatic three-dimensional echocardiography is needed for right ventricular assessment in adults; validation with cardiac magnetic resonance," *Cardiovascular Ultrasound*, vol. 10, 1 Jan. 2012.

[69] R. V. Stebbing, A. I. Namburete, R. Upton, P. Leeson, and J. A. Noble, "Data-driven shape parameterization for segmentation of the right ventricle from 3D+t echocardiography," *Medical Image Analysis*, vol. 21, pp. 29–39, 1 2015.

[70] C. Petitjean, M. A. Zuluaga, W. Bai, J.-N. Dacher, D. Grosgeorge, J. Caudron, S. Ruan, I. B. Ayed, M. J. Cardoso, H.-C. Chen, D. Jimenez-Carretero, M. J. Ledesma-Carbayo, C. Davatzikos, J. Doshi, G. Erus, O. M. O. Maier, C. M. S. Nambakhsh, Y. Ou, S. Ourselin, C.-W. Peng, N. S. Peters, T. M. Peters, M. Rajchl, D. Rueckert, A. Santos, W. Shi, C.-W. Wang, H. Wang, and J. Yuan, "Right ventricle segmentation from cardiac mri: a collation study," *Medical Image Analysis*, vol. 19, pp. 187–202, 1 Jan. 2015.

[71] A. Bistoquet, J. Oshinski, and O. Skrinjar, "Left ventricular deformation recovery from cine mri using an incompressible model," *IEEE Transactions on Medical Imaging*, vol. 26, pp. 1136–1153, 9 2007.

[72] R. M. Lang, L. P. Badano, V. Mor-Avi, J. Afilalo, A. Armstrong, L. Ernande, F. A. Flachskampf, E. Foster, S. A. Goldstein, T. Kuznetsova, P. Lancellotti, D. Muraru, M. H. Picard, E. R. Rietzschel, L. Rudski, K. T. Spencer, W. Tsang, and J.-U. Voigt, "Recommendations for cardiac chamber quantification by echocardiography in adults: An update from the american society of echocardiography and the european association of cardiovascular imaging," *Journal of the American Society of Echocardiography*, vol. 28, 1 –39.e14, 1 2015.

[73] D. Ni, Y. Qu, X. Yang, Y. P. Chui, T.-T. Wong, S. S. M. Ho, and P. A. Heng, "Volumetric ultrasound panorama based on 3d sift," in *Medical Image Computing and Computer-Assisted Intervention - MICCAI 2008*, ser. Lecture Notes in Computer Science, vol. 5242, Springer Berlin Heidelberg, 2008, pp. 52–60.

[74] D. Perperidis, R. H. Mohiaddin, and D. Rueckert, "Spatio-temporal free-form registration of cardiac mr image sequences," *Medical Image Analysis*, vol. 9, pp. 441 – 456, 5 2005.

[75] W. Zhang, J. A. Noble, and J. M. Brady, "Spatio-temporal registration of real time 3d ultrasound to cardiovascular mr sequences," in *Medical Image Computing and Computer-Assisted Intervention - MICCAI 2007*, ser. Lecture Notes in Computer Science, vol. 4791, Springer Berlin Heidelberg, 2007, pp. 343–350.

[76] A. Blake, R. Curwen, and A. Zisserman, "A framework for spatiotemporal control in the tracking of visual contours," *International Journal of Computer Vision*, vol. 11, pp. 127–145, 2 1993.

[77] A. Blake, M. Isard, and D. Reynard, "Learning to track the visual motion of contours," *Artificial Intelligence*, vol. 78, pp. 101–134, 1995.

[78] A. Blake and M. Isard, *Active Contours: The Application of Techniques from Graphics, Vision, Control Theory and Statistics to Visual Tracking of Shapes in Motion*. Springer-Verlag, 1998.

[79] G. Jacob, J. A. Noble, M. Mulet-Parada, and A. Blake, "Evaluating a robust contour tracker on echocardiographic sequences," *Medical Image Analysis*, vol. 3, pp. 63 – 75, 1 1999.

[80] G. Jacob, J. Noble, C. Behrenbruch, A. Kelion, and A. Banning, "A shape-space-based approach to tracking myocardial borders and quantifying regional left-ventricular function applied in echocardiography," *IEEE Transactions on Medical Imaging*, vol. 21, pp. 226–238, 3 2002.

[81] S. J. Julier and J. K. Uhlmann, "Unscented filtering and nonlinear estimation," *Proceedings of the IEEE*, vol. 92, pp. 401–422, 3 2004.

Paper I

Automatic Measurement of Aortic Annulus Diameter in 3-Dimensional Transoesophageal Echocardiography

BMC Medical Imaging, 2014, 14:*31.*

Jørn Bersvendsen [1,2,3], Jan O. Beitnes [4], Stig Urheim [4], Svend Aakhus [4] and Eigil Samset [1,2,3]

[1]GE Vingmed Ultrasound AS, Horten, Norway
[2]Department of Informatics, University of Oslo, Oslo, Norway
[3]Center for Cardiological Innovation, Oslo, Norway
[4]Department of Cardiology, Oslo University Hospital, Oslo, Norway

Abstract

Background: **Transcatheter aortic valve implantation involves percutaneously implanting a biomechanical aortic valve to treat severe aortic stenosis. In order to select a proper device, precise sizing of the aortic valve annulus must be completed.**
Methods: **In this paper, we describe a fully automatic segmentation method to measure the aortic annulus diameter in patients with aortic calcification, operating on 3-dimensional transesophageal echocardiographic images. The method is based on state estimation of a subdivision surface representation of the left ventricular outflow tract and aortic root. The state estimation is solved by an extended Kalman filter driven by edge detections normal to the subdivision surface.**
Results: **The method was validated on echocardiographic recordings of 16 patients. Comparison against two manual measurements showed agreements (mean±SD) of** -0.3 ± 1.6 **and** -0.2 ± 2.3 **mm for perimeter-derived diameters, compared to an interobserver agreement of** -0.1 ± 2.1 **mm.**
Conclusions: **With this study, we demonstrated the feasibility of an efficient and fully automatic measurement of the aortic annulus in patients with aortic disease. The algorithm robustly measured the aortic annulus diameter, providing measurements indistinguishable from those done by cardiologists.**

I.1 Background

Transcatheter Aortic Valve Implantation (TAVI) involves percutaneously implanting a biomechanical aortic valve to treat severe aortic stenosis. Because of its minimally invasive nature, TAVI is a viable alternative for patients who are at too high risk to undergo conventional surgical aortic valve replacement.

Precise sizing of the aortic annulus prior to TAVI is required for determining procedure eligibility and for selecting the correct implant size and type. Errors in prosthesis sizing may lead to complications during or after the procedure, such as Paravalvular Aortic Regurgitation (PAR) [1].

In current clinical practice, measurement of the annulus diameter before TAVI is typically done by 2D transthoracic echocardiography, 2D Transoesophageal Echocardiography (TEE) or Multi-Slice Computed Tomography (MSCT).

It has been shown that sizing based on MSCT, as opposed to 2D TEE, results in fewer instances of post operational PAR [2], as 2D modalities can fail to accurately describe the 3D structure of the aortic valve [3]–[5]. Strong correlations between 3D TEE and MSCT measurements of the annulus diameter [4] indicate feasibility of similar results for a method based on 3D TEE.

We propose an algorithm for automatic annulus measurements operating on 3D TEE images, using a real-time volumetric tracking and segmentation framework presented by

Orderud *et al.* [6], [7]. The framework uses an extended Kalman filter to solve a state space estimation formulation of the segmentation problem, and has been applied on the left ventricle.

In this paper, we apply the same framework to model the left ventricular outflow tract and aortic root. We propose a two-stage approach by performing segmentation based on a stiff and deformable surface sequentially. Combined with assimilation of forward and backward tracking, we obtain a fully automatic measurement of the aortic annulus diameter in 3D TEE images.

We validated our results by comparing automatic measurements of 16 recordings to manual measurements made by two cardiologists.

I.2 Methods

I.2.1 Segmentation

The method presented here is an application of a previously presented real-time volumetric segmentation framework, operating on deformable subdivision surfaces [6], [7]. The segmentation is represented as a state estimation problem and solved with an extended Kalman filter.

The filter is run iteratively over all frames in a heart cycle with a single iteration on each frame. For each frame, a motion model predicts the next estimate $\hat{\mathbf{x}}_{k|k-1}$. Edge detection is then done locally on the deformed model surface, and the prediction is updated with the measurement information, resulting in the state estimate $\hat{\mathbf{x}}_{k|k}$. This processing chain is illustrated in figure I.1.

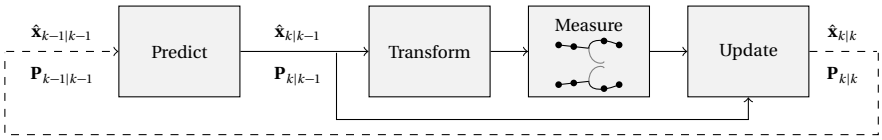

Figure I.1: State estimation KF processing chain. Figure adapted from [7]. $\hat{\mathbf{x}}_{k|j}$ and $\mathbf{P}_{k|j}$ denote the state and covariance estimates respectively, at time index k using measurements up to and including time index j.

Surface model

We use a cylindrical Doo-Sabin subdivision surface consisting of 5 connected circles of 6 uniformly distributed control points to represent the Left Ventricular Outflow Tract (LVOT) and aortic root, illustrated in figure 3(g). A subdivision surface has the advantage of being highly deformable but parameterized by only a few states, making the state space estimation an efficient approach.

The surface is deformed locally by displacing each control point in the direction normal to the cylinder long axis, to maximize deformation per degree of freedom. The local deformation transform is denoted $\mathbf{T}_l(\mathbf{p};\mathbf{x}_l)$, where $\mathbf{x}_l$ is the state vector of local deformations.

A global transform

$$\mathbf{T}_g(\mathbf{p};\mathbf{x}_g) = s\mathbf{R}_x(\theta_x)\mathbf{R}_y(\theta_y)\mathbf{R}_z(\theta_z)\mathbf{p} + [t_x,\, t_y,\, t_z]^\top \tag{I.1}$$

where $\mathbf{x}_g = [t_x,\, t_y,\, t_z,\, s,\, \theta_x, \theta_y, \theta_z]^\top$ is the global transform state vector, allows for translation, scaling and rotation of the model. The composite transform is given by $\mathbf{T}(\mathbf{p};\mathbf{x}) = \mathbf{T}_g(\mathbf{T}_l(\mathbf{p};\mathbf{x}_l);\mathbf{x}_g)$ where $\mathbf{x}^\top = \left[\mathbf{x}_g^\top, \mathbf{x}_l^\top\right]$ is the state vector.

The aortic annulus plane is represented by a disc placed in the middle of the surface model. The disc shares the same global transform $\mathbf{T}_g$ but is not deformable.

Motion model

The time domain dynamics of the model is inferred in the Kalman filter prediction step. We use a combination of the previous estimate $\hat{\mathbf{x}}_{k-1|k-1}$ and a regularization state $\hat{\mathbf{x}}_{0,k}$ to predict the next estimate by

$$\hat{\mathbf{x}}_{k|k-1} = \mathbf{A}\hat{\mathbf{x}}_{k-1|k-1} + (\mathbf{I}-\mathbf{A})\mathbf{x}_{0,k}\,, \tag{I.2}$$

where $\mathbf{A}$ is a diagonal matrix specifying the regularization strength for each state. Note that $0 \leq a_{ij} \leq 1$ ensures stability. The diagonal elements of $\mathbf{A}$ were chosen separately for translation, scaling, rotation and deformation states.

The covariance matrix of the estimate is predicted by

$$\mathbf{P}_{k|k-1} = \mathbf{A}\mathbf{P}_{k-1|k-1}\mathbf{A}^\top + \mathbf{Q}_{0,k}\,, \tag{I.3}$$

where $\mathbf{Q}_0$ is the process noise covariance matrix. A low noise value will decrease the prediction covariance relative to the measurement covariance, which in turn will make the Kalman filter rely more on the previous estimate than the detected edges. $\mathbf{Q}_0$ therefore functions as a fairness parameter.

Edge detection

300 evenly distributed points on the model surface are defined. For the valve disc, 40 edge points are defined.

After applying $\mathbf{T}_l$, each edge point $\mathbf{p}_l$ is extracted with associated unit normal $\mathbf{n}_l$ and Jacobian matrix $\mathbf{J}_l$. These are then transformed to the global space by

$$\mathbf{p}_g = \mathbf{T}_g(\mathbf{p}_l;\hat{\mathbf{x}}) \tag{I.4}$$

$$\mathbf{n}_g = |\mathbf{M}|\mathbf{M}^{-\top}\mathbf{n}_l \text{ where } \mathbf{M} = \left.\frac{\partial \mathbf{T}_g(\mathbf{p};\mathbf{x})}{\partial \mathbf{p}}\right|_{\substack{\mathbf{p}_l \\ \hat{\mathbf{x}}}} \tag{I.5}$$

$$\mathbf{J}_g = \left[\left.\frac{\partial \mathbf{T}_g(\mathbf{p};\mathbf{x})}{\partial \mathbf{x}}\right|_{\substack{\mathbf{p}_l \\ \hat{\mathbf{x}}}}, \left.\frac{\partial \mathbf{T}_g(\mathbf{p},\mathbf{x})}{\partial \mathbf{p}}\right|_{\substack{\mathbf{p}_l \\ \hat{\mathbf{x}}}} \mathbf{J}_l\right]. \tag{I.6}$$

where $\hat{\mathbf{x}} = \hat{\mathbf{x}}_{k|k-1}$.

Edge displacements are detected by searching along $\mathbf{n}_g$ around $\mathbf{p}_g$ using the least mean squares fit to an intensity step or peak function. Outlier edges are rejected based on the intensity step function height and differences between neighboring edges. The capture range is determined by the search length along $\mathbf{n}_g$.

Each measured edge displacement v_i has an associated measurement noise with estimated variance r_i which is the sum of squared deviations in the intensity fit. The variance estimates are normalized such that $\sum_i r_i = r_{edge}$.

Measurement update

To relate the edge displacement v_i to changes in the state vector, the measurement vector $\mathbf{h}_i^\top = \mathbf{n}_i^\top \mathbf{J}_i$ is calculated, where $\mathbf{J}_i$ is the global Jacobian evaluated at $\mathbf{p}_i$ for $\hat{\mathbf{x}}_{k|k-1}$. By assuming that all measurement noises are independent, the Kalman filter update step can be written as [7]

$$\mathbf{P}_{k|k}^{-1} = \mathbf{P}_{k|k-1}^{-1} + \sum_i \mathbf{h}_i \, r_i^{-1} \mathbf{h}_i^\top \tag{I.7}$$

$$\hat{\mathbf{x}}_{k|k} = \hat{\mathbf{x}}_{k|k-1} + \mathbf{P}_{k|k} \sum_i \mathbf{h}_i \, r_i^{-1} \, v_i \, . \tag{I.8}$$

This computation is efficient as it does not require inversion of matrices with size dependent on the number of measurements.

Forward and backward tracking

A common problem with segmentation of time-series is that the segmentation lags behind the recording. We solve this by tracking forward and backward in time.

The Kalman filter is iterated forward over frames $k = 1, 2, \ldots, N$ to produce estimate $\mathbf{x}_{f,k}$ with estimated covariance $\mathbf{P}_{f,k}$. Backwards iteration over frames $k = N, N-1, \ldots, 1$ produces $\mathbf{x}_{b,k}$ and $\mathbf{P}_{b,k}$. The forward and backward state estimates are then assimilated by

$$\mathbf{P}_k = \left(\mathbf{P}_{f,k}^{-1} + \mathbf{P}_{b,k}^{-1} \right)^{-1} \tag{I.9}$$

$$\hat{\mathbf{x}}_k = \mathbf{P}_k \left(\mathbf{P}_{f,k}^{-1} \hat{\mathbf{x}}_{f,k} + \mathbf{P}_{b,k}^{-1} \hat{\mathbf{x}}_{b,k} \right) . \tag{I.10}$$

This bidirectional tracking makes the segmentation robust to significant movement of the LVOT and aortic root during the cardiac cycle.

Two-phase segmentation

The described tracking algorithm is run in two passes; stiff segmentation and deformable segmentation.

Stiff segmentation In the first pass, the subdivision surface is made stiff by removing all deformation states. The initial mesh is then oriented along an estimated LVOT long axis, derived from the ultrasound recorded roll angle.

The Kalman filter iterates over each consecutive frame once to ensure rough convergence. This is then repeated for the actual segmentation. A simplified motion model is used where $\mathbf{x}_{0,k} = \mathbf{x}_0$ and $\mathbf{Q}_{0,k} = \mathbf{Q}_0$ are constant during the cardiac cycle. $\mathbf{Q}_0$ was chosen to be a diagonal matrix of process noise standard deviations.

The resulting global pose states $\hat{\mathbf{x}}_{\text{stiff},k}$, with estimated covariance $\mathbf{P}_{\text{stiff},k}$, aligns the subdivision surface to the recording for each frame. This captures the global movement of the LVOT and aortic root during the cardiac cycle.

Deformable segmentation After stiff segmentation, the deformation states are reintroduced. The state vectors $\hat{\mathbf{x}}_{\text{stiff},k}$ and covariance matrices $\mathbf{P}_{\text{stiff},k}$ from the stiff segmentation are used for $\mathbf{x}_{0,k}$ and $\mathbf{Q}_{0,k}$ in the motion model. Bidirectional tracking is performed over a single heart cycle.

Different prediction parameters $\mathbf{A}$ are used in the stiff and deformable phases to reflect the increased confidence of the global transform states after stiff segmentation. For deformable segmentation, the regularization strength $\mathbf{A}$ is increased for the these states, ensuring that the movement of the aortic structure is tracked.

Automatic annulus measurements

The aortic annulus is extracted by the intersection of the deformed surface model and the aortic valve disk. An ellipse is fitted to the intersection points by least mean squares optimization and the major and minor axes, area and perimeter are extracted.

The mid systolic frame was defined as the frame with maximum detected aortic annulus area.

I.2.2 Transoesophageal echocardiography

Acquisition

16 anonymous 3D TEE recordings were provided retrospectively by the Oslo University Hospital for validation. Patient characteristics are shown in table I.1. The dataset contained both tri- and bicuspid aortic valves with varying degrees of stenosis and insufficiency. The images were acquired in mid-esophageal position using zoom mode and showed the LVOT, aortic valve and aortic root. All images were recorded on a Vivid E9 scanner with a 6 VT-D probe and all analysis was done using EchoPAC version 112.1.0 (GE Vingmed Ultrasound AS, Horten Norway).

Manual measurements

The aortic annulus was manually measured by two cardiologists. The annulus plane was visualized using 3 orthogonal planes in mid systole. A sagittal and a coronal plane bi-

Table I.1: Patient characteristics.

Age*, yr	69±16
Sex*, male/female	7/6
Disease, n	
Aortic stenosis	12
Aortic insufficiency	2
Normal	2
Aortic morphology, n	
Tricuspid	14
Bicuspid	2
LV EF < 50 %*, n	3

*Age, sex and LV EF were unknown for 3 patients.

sected the long axis of the LVOT and a transverse plane bisected the lowest insertion points of all 3 aortic cusps, as shown in figure I.3(a-c). The annulus diameter was measured in the sagittal and coronal long axis planes. Area and perimeter were measured by manual trace in the short axis plane. The manual observers where blinded to each other and the results from the automatic measurements.

I.2.3 Sensitivity analysis

To assess the robustness of the algorithm with respect to the roll-angle derived initial LVOT long axis estimate, the following test was carried out. For a single recording, the initial state $\mathbf{x}_0$ prior to stiff segmentation was randomly perturbed 500 times, and the resulting perimeter-derived annulus diameter distributions were recorded. This was done separately for perturbations to translation and rotation.

Translation The perturbations were on the form $d\,\mathbf{n}/||\mathbf{n}||$ where the elements of $\mathbf{n} \in \mathbb{R}^3$ were uniformely distributed. The analysis was repeated for each $d = 2, 4, \ldots, 12$ mm, which is within the capture range of ±14 mm.

Rotation For each iteration, a vector $\mathbf{n}/||\mathbf{n}||$ was generated, where the elements of $\mathbf{n} \in \mathbb{R}^3$ were uniformely distributed. The initial model was then rotated an angle ϕ about the line $\mathbf{v}(t) = \mathbf{v}_0 + \mathbf{n}t$ where $\mathbf{v}_0$ is the initial annulus center. The analysis was repeated for each $\phi = 1, 2, \ldots, 15$ deg.

To assess robustness with respect to scaling, the segmentation was repeated for 100 linearly spaced initial annulus diameters $D_0 \in [15, 35]$ mm.

I.2.4 Statistical analysis

Agreement between the automatic method and the two manual observers was analyzed using Blant and Altmans method and two-way absolute agreement intraclass correlation

coefficients. All statistical analysis was performed using IBM SPSS Statistics for Windows, Version 20.0 (IBM Corp., Armonk, NY, USA).

I.3 Results

The described algorithm was executed on all 16 3D TEE datasets. The segmentation time was (mean±SD) 9.9 ± 7.3 s on a standard laptop.

I.3.1 Sensitivity analysis

Figure I.2 shows the results of the sensitivity analysis for translational and rotational perturbations in the initial state. The sample standard deviations of the resulting diameter distributions were ≤ 0.29, ≤ 0.28 and 0.10 mm for the translation, rotation and scaling sensitivity tests respectively.

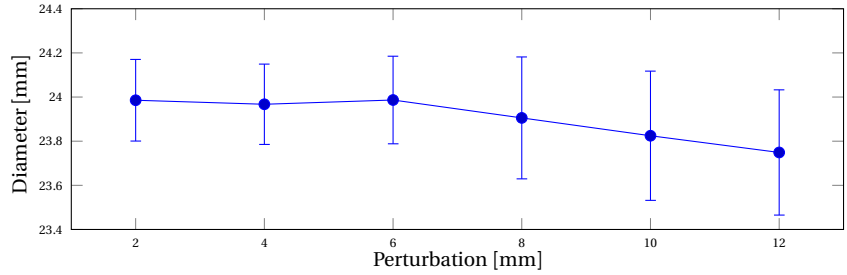

(a) Translational perturbation

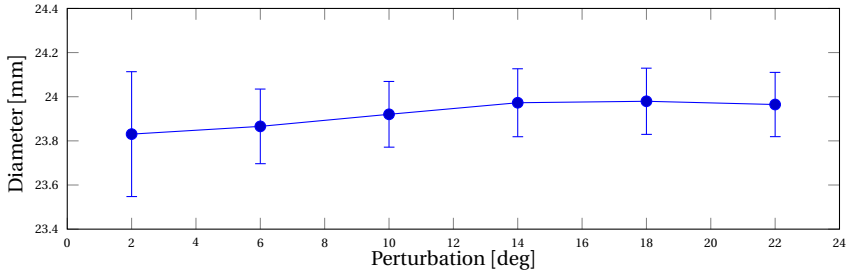

(b) Rotational perturbation

Figure I.2: Results of global registration sensitivity analysis. The plot shows the mean and standard deviation of the output diameter distributions as a function of translational and rotational perturbations.

I.3.2 Comparison of manual and automatic measurements

Comparisons of manual and automatic measurements are shown in tables I.2, I.3 and figure I.4. Figure I.3 shows an example of the manual and automatic measurements.

The interobserver Intraclass Correlation Coefficients (ICC) were 0.78 and 0.77 for perimeter and area derived diameters respectively. The intraclass correlation coefficients between the automatic method and each of the manual observers were 0.87 and 0.75 for the perimeter derived diameters and 0.85 and 0.74 for the area derived diameters.

Table I.2: Automatic and manual measurements of arotic annulus diameters. Values are mean±SD [mm]. D_{auto}, D_1 and D_2 denote automatic and manual measurements from the the first and second observer respectively.

	D_{auto}	D_1	D_2
Minimum	24.3 ± 3.0		
Maximum	26.8 ± 3.5		
Sagittal		23.9 ± 2.7	23.9 ± 3.1
Coronal		25.4 ± 3.3	25.3 ± 3.0
Area-derived	25.5 ± 3.2	24.9 ± 3.0	25.0 ± 3.1
Perimeter-derived	25.6 ± 3.2	25.9 ± 3.2	25.8 ± 3.1

Table I.3: Comparison of automatic and manual measurements of arotic annulus diameter. Biases are mean±SD [mm]. D_{auto}, D_1 and D_2 denote automatic and manual measurements from the the first and second observer respectively.

	Bias	Intraclass Correlation
Sagittal		
D_1 versus D_2	0.063 ± 1.5	0.88
Coronal		
D_1 versus D_2	0.063 ± 2.4	0.74
Perimeter-derived		
D_{auto} versus D_1	-0.35 ± 1.6	0.87
D_{auto} versus D_2	-0.23 ± 2.3	0.75
D_1 versus D_2	0.12 ± 2.1	0.78
Area-derived		
D_{auto} versus D_1	0.62 ± 1.7	0.85
D_{auto} versus D_2	0.46 ± 2.3	0.74
D_1 versus D_2	-0.16 ± 2.1	0.77

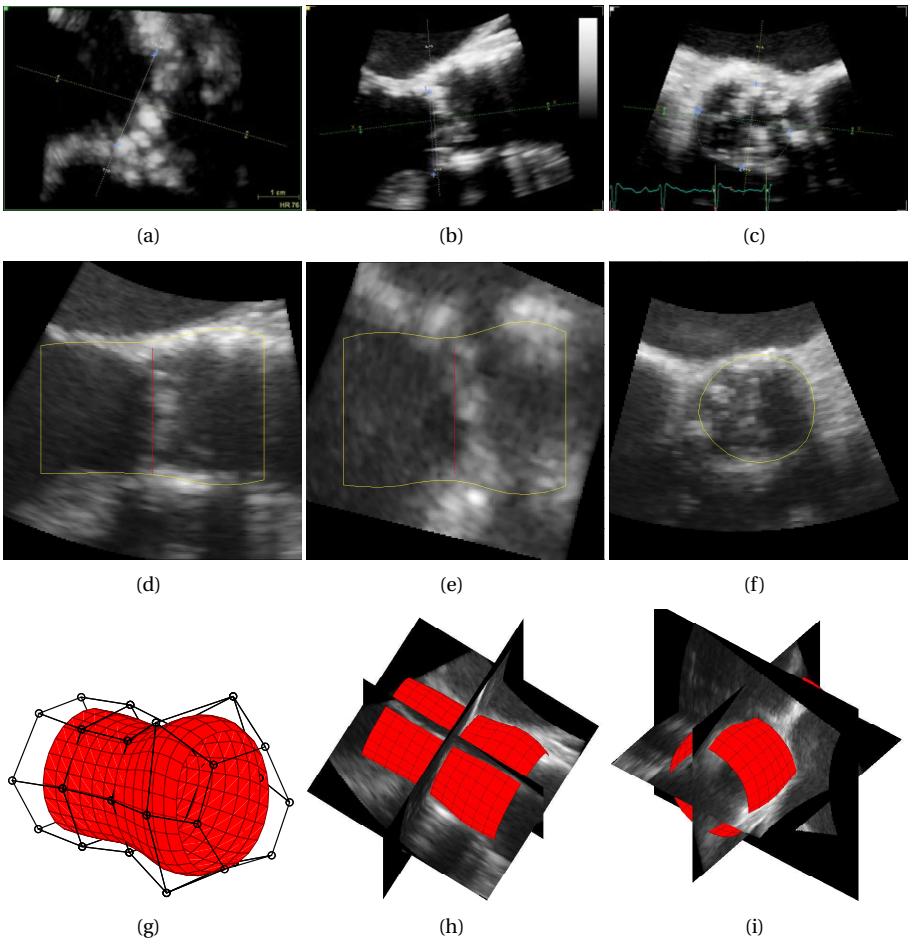

Figure I.3: Manual (a-c) and automatic (d-f) measurements of the aortic valve annulus in a 3D TEE recording. Initial (g) and deformed (h-i) subdivision surface.

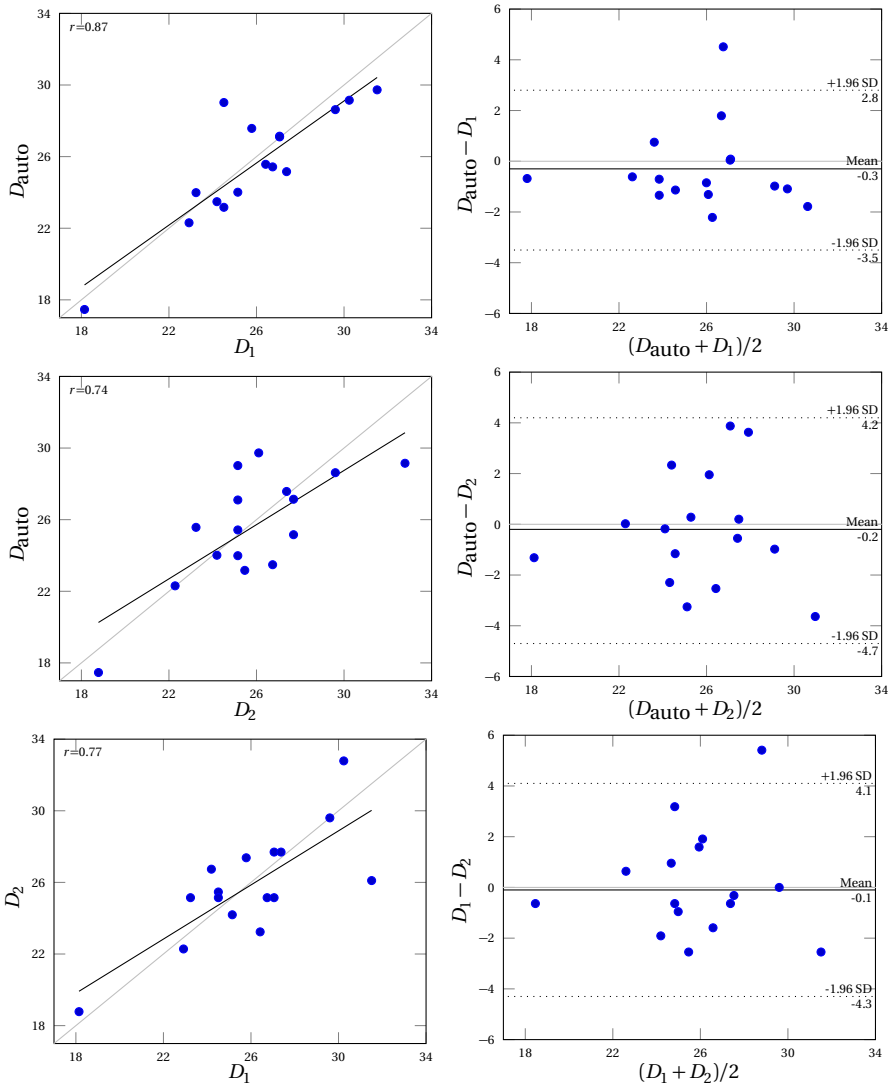

Figure I.4: Comparison of automatic and manual perimeter-derived measurements. All diameters are [mm]. D_{auto}, D_1 and D_2 denote automatic and manual measurements from the the first and second observer respectively.

I.4 Discussion

I.4.1 Sensitivity analysis

Even for significant perturbations (±12 mm translation, ±15 deg rotation or ±10 mm initial annulus diameter), the standard deviation of the automatic measurement was significantly lower than the interobserver variation. This indicates that the algorithm is robust with respect to errors in the initial LVOT long axis derived from the recorded roll angle, as well as the assumed initial annulus diameter.

I.4.2 Comparison of manual and automatic measurements

The algorithm performance was indistinguishable from human observers' performance. The automatic algorithm successfully segmented the LVOT and aortic root and measured the aortic annulus diameter in all 16 images, with mean computation time 9.9 s. Interobserver correlation coefficient for the manual measurements was comparable to that reported by others [4]. The correlation and deviation between the automatic and each manual measurements were comparable to the interobserver reliability.

Perimeter-derived measurements showed the closest agreement with the manual observers. Since the perimeter-derived diameter changes the least during the cardiac cycle [8], this measurement should not be affected by errors in mid-systole detection. This is therefore a more robust measurement compared to area, major and minor diameters, and was chosen as the algorithm's main output diameter.

The annulus plane is normally defined as the plane spanned by the hinge points of the three valve cusps. However, the hinge points are not explicitly defined in the described model. Because the disk representing the aortic valve is non-deformable and shares the same pose transform as the surface model, the detected annulus will align perpendicular to the long axis of the LVOT.

Since the hinge point plane and the perpendicular plane are closely aligned, we propose that a perpendicular plane is a good estimation of the anatomical annulus plane. In the rare cases where these planes are not aligned, we submit that a perpendicular plane is of clinical relevance since a prosthetic valve is more likely to align with the LVOT long axis than the native valve's hinge points.

The largest absolute deviation between the two manual observers was 5.4 mm. Poor image quality, low frame rate (7.7 vps) and a wide sinus of Valsalva lead to the significant interobserver deviation. The largest absolute deviation between automatic and manual measurements was 5.5 mm. In this case, the automatic method grossly overestimated the annulus diameter, resulting from a very wide sinus of Valsalva combined with dropouts close to the annulus. Although these discrepancies would indicate a difference in device selection, it is extremely unlikely that these specific images would be used as the basis of device selection.

Two recordings had visible stitching artifacts. In both recordings all absolute deviations between the the automatic and manual measurements were ≤0.6 mm, indicating

robustness against stitching artifacts.

Recently, a validation study of the first description of an automated aortic root modeling and quantification algorithm for 3D TEE images was published [9]. The study reported annulus diameter agreement (mean±SD) of 1.1 ± 1.3 and 3.6 ± 2.3 mm for sagittal and coronal diameters respectively, which is comparable to our results. However, manual identification of peak systole and end diastole was required, and manual segmentation adjustments were needed in 23 of 69 TEE recordings. The reported interobserver variability was 0.2 ± 0.56 and 0.0 ± 0.61 mm. Although our presented algorithm is fully automatic and therefore has no interobserver variability, these values are comparable to our sensitivity analysis results. The reported computation and adjustment time was 2.3 ± 0.6 minutes, which is significantly longer than our results.

This method is based on machine learning and statistical shape models [10]. However, these algorithms require a large database of recordings annotated with manual ground truth segmentations. The presented method is simpler and does not rely on a history of previous segmentations.

Within the presented framework, there are several quality measures available that can potentially be used to automatically identify poor segmentations, e.g. number of discarded edge profiles, deviation from segmentation surface to detected edges or the state covariance estimates. These should be further investigated with an available gold standard to create criteria that can automatically judge the segmentation quality.

This study used a limited sample size of 16 patients. Further studies with a larger number of patients should be performed. Comparison of measurements in prospective 3D TEE images with ECG gated Multi-Slice Computed Tomography (MSCT) gold standard should be carried out to investigate if the algorithm can render MSCT superfluous for a significant portion of TAVI candidates.

I.5 Conclusions

With this study, we demonstrated the feasibility of an efficient and fully automatic measurement of the aortic annulus in patients with aortic disease. The algorithm robustly measured the aortic annulus diameter, providing measurements indistinguishable from those done by cardiologists.

Acknowledgements

The authors gratefully acknowledge the Research Council of Norway for their research grant, as well as the support of Center for Cardiological Innovation, funded by the Research Council of Norway.

References

[1] J. L. Zamorano, L. P. Badano, C. Bruce, K.-L. Chan, A. Gonçalves, R. T. Hahn, M. G. Keane, G. La Canna, M. J. Monaghan, P. Nihoyannopoulos, F. E. Silvestry, J.-L. Vanoverschelde, L. D. Gillam, A. Vahanian, V. Di Bello, and T. Buck, "Eae/ase recommendations for the use of echocardiography in new transcatheter interventions for valvular heart disease.," *European Heart Journal*, vol. 12, pp. 557–84, 8 Aug. 2011.

[2] H. Jilaihawi, M. Kashif, G. Fontana, A. Furugen, T. Shiota, G. Friede, R. Makhija, N. Doctor, M. B. Leon, and R. R. Makkar, "Cross-sectional computed tomographic assessment improves accuracy of aortic annular sizing for transcatheter aortic valve replacement and reduces the incidence of paravalvular aortic regurgitation," *Journal of the American College of Cardiology*, vol. 59, pp. 1275–1286, 14 Apr. 2012.

[3] A. C. T. Ng, V. Delgado, F. van der Kley, M. Shanks, N. R. L. van de Veire, M. Bertini, G. Nucifora, R. J. van Bommel, L. F. Tops, A. de Weger, G. Tavilla, A. de Roos, L. J. Kroft, D. Y. Leung, J. Schuijf, M. J. Schalij, and J. J. Bax, "Comparison of aortic root dimensions and geometries before and after transcatheter aortic valve implantation by 2- and 3-dimensional transesophageal echocardiography and multislice computed tomography.," *Circulation: Cardiovascular imaging*, vol. 3, pp. 94–102, 1 Jan. 2010.

[4] E. Altiok, R. Koos, J. Schröder, K. Brehmer, S. Hamada, M. Becker, A. H. Mahnken, M. Almalla, G. Dohmen, R. Autschbach, N. Marx, and R. Hoffmann, "Comparison of two-dimensional and three-dimensional imaging techniques for measurement of aortic annulus diameters before transcatheter aortic valve implantation.," *Heart*, vol. 97, pp. 1578–84, 19 Oct. 2011.

[5] D. Muraru, L. P. Badano, M. Vannan, and S. Iliceto, "Assessment of aortic valve complex by three-dimensional echocardiography: a framework for its effective application in clinical practice.," *European Heart Journal - Cardiovascular Imaging*, vol. 13, pp. 541–55, 7 Jul. 2012.

[6] F. Orderud and S. I. Rabben, "Real-time 3d segmentation of the left ventricle using deformable subdivision surfaces," in *Computer Vision and Pattern Recognition, 2008. IEEE Conference on*, Norwegian Univ. of Sci. & Technol., Trondheim, IEEE, Jun. 2008.

[7] F. Orderud, "A framework for real-time left ventricular tracking in 3d+t echocardiography, using nonlinear deformable contours and kalman filter based tracking," in *Computers in Cardiology, 2006*, IEEE, 2006, pp. 125–128.

[8] A. Hamdan, V. Guetta, E. Konen, O. Goitein, A. Segev, E. Raanani, D. Spiegelstein, I. Hay, E. Di Segni, M. Eldar, and E. Schwammenthal, "Deformation dynamics and mechanical properties of the aortic annulus by 4-dimensional computed tomography: insights into the functional anatomy of the aortic valve complex and implications for transcatheter aortic valve therapy.," *Journal of the American College of Cardiology*, vol. 59, pp. 119–27, 2 Jan. 2012.

[9] A. Calleja, P. Thavendiranathan, R. I. Ionasec, H. Houle, S. Liu, I. Voigt, C. Sai Sudhakar, J. Crestanello, T. Ryan, and M. A. Vannan, "Automated quantitative 3-d modeling of the aortic valve and root by 3-d transesophageal echocardiography in normals, aortic regurgitation and, aortic stenosis: Comparison to computed tomography in normals and clinical implications," *Circulation: Cardiovascular Imaging*, 2012.

[10] R. Ionasec, I. Voigt, B. Georgescu, Y. Wang, H. Houle, F. Vega-Higuera, N. Navab, and D. Comaniciu, "Patient-specific modeling and quantification of the aortic and mitral valves from 4-d cardiac ct and tee," *IEEE Transactions on Medical Imaging*, vol. 29, pp. 1636–1651, 9 2010.

Paper II

Automated Segmentation of the Right Ventricle in 3D Echocardiography: A Kalman Filter State Estimation Approach

IEEE Transactions on Medical Imaging, 2016, 35*:1.*

Jørn Bersvendsen [1,2,3], Fredrik Orderud [1], Richard J Massey [4], Kristian Fosså [5], Olivier Gerard [1], Stig Urheim [4,6] and Eigil Samset [1,2,3]

[1]GE Vingmed Ultrasound AS, Horten, Norway
[2]Dept. of Informatics, University of Oslo, Oslo, Norway
[3]Center for Cardiological Innovation, Oslo, Norway
[4]Dept. of Cardiology, Oslo University Hospital, Oslo, Norway
[5]Dept. of Radiology and Nuclear Medicine, Oslo University Hospital, Oslo, Norway
[6]Institute for Surgical Research, Oslo University Hospital, Oslo, Norway

Abstract

As the Right Ventricle's (RV) role in cardiovascular diseases is being more widely recognized, interest in RV imaging, function and quantification is growing. However, there are currently few RV quantification methods for 3D echocardiography presented in the literature or commercially available. In this paper we propose an automated RV segmentation method for 3D echocardiographic images. We represent the RV geometry by a Doo-Sabin subdivision surface with deformation modes derived from a training set of manual segmentations. The segmentation is then represented as a state estimation problem and solved with an extended Kalman filter by combining the RV geometry with a motion model and edge detection. Validation was performed by comparing surface-surface distances, volumes and ejection fractions in 17 patients with aortic insufficiency between the proposed method, Magnetic Resonance Imaging (MRI), and a manual echocardiographic reference. The algorithm was efficient with a mean computation time of 2.0 s. The mean absolute distances between the proposed and manual segmentations were 3.6 ± 0.7 **mm. Good agreements of end diastolic volume, end systolic volume and ejection fraction with respect to MRI (**-26 ± 24 **mL,** -16 ± 26 **mL and** 0 ± 10 **% respectively) and a manual echocardiographic reference (**7 ± 30 **mL,** 13 ± 17 **mL and** -5 ± 7 **% respectively) were observed.**

II.1 Introduction

Compared to the Left Ventricle (LV), image processing methods of the Right Ventricle (RV) are infrequently reported in the literature. However, as the RV's role in cardiovascular diseases is being more widely recognized, interest in RV function and imaging is growing. For instance, accurate assessment of the RV has been shown to be important in patients with pulmonary hypertension or LV dysfunction [1], [2].

In current clinical practice, manual measurements in Magnetic Resonance Imaging (MRI) are considered the gold standard for quantitative assessment of RV volumes and ejection fraction [1]. However, MRI is seldom routinely available, and in some cases contraindicated. Furthermore, since manual assessment is time consuming and subject to inter-observer variability, automated methods are preferred. In the last decade, Three-Dimensional Transthoracic Echocardiography (3DTTE) has emerged as an alternative for assessing the RV.

Automated segmentation of the RV is largely an unsolved problem, and sparsely reported in the literature for both 3DTTE and MRI. For MRI, the problem is typically solved with a bi-ventricular segmentation method [3]. Methods using a strong prior, such as deformable models [4], active shape models [5] or atlases [6]–[9], and image based methods with and without anatomical priors [10]–[13] have been proposed.

For 3DTTE, Angelini *et al.* [14] have presented a level-set framework for segmentation of both LV and RV. The LV and RV surfaces are implicitly represented as the zero-

intersection of a higher order function, which is fitted to the image by energy minimization. Stebbing *et al.* [15] has described a segmentation method using an explicit Loop subdivision surface model of the RV and solving the fitting problem with energy minimization. Missing edges and information of RV shape in the target population is implicitly handled by solving the energy minimization simultaneously in either multiple views of the same patient, or across multiple patients. Commercially, the only widely available tool for RV segmentation in 3DTTE is the TomTec 4D RV-Function software (TomTec Imaging Systems, Munich, Germany). Although the tool has been extensively validated in the literature [16]–[21], the details of the underlying method have not been published.

Segmentation of the LV in 3DTTE has received much more attention in the literature, and methods based on deformable models [22], [23], active shape models [24], active appearence models [25], level-set methods [14], and classification [26] have been presented. However, these methods are not immediately applicable to the RV, as there are several challenges that are especially demanding in this case, such as an increased anatomical complexity and larger inter-patient variation. For echocardiography in particular, challenges such as weaker myocardial borders, thin walls, pronounced trabeculations and reduced image quality make the problem even harder. Furthermore, 3DTTE acquisition of the whole RV is generally challenging. For instance, the anterior part of the RV outflow tract (RVOT) and anterio-lateral RV free wall is typically shadowed by the sternum or lung tissue [21].

In this paper we present a computationally efficient RV segmentation algorithm for 3DTTE images. The algorithm is based on a real-time segmentation framework previously applied to the LV [22]. We represent the RV anatomy using a compact geometric model with modes of variation derived from manual segmentations in MRI sequences. The segmentation problem is then solved by state estimation using a Kalman filter to combine the geometric model with edge detections and a motion model. Evaluation of the method was performed by comparing volumes and ejection fractions in 17 clinical cases to MRI and a state-of-the-art commercial 3DTTE RV assessment tool, as well as surface-surface distance metrics with respect to manual segmentations in 3DTTE.

II.2 Methods

The method presented here is an application of a previously published real-time volumetric segmentation framework that has been applied to the left ventricle [22], [27] and aortic root [28]. In this framework, a compact geometric representation of the target anatomy is fitted to the image by fusing information from the shape prior, edge detection, and motion prediction using an extended Kalman filter. The underlying RV geometry is represented by a subdivision surface and extended with a Statistical Shape Model (SSM) derived from manual segmentations in cine MRI images.

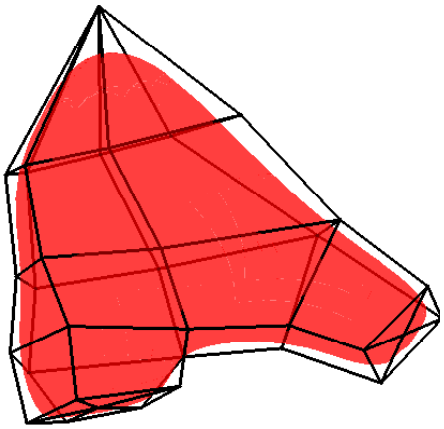

Figure II.1: Control polyhedron and resulting Doo-Sabin surface representation of the right ventricle.

II.2.1 Model

Surface Model

We represent the underlying RV geometry with a Doo-Sabin subdivision surface. This type of surface is a generalization of a uniform quadratic B-spline for arbitrary topology, defined by a control polyhedron which is interpolated to create a smooth surface.

Orderud *et al.* [27] have described a computationally efficient method of calculating the basis functions at arbitrary surface locations. For a location (u, v) on the surface defined by a control polyhedron with vertices $\mathbf{U} = [\mathbf{u}_1, \mathbf{u}_2, \cdots, \mathbf{u}_N]$, the transformed point $\mathbf{p} \in \mathbb{R}^3$ is given by

$$\mathbf{p}(u, v) = \sum_i^N b_i(u, v)\mathbf{u}_i = \mathbf{U}\mathbf{b}(u, v). \tag{II.1}$$

where $\mathbf{b}$ is a vector of basis functions. This surface deformation is denoted $\mathbf{T}_s(\mathbf{U})$. Note that the basis functions are uniquely defined by the topology of the control polyhedron, which means they can be precomputed for a given surface distribution. This is important for computational efficiency [27]. The RV subdivision surface is defined by a control polyhedron consisting of 32 vertices; 12 on the lateral free wall, 9 at the septum, 5 at the Tricuspid Valve (TV) annulus, 5 at the Pulmonary Valve (PV) annulus and 1 at the apex. Figure II.1 shows the control polyhedron and the resulting surface.

Hinge transform

One of the anatomical variations of the RV is the orientation of the Right Ventricle Outflow Tract (RVOT) with respect to the RV long axis. In order to capture this variability in a natural way, we introduce a hinge transform for the pulmonary valve control vertices. This

transform is a rotation about the apex-PV-TV plane normal direction and a displacement in the RVOT long axis, as demonstrated in figure II.2.

The hinge transform $\mathbf{V} = \mathbf{T}_h(\mathbf{x}_h, \mathbf{U})$ is applied by transforming the control vertices $\mathbf{U}$,

$$\mathbf{v}_i = \begin{cases} \mathbf{R}(\theta_h)\mathbf{u}_i + d_h \mathbf{d}_{\text{RVOT}} & \text{if } i \in \Omega_H \\ \mathbf{u}_i & \text{otherwise} \end{cases}, \tag{II.2}$$

where $\mathbf{x}_h = [\theta_h, d_h]$ are the rotation and displacement parameters and Ω_H is the set of control vertices for which the hinge applies.

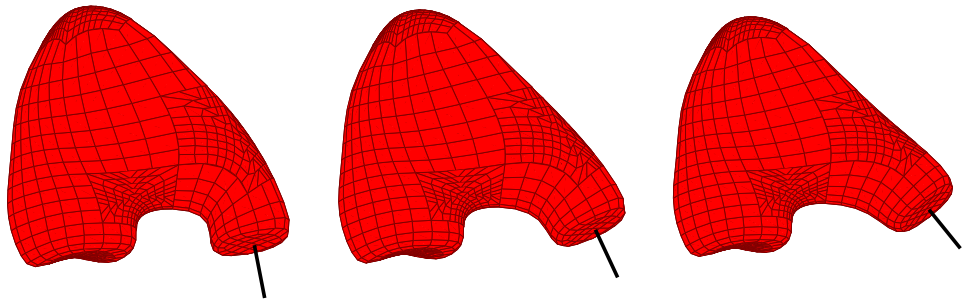

Figure II.2: Mean model with changing hinge transform parameter. From left to right: $-15°$, 0 and $15°$ rotations. The black line illustrates the normal direction of the pulmonary valve, for reference.

Statistical Shape Model

Statistical Shape Models (SSM) have been established as a robust tool for modeling cardiac structures [29]. By building a statistical model from manual segmentations, one can introduce strong prior shape information while simultaneously handling shape variation in a natural way. SSMs are normally constructed by performing Principal Component Analysis (PCA) on a training matrix whose rows are coordinates for all landmarks in manually segmented point distribution models. This results in a set of modes of variation $\boldsymbol{\phi}_m$ such that any valid shape $\mathbf{x}$ can be approximated by

$$\hat{\mathbf{x}} = \bar{\mathbf{x}} + \sum_i \beta_i \boldsymbol{\phi}_i, \tag{II.3}$$

where $\bar{\mathbf{x}}$ is the mean model and β_i are the shape parameters.

We derived the mean model and statistical modes of variation from manual segmentations of short axis cine-MRI recordings from an open access database [30]. 14 patients with high quality RV images were selected from the database, constituting 5 patients with myocardial infarction, 4 with non-infarct heart failure, 3 with hypertrophy and 2 healthy subjects. Stack misalignment was corrected by fitting the LV center points to a second

order polynomial [31]. All recordings consisted of 20 phases resulting in a total of 280 images.

For each reference MRI image, the RV endocardial borders were manually traced in all slices, and the pulmonary valve center, tricuspid valve center and RV apex landmarks were identified, resulting in a set of manual trace points $\mathcal{P} = \{\mathbf{p}_i\}$. The Doo-Sabin surface was fitted to each trace set by minimizing the sum of Euclidean distances between $\mathcal{P}$ and corresponding surface points,

$$\left(\hat{\mathbf{U}}, \hat{\mathbf{x}}_h\right) = \arg\min_{\mathbf{U},\mathbf{x}_h} \frac{1}{2} \sum_{i \in \mathcal{P}} \|\mathbf{p}_i - \mathbf{q}_i\|^2 , \tag{II.4}$$

where $\mathbf{q}_i$ is the projection onto the surface $\mathbf{T}_s(\mathbf{T}_h(\mathbf{U}, \mathbf{x}_h))$ of the trace point $\mathbf{p}_i$. The optimization was solved using gradient descent,

$$\hat{\mathbf{y}}_{k+1} \quad = \quad \hat{\mathbf{y}}_k + \lambda \sum_i (\mathbf{p}_i - \mathbf{q}_i)^\top \, \mathbf{J}_i|_{\hat{\mathbf{y}}_k} , \tag{II.5}$$

where

$$\mathbf{y} = \left[\mathbf{x}_h^\top, \mathbf{u}_1^\top, \mathbf{u}_2^\top, \cdots, \mathbf{u}_N^\top\right]^\top \tag{II.6}$$

is a vector of optimization variables, and $\mathbf{J}_i$ is the associated Jacobian matrix

$$\mathbf{J}_i = \frac{\partial \mathbf{q}_i}{\partial \mathbf{y}} = \left[\frac{\partial \mathbf{T}_h}{\partial \mathbf{x}_h}^\top , \left(\frac{\partial \mathbf{T}_s}{\partial \mathbf{T}_h} \frac{\partial \mathbf{T}_h}{\partial \mathbf{U}} \right)^\top \right]^\top . \tag{II.7}$$

The hinge was removed by applying $\mathbf{T}_h^{-1}$ on the control vertices of each training surface, before rigidly registering to a randomly selected surface, allowing for anisotropic scaling. In order to perform PCA on surface points as opposed to control vertices, the surface points $\mathbf{Q}$ corresponding to the control vertices $\mathbf{P}$ were calculated by $\mathbf{Q} = \mathbf{BP}$ where $\mathbf{B}$ is a matrix of Doo-Sabin basis functions at the centroid of each surface patch.

After performing PCA on the surface locations, each mode $\boldsymbol{\phi}_i$ was projected back into the control vertex space by $\boldsymbol{\psi}_i = \mathbf{B}^{-1}\boldsymbol{\phi}_i$. To reduce the parameter space, the first N_m modes constituting at least 95 % of the total variation were kept. The local control vertices of every valid shape $\mathbf{U}$ can then be approximated by a linear combination of the modes of variation,

$$\hat{\mathbf{U}} = \bar{\mathbf{U}} + \sum_{i=1}^{N_m} \mathbf{x}_{s,i} \boldsymbol{\psi}_i , \tag{II.8}$$

where $\mathbf{x}_s$ is the shape parameters and $\bar{\mathbf{U}}$ is the mean model. This transform is denoted $\mathbf{T}_{ssm}(\mathbf{x}_s)$.

Global transform

In order to align the model in the image space, we introduce a global transform allowing translation, anisotropic scaling, and rotation. The global transform is denoted $\mathbf{T}_g(\mathbf{x}_g)$ where $\mathbf{x}_g$ is the 9-degrees-of-freedom transform state vector.

Motion model

In order to capture the movement of the Atrio-Ventricular (AV) plane during the cardiac cycle, we introduce a motion model. The hinge and global transforms can be defined by three landmarks; valve center, tricuspid valve center, and the RV apex position. We model the trajectory $\mathbf{p}(t)$ of each of these landmarks as a simple linear motion

$$\hat{\mathbf{p}}(t) = \mathbf{p}_{ED} + \bar{\alpha}(t)(\mathbf{p}_{ES} - \mathbf{p}_{ED}), \tag{II.9}$$

where $\mathbf{p}_{ES}$ and $\mathbf{p}_{ED}$ are the landmark positions in the End Diastolic (ED) and End Systolic (ES) frames.

For each of the 14 MRI images used for statistical analysis, the landmarks $\mathbf{p}(t)$ were manually traced during the cardiac cycle and the coefficient $\alpha(t)$ was calculated by

$$\alpha(t) = \frac{(\mathbf{p}(t) - \mathbf{p}_{ED}) \cdot (\mathbf{p}_{ES} - \mathbf{p}_{ED})}{\|\mathbf{p}_{ES} - \mathbf{p}_{ED}\|^2}. \tag{II.10}$$

Each $\bar{\alpha}$ was then calculated as the mean of all training trajectories.

Complete model

The combined transform between a local point $\mathbf{q} = (u, v)$ on the surface to the global space is

$$\mathbf{T}(\mathbf{q}, \mathbf{x}) = \mathbf{T}_g(\mathbf{T}_s(\mathbf{T}_h(\mathbf{T}_{ssm}(\mathbf{x}_s), \mathbf{x}_h), \mathbf{q}), \mathbf{x}_g). \tag{II.11}$$

II.2.2 Segmentation

The method presented here is an application of a previously presented real-time volumetric segmentation framework [22], [27]. The segmentation is represented as a state estimation problem and solved with an extended Kalman filter with the following processing chain.

1. The model is initialized in the image by aligning it with manually identified landmarks.
2. Iteratively for each consecutive frame in the cardiac cycle, starting at ED,
   (a) The next state is predicted according to the motion model.
   (b) Edges are detected normal to the predicted surface location.
   (c) The prediction and edge detections are fused to form an updated state estimate.
   (d) The shape parameters are normalized to a plausible shape.
3. The previous iteration is repeated, iterating backwards in time.
4. Forwards and backwards iterations are fused, resulting in the final segmentation.

Following an approach previously applied to segmentation of the aortic root [28], we perform the whole processing cycle in two passes. First, the segmentation is performed using a learned prediction step and a restricted model allowing no local deformations, which results in a rough segmentation and tracking of the RV during the cardiac cycle. This result is then used as the motion model for the second pass, in which local model deformations are allowed, resulting in the final segmentation.

Initialization

The segmentation is initialized by manually identifying three landmarks in both ED and ES; RV apex, Pulmonary Valve (PV) center, and Tricuspid Valve (TV) center.

Based on the landmarks $\mathcal{L}_I = \{\mathbf{p}_{apex}, \mathbf{p}_{tv}, \mathbf{p}_{pv}\}$ in the image space, an initial alignment state $\mathbf{x}_0$ for the hinge and global transforms is calculated by aligning $\mathcal{L}_I$ with the corresponding landmarks $\mathcal{L}_M = \{\mathbf{q}_{apex}, \mathbf{q}_{tv}, \mathbf{q}_{pv}\}$ in the model space.

Prediction

The time domain dynamics of the model is controlled in the Kalman filter prediction step, similar to previous works [28]. We use a combination of the previous estimate $\hat{\mathbf{x}}_{k-1|k-1}$, $\hat{\mathbf{P}}_{k-1|k-1}$ and a regularization state $\hat{\mathbf{x}}_{0,k}$ to predict the next estimate by

$$\hat{\mathbf{x}}_{k|k-1} = \mathbf{A}\hat{\mathbf{x}}_{k-1|k-1} + (\mathbf{I}-\mathbf{A})\mathbf{x}_{0,k} \tag{II.12}$$

$$\hat{\mathbf{P}}_{k|k-1} = \mathbf{A}\hat{\mathbf{P}}_{k-1|k-1}\mathbf{A}^\top + \mathbf{Q}_k\,, \tag{II.13}$$

where $\mathbf{A}$ is a diagonal matrix specifying the regularization strength for each state and $\mathbf{Q}_k$ is the estimated prediction noise. The diagonal elements of $\mathbf{A}$ were chosen separately for translation, scaling, rotation and deformation states.

In the first pass, $\mathbf{x}_{0,k}$ is calculated using the initialization method described in section II.2.2 using the motion model landmark points described in II.2.1. In the second pass, $\mathbf{x}_{0,k}$ is the result of the first segmentation pass.

Edge detection

In order to drive the surface towards the image borders, edge detection is performed normal to the predicted surface at 650 evenly distributed points. Each local edge point $\mathbf{p}_l$ with associated unit normal $\mathbf{n}_l$ is transformed to the global space $\mathbf{p}_g$, $\mathbf{n}_g$, and the corresponding Jacobian matrix $\mathbf{J}_g$ is calculated by

$$\mathbf{p}_g = \mathbf{T}_g(\mathbf{p}_l; \hat{\mathbf{x}}) \tag{II.14}$$

$$\mathbf{n}_g = |\mathbf{M}|\left(\mathbf{M}^{-1}\right)^\top \mathbf{n}_l \text{ where } \mathbf{M} = \left.\frac{\partial \mathbf{T}_g(\mathbf{p};\mathbf{x})}{\partial \mathbf{p}}\right|_{\substack{\mathbf{p}_l \\ \hat{\mathbf{x}}}} \tag{II.15}$$

$$\mathbf{J}_g = \left.\frac{\partial \mathbf{T}}{\partial \mathbf{x}}\right|_{\substack{\mathbf{p}_l \\ \hat{\mathbf{x}}}} = \left[\frac{\partial \mathbf{p}}{\partial \mathbf{x}_g}, \frac{\partial \mathbf{p}}{\partial \mathbf{x}_h}, \frac{\partial \mathbf{p}}{\partial \mathbf{x}_s}\right], \tag{II.16}$$

where $\hat{\mathbf{x}} = \hat{\mathbf{x}}_{k|k-1}$ and

$$\frac{\partial \mathbf{p}}{\partial \mathbf{x}_g} = \frac{\partial \mathbf{T}_g(\mathbf{x}_g)}{\partial \mathbf{x}_g} \tag{II.17}$$

$$\frac{\partial \mathbf{p}}{\partial \mathbf{x}_h} = \frac{\partial \mathbf{T}_g(\mathbf{q})}{\partial \mathbf{q}} \frac{\partial \mathbf{T}_s(\mathbf{U})}{\partial \mathbf{U}} \frac{\partial \mathbf{T}_h(\mathbf{x}_h)}{\partial \mathbf{x}_h} \tag{II.18}$$

$$\frac{\partial \mathbf{p}}{\partial \mathbf{x}_s} = \frac{\partial \mathbf{T}_g(\mathbf{q})}{\partial \mathbf{q}} \frac{\partial \mathbf{T}_s(\mathbf{U})}{\partial \mathbf{U}} \frac{\partial \mathbf{T}_h(\mathbf{U})}{\partial \mathbf{U}} \frac{\partial \mathbf{T}_{ssm}(\mathbf{x}_s)}{\partial \mathbf{x}_s}, \tag{II.19}$$

due to the chain rule.

Edge displacements v_i are detected by searching along $\mathbf{n}_g$ around $\mathbf{p}_g$ using the least mean squares fit to an intensity step function. We use 40 samples with 1 mm spacing for each edge profile, resulting in a capture range of 4 cm. Outlier edges are rejected based on the intensity step height and differences between neighboring edges.

The edge points are grouped into 5 regions; Septum, posterior LV-RV attachment, posterolateral free wall, anterolateral free wall including the outflow tract and anterior LV-RV attachment, and base, as shown in figure II.3. Each group has different a priori uncertainties of the edge measurements, used to express the common appearance of RV 3DTTE images. The uncertainties are highest for the anterolateral free wall and lowest for the septum and posterolateral free wall.

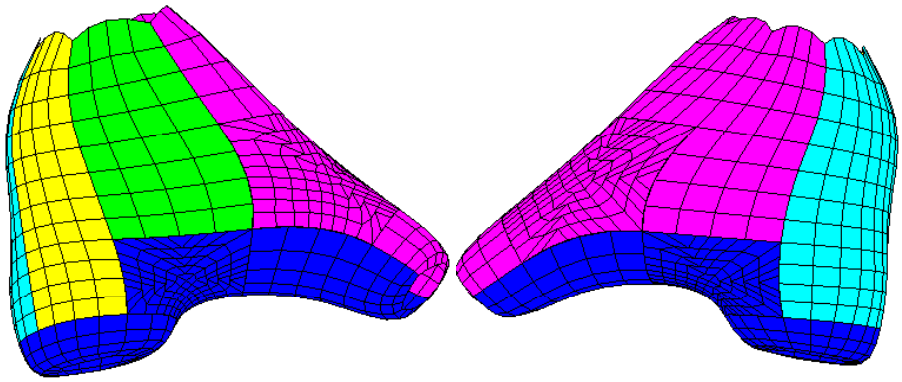

Figure II.3: Model regions as seen from medial (left) and lateral (right) sides; septum (green), posterior LV-RV attachment (yellow), posterolateral free wall (cyan), anterolateral free wall (magenta), and base (blue).

For each region k, each measured edge displacement $v_{k,i}$ has an associated measurement noise with estimated variance $r_{k,i}$. It is generally hard to properly estimate the variance $r_{k,i}$ of each edge profile in the ultrasound image. To simplify, we calculate the quality-of-fit $q_{k,i}$ for each edge profile as the sum of squared deviations in the intensity

fit. The variances are then normalized by

$$r_{k,i} = R_k q_{k,i} \sum_j \frac{1}{q_{k,j}} \tag{II.20}$$

such that the amount of measurement influence $\sum_i r_{k,i}^{-1} = R_k^{-1}$ is consistent across datasets, where R_k is the a priori variance of the edge detection of the k'th region.

State update

The update step in the Kalman filter fuses the previous estimate, state prediction, and detected edges. In order to speed up the calculations, the Kalman gain is simplified by assuming independent measurement noises [22]. With this simplification, the update step can be written as

$$\mathbf{h}_i^\top = \mathbf{n}_i^\top \mathbf{J}_i \tag{II.21}$$

$$\mathbf{P}_{k|k}^{-1} = \mathbf{P}_{k|k-1}^{-1} + \sum_i \mathbf{h}_i r_i^{-1} \mathbf{h}_i^\top \tag{II.22}$$

$$\hat{\mathbf{x}}_{k|k} = \hat{\mathbf{x}}_{k|k-1} + \mathbf{P}_{k|k} \sum_i \mathbf{h}_i r_i^{-1} v_i \,, \tag{II.23}$$

where $\hat{\mathbf{x}}_{k|k}$ and $\mathbf{P}_{k|k}^{-1}$ are the updated state and covariance matrix, and v_i, r_i, $\mathbf{n}_i$ and $\mathbf{J}_i$ are the edge displacement, edge noise variance, normal vector, and surface Jacobian matrix respectively.

This computation is efficient as it does not require inversion of matrices with size dependent on the number of measurements.

Normalization

The deformation states $\boldsymbol{\beta}$ were modeled as a multi-variate gaussian distribution,

$$M(\boldsymbol{\beta}) = \sum_{i=1}^{N_m} \frac{\beta_i^2}{\lambda_i} \sim \chi^2 \,. \tag{II.24}$$

To constrain the allowed deformation to plausable shapes, the deformation states $\boldsymbol{\beta}_{k|k}$ for which $M(\boldsymbol{\beta}_{k|k}) \geq M_t$ are projected onto the hyperellipsoid $M(\boldsymbol{\beta}_{k|k}) = M_t$ where M_t is the 95 % threshold of the χ^2 distribution according to normal SSM practice [29].

Kalman smoother

In order to prevent the segmentation from lagging behind the image borders and to regularize towards a cyclic volume curve, we apply Kalman smoothing by tracking forwards and backwards in time as previously described [28].

The Kalman filter is iterated forward over frames $k = 1, 2, \ldots, N$ to produce estimate $\mathbf{x}_{f,k}$ with estimated covariance $\mathbf{P}_{f,k}$. Backwards iteration over frames $k = N, N-1, \ldots, 1$

produces $\mathbf{x}_{b,k}$ and $\mathbf{P}_{b,k}$. The forward and backward state estimates are then assimilated by

$$\mathbf{P}_k = \left(\mathbf{P}_{f,k}^{-1} + \mathbf{P}_{b,k}^{-1}\right)^{-1} \tag{II.25}$$

$$\hat{\mathbf{x}}_k = \mathbf{P}_k\left(\mathbf{P}_{f,k}^{-1}\hat{\mathbf{x}}_{f,k} + \mathbf{P}_{b,k}^{-1}\hat{\mathbf{x}}_{b,k}\right). \tag{II.26}$$

II.2.3 Validation

Model

To ensure that the subdivision surface was able to represent the RV geometry with the limited degrees of freedom introduced in section II.2.1, the mean and maximum (Hausdorff) euclidean distances between all points on the manual endocardial contour and corresponding points on the fitted surface were calculated.

To further ensure that the subspace consisting of the selected modes of variation was suitable to represent the observed range of anatomies, a leave-one-patient-out statistical shape model reconstruction validation was performed. For each patient, the mean model parameters $\bar{\mathbf{x}}$ and modes of variation $\mathbf{\Phi}$ were constructed for the remaining 13 patients as described in section II.2.1, selecting the N_m modes constituting at least 95 % of the variation. For each surface of the unseen patient, the reconstructed surface was calculated using parameters

$$\hat{\mathbf{x}} = \bar{\mathbf{x}} + \mathbf{\Phi}\hat{\boldsymbol{\beta}}\,, \tag{II.27}$$

where $\hat{\boldsymbol{\beta}} = \arg\min_{\boldsymbol{\beta}} \left\|\hat{\mathbf{x}}(\boldsymbol{\beta}) - \mathbf{x}\right\|$ and $\mathbf{x}$ are the parameters of the unseen surface. The mean signed and unsigned euclidean distances between points on the unseen MRI traces and reconstructed surfaces were calculated, as well as the Hausdorff distances.

Segmentation

The segmentation was validated retrospectively on 3DTTE recordings of 17 patients with aortic insufficiency. The patient characteristics are given in table II.1. Segmentation quality was evaluated by comparing End Diastolic Volume (EDV), End Systolic Volume (ESV), Stroke Volume (SV) and Ejection Fraction (EF) between the proposed method and manual measurements in MRI, as well as a state-of-the-art commercial segmentation tool for 3DTTE (TomTec 4D RV-Function, version 2.0, TomTec Imaging Systems, Munich, Germany) with and without manual contour correction.

In addition, the following surface-surface distance metrics between the automated and manual 3DTTE segmentations were calculated: mean and median absolute distance, mean and median signed distance, and Hausdorff distance.

3DTTE acquisition 3DTTE recordings of the RV were acquired from an apical position. The probe was tilted slightly in order to get as much as possible of the RV into the sector. The images were recorded using ECG-gated multi-beat acquisitions under breath hold. All images were acquired on a Vivid E9 scanner using a 4V probe (GE Vingmed Ultrasound

Table II.1: Patient characteristics of the 17 clinical cases used for validation.

Age, yr	47 ± 15
Male, n	15 (88 %)
Weight, kg	84 ± 14
Height, cm	178 ± 9
LV hypertension, n	1 (6 %)
LV hypertrophy, n	10 (63 %)

AS, Horten, Norway). The mean temporal resolution and sector size were 28 ms and $63 \times 63°$ respectively. 15 recordings were acquired from 6 beats, and 2 recordings from 4 beats.

3DTTE automated segmentation The RV apex, pulmonary valve, and tricuspid valve were manually identified in ES and ED using a dedicated software. The proposed automated segmentation method was then run on the image without any further manual involvement.

3DTTE reference segmentation The TomTec 4D RV-Function software was used as a reference for RV assessment in 3DTTE. For each image, the analysis starts by manually identifying the following 10 landmarks in a dedicated software; mitral and tricuspid valve center, LV and RV apex, anterior and posterior RV-LV attachment points as well as medial and lateral RV endocardial border points in a single short axis slice, and two points spanning the aortic valve annulus. The software then automatically tracks the endocardial borders during the cardiac cycle and generates corresponding volume loops. After tracking, all contours can be manually adjusted. This software was run twice for each image, by an experienced cardiologist. Firstly, extensive manual contour corrections were performed to provide a ground-truth manual 3DTTE reference. Secondly, the tool was run without any manual interaction after initialization, in order to provide a comparable algorithmic reference for the proposed method.

MRI acquisition Magnetic resonance images were acquired with Siemens 1.5 tesla scanners (Siemens Avanto and Siemens Sonata; Siemens Medical Systems, Erlangen, Germany), using a breath-hold, prospectively ECG-triggered, segmented, balanced steady-state free precession gradient-echo cine sequence with minimum echo and repetition times. Slices were 6 mm thick with a 4 mm short-axis interslice gap, a spatial resolution of 1.9×1.3 mm, and a temporal resolution of 30-35 ms. Endocardial borders were traced manually at a PACS work station (Sectra Medical Systems AB, Linköping, Sweden). Right and left ventricular volumes and ejection fractions were calculated by short axis slice summation.

Statistical analysis

Statistical analysis was performed using MedCalc, version 15.2 (MedCalc Software, Ostend, Belgium). Correlation between measurements were assessed by the Intra-class Correlation Coefficient (ICC) using a two-way model with absolute agreement. Continuous variables are presented as mean ± SD.

Figure II.4: Example of manual segmentation in MRI short axis view.

II.3 Results

II.3.1 Model

For the 280 fitted MRI segmentations, the mean distance between the manual trace and fitted model was 1.8 ± 0.37 mm with a mean signed distance of 0.30 ± 0.12 mm and Hausdorff distance 7.6 ± 2.3 mm.

12 deformation modes were necessary to cover at least 95 % of the observed variation. The first modes of variation contained the expansion, elongation, and curvature around the LV, shown in figure II.5. The leave-one-patient-out reconstruction resulted in a surface-surface mean absolute distance error of 2.1 ± 0.4 mm, signed distance error 0.4 ± 0.4 mm, and Hausdorff distance 8.7 ± 3.0 mm.

II.3.2 Segmentation

All recordings were successfully segmented with computation time 2.0±0.33 s (53±4.1 ms per frame) on a standard laptop. The mean signed and unsigned surface-surface distances between the automated and 3DTTE reference segmentations were 0.5 ± 1.4 mm

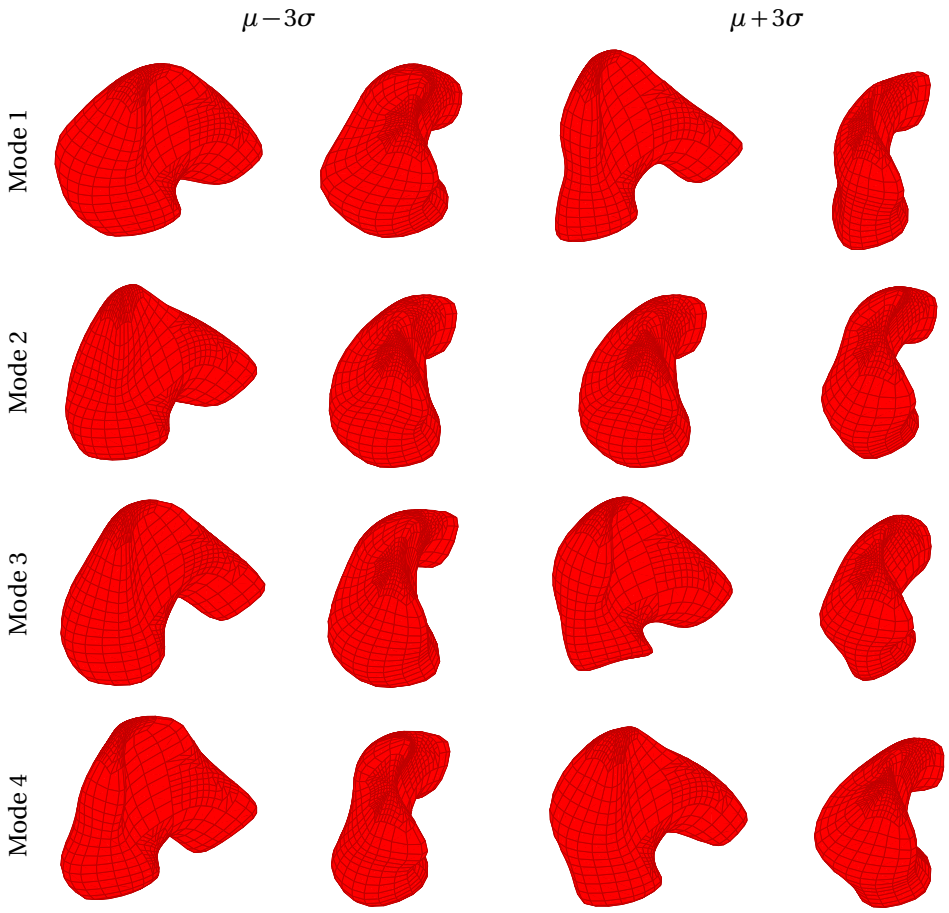

Figure II.5: The most dominant modes of variation of the statistical shape model.

and 3.6±0.7 mm respectively. The corresponding median surface-surface distances were 0.2 ± 0.7 mm and 3.0 ± 0.6 mm, and the Hausdorff distances were 11.6 ± 2.0 mm. A comparison of volumes and ejection fractions for all methods is reported in table II.2. Figures II.6 and II.7 show a BlandâĂŞAltman analysis, and clustering and agreement between the methods respectively. Example segmentations are shown in figures II.4 and II.8.

II.4 Discussion

Fitting the proposed subdivision surface to manual segmentations in MRI images for statistical shape analysis resulted in an acceptable residual distance between the fitted surface and manual trace, and an associated mean signed distance close to zero. Although this error could be reduced by increasing the number of control vertices of the RV model, this would come at the cost of reduced segmentation robustness. We conclude that the surface was a sufficiently accurate representation of the observed RV geometries, and the compact representation did not significantly restrict the expressivity of the surface. Furthermore, the statistical shape model using only 12 modes of variation was able to accurately represent the observed geometrical distribution in a leave-one-patient-out experiment.

The method achieved a Mean Absolute Distance (MAD) error of 3.6 mm and Hausdorff Distance (HD) of 11.6 mm. It is natural to compare this to to LV segmentation methods, where MAD and HD errors of about 2.3 mm and 8.5 mm have been reported for current state-of-the-art methods [33], including state-estimation approaches similar to the proposed method [34]. The noticeably higher surface errors illustrate how challenging the RV segmentation problem is in comparison to the LV, because of the increased shape complexity and reduced image quality. The majority of the surface error was observed in the RVOT region. This is where the image quality is poorest, and both the automated and manual segmentations are most uncertain. Additionally, the tool used to generate the reference segmentations has limited flexibility in editing the RVOT.

The observed HD of 11.6 mm is comparable to what was recently reported from the MICCAI'12 MRI RV segmentation challenge, where the lowest HD was 7.3 mm and 9.3 mm for two separate data sets [3]. Recently, Stebbing *et al.* [15] presented a RV segmentation method that, instead of using statistical shape information directly, performs segmentation simultaneously in either multiple images from different views of the same patient, or in images of multiple patients. The method achieved median signed trace-surface distances of about 1.5 mm (median over 4 cases) for multiple images of a single patient and 1.7 mm (median over 12 cases) for multiple patients. These error metrics are significantly lower than what was shown in our validation (3.0 mm mean). However, the metrics were based on traces in three short axis and two long axis slices which did not cover the RVOT. They are therefore not directly comparable to the surface-surface distances reported in our validation. Finally, our proposed method was significantly faster, requiring on average 2 s per patient compared to about 60 minutes for simultaneous segmentation of 12 patients.

The model contains a hinge transform used to capture differences in the RVOT orien-

Table II.2: Comparison between manual measurements in MRI, reference method in 3DTTE with and without manual contour correction, and the proposed method for EDV, ESV, SV and EF. Values are mean±SD (ICC). $^*p < 0.05$ by two-tailed Student's t-test. Negative values indicate an underestimation of the row relative to the column.

(a) End Diastolic Volume (mL)

	MRI	3DTTE reference (manual)	3DTTE reference (automatic)
Reference man.	-32.4 ± 36.3 (0.63)		
Reference auto.	$-58.8 \pm 40.6^*$ (0.39)	-26.4 ± 29.1 (0.67)	
Proposed	-25.8 ± 23.7 (0.79)	6.6 ± 29.7 (0.78)	$33.1 \pm 32.9^*$ (0.56)

(b) End Systolic Volume (mL)

	MRI	3DTTE reference (manual)	3DTTE reference (automatic)
Reference man.	$-28.4 \pm 28.6^*$ (0.54)		
Reference auto.	-23.3 ± 31.7 (0.52)	5.1 ± 24.0 (0.67)	
Proposed	-15.7 ± 25.5 (0.73)	12.7 ± 17.1 (0.80)	7.6 ± 29.1 (0.56)

(c) Stroke Volume (mL)

	MRI	3DTTE reference (manual)	3DTTE reference (automatic)
Reference man.	-4.0 ± 19.4 (0.54)		
Reference auto.	$-35.5 \pm 20.6^*$ (0.13)	$-31.5 \pm 17.3^*$ (0.26)	
Proposed	-10.0 ± 19.1 (0.38)	-6.0 ± 20.4 (0.42)	$25.5 \pm 17.8^*$ (0.22)

(d) Ejection Fraction (%)

	MRI	3DTTE reference (manual)	3DTTE reference (automatic)
Reference man.	4.8 ± 7.6 (0.39)		
Reference auto.	$-9.5 \pm 10.4^*$ (0.03)	$-14.3 \pm 8.5^*$ (0.03)	
Proposed	0.0 ± 10.1 (0.29)	-4.8 ± 6.9 (0.47)	$9.5 \pm 11.5^*$ (-0.10)

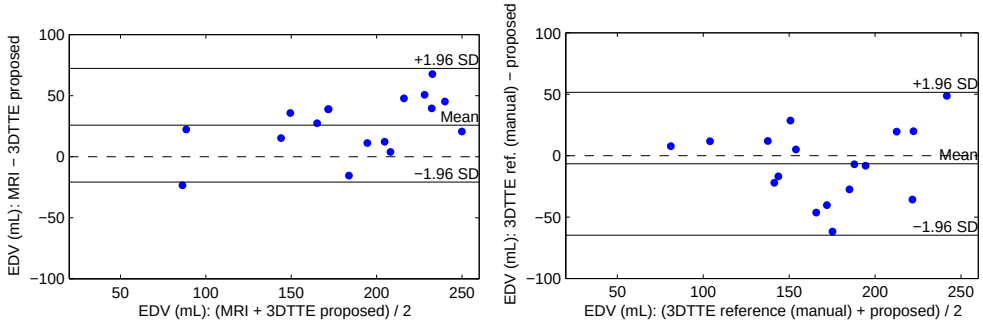

(a) End diastolic volume

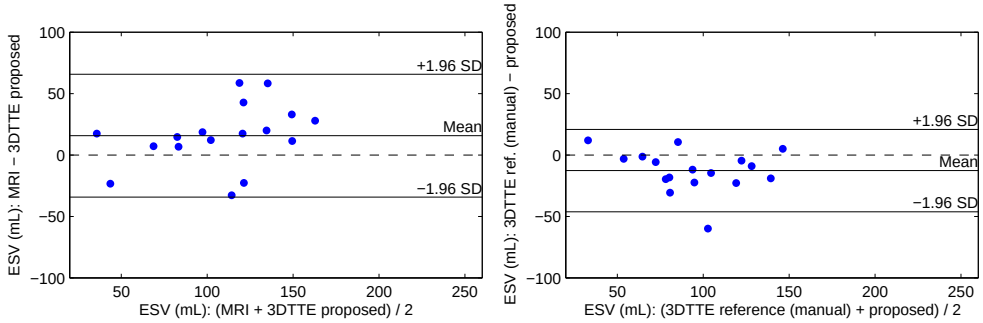

(b) End systolic volume

Figure II.6: End diastolic and end systolic volumes quantified by the proposed automated method in 3DTTE compared to MRI and 3DTTE reference (manual).

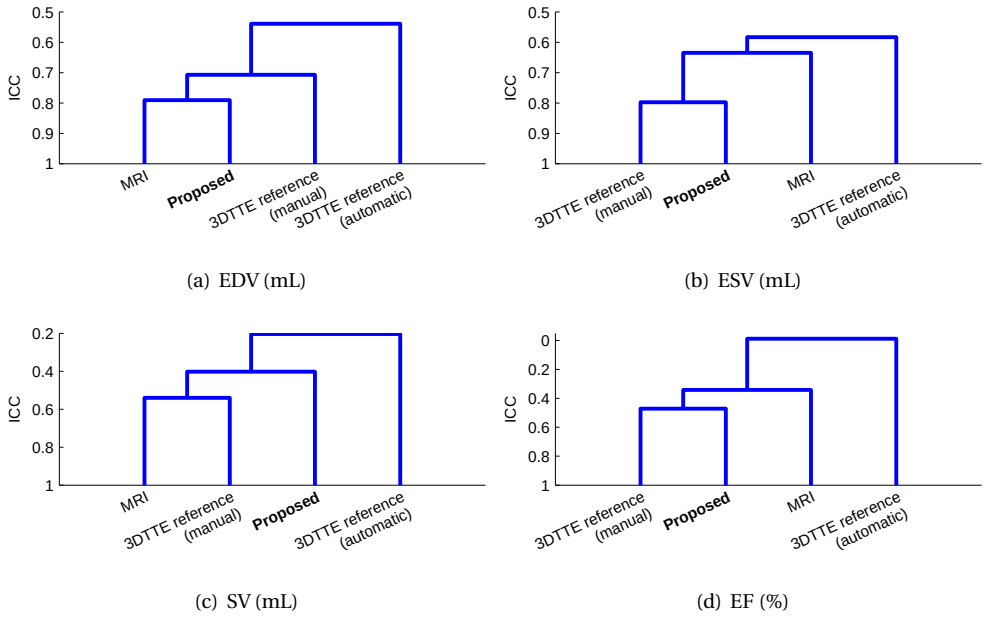

(a) EDV (mL)

(b) ESV (mL)

(c) SV (mL)

(d) EF (%)

Figure II.7: Dendrograms from agglomerative hierarchical clustering using average linkage [32] of Intra-class Correlation Coefficients (ICC) between manual measurements in MRI, reference method in 3DTTE with and without manual contour correction, and the proposed method.

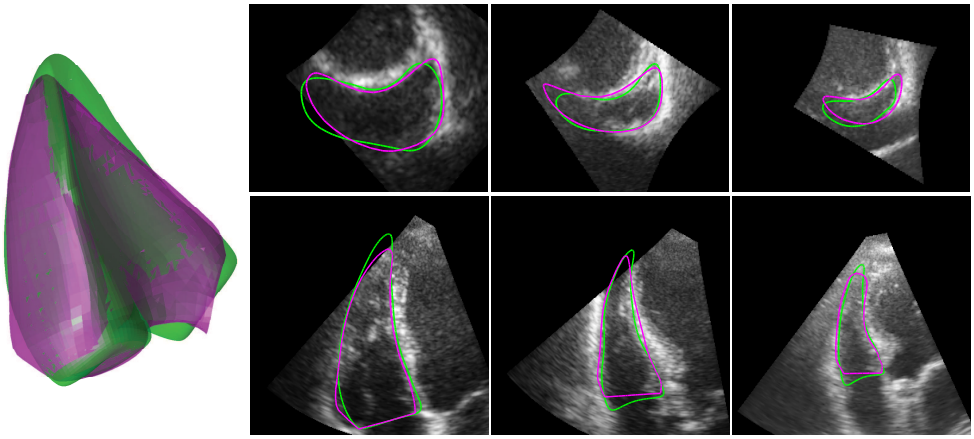

Figure II.8: Example of segmentation by the proposed method (green) compared to the manual reference (magenta). *Left:* Segmented meshes for a single case. *Right:* short axis (top) and long axis (bottom) planes for three different cases.

tation. This transform was not considered when building the statistical shape model, as PCA applied in euclidean space is generally not suited to capture rotational movement. This means that the model will lack deformation modes relating the RVOT orientation with RV shape. However, the hinge introduces the necessary degrees of freedom to place the pulmonary valve alignment landmark in a natural way, without any surface deformations. This is both desirable for the user, and results in a good initialization which is important for the Kalman filter driven segmentation.

We observed an underestimation with respect to MRI of the EDV, ESV and SV of both the manual 3DTTE reference and the proposed method, while the EF was unbiased for the proposed method and overestimated for the manual reference. This trend is consistent with results reported in the literature for manual and semi-automatic measurements, except for the manual EF which is typically slightly underestimated [21], [35]. Because of the large differences in methodology between TTE and MRI, perfect correlation should not be expected [17]. For instance, the RV volume in the proposed 3DTTE segmentation method is strictly bounded by the tricuspid and pulmonary valve planes. In contrast, using disk summation in MRI short axis slices, the volume is bounded by a slice approximately in the atrioventricular plane. Compared to TomTec 4D RV-Function without manual contour correction, the proposed method resulted in higher intra-class correlation coefficients and smaller biases compared to both MRI and 3DTTE reference for all quantification variables, EDV, ESV, SV and EF. In addition, the proposed method requires less manual user interaction; identification of 3 landmarks in two phases compared to 10 landmarks in a single phase.

Segmentation in ultrasound images is generally challenging, because of the low spatial resolution and the presence of artifacts such as dropouts, speckles and reverberations. For the RV in particular, the pulmonary valve, RVOT and anterolateral free wall is often acoustically shadowed by the sternum and lungs [21]. Furthermore, irregular trabeculations are typically very pronounced in the apical region of the RV [3]. Robustness of the segmentation method is therefore essential for solving this problem. The proposed RV surface model has a compact representation and inherently enforces regularization. By combining this with a statistical shape model we are mitigating problems related to edges disappearing due to acoustic shadowing or out of sector motion, by assuming in this region a statistically plausible shape, influenced by the general shape of the ventricle. The simple line search edge detectors are robust to noise in the ultrasound image, and because we combine several of them, we limit the impact of individual errors on the final segmentation. Similarly, using a strong prior geometry and motion model in the Kalman filter ensures a robust segmentation.

An echocardiography procedure is interactive in nature, and a computationally efficient method is therefore vital for wide-spread usage in clinical practice. The Kalman filter approach is very computationally efficient, with a mean computation time of 2.0 s. Further improvements could be made as the method lends itself to GPU parallelization.

In a clinical setting, it is important that the user is able to adjust the segmentation. The proposed framework naturally extends to user input, as manually annotated points and traces can be introduced as measurements (II.23). If these measurements are modeled with a low variance, the surface will interpolate the annotations and affect the segmenta-

tion during the whole cardiac cycle.

The effectiveness of the statistical shape model approach is dependent on the quality and quantity of the training data. In this study, we used a limited training set of only 14 patients. This can be justified by the fact that the training set contained patients with a variety of diseases. However, the method remains to be proven on different patient populations with diseases relevant to the RV.

A fundamental limitation to the statistical shape method is the inability of the surface model to adequately represent anatomies very different from what was observed in the training set. For some diseases, this problem can be mitigated by increasing the training set without any further changes in methodology. However, in some variations of structural congenital heart disease, such as double outlet right ventricle, the method proposed here is not directly suited, unless the disease is known prior to segmentation and a separate model and training set specific to the disease is used.

II.5 Conclusion

In this study an automated method for segmenting the right ventricle in 3D echocardiography has been described and validated against MRI and manual echocardiographic segmentation. The method is robust and computationally efficient, and resulted in good correlation with both MRI and manual 3DTTE reference in 17 clinical cases.

References

[1] L. L. Mertens and M. K. Friedberg, "Imaging the right ventricle - current state of the art," *Nature Reviews Cardiology*, vol. 7, pp. 551–563, 10 Oct. 2010.

[2] E. R. Valsangiacomo Buechel and L. L. Mertens, "Imaging the right heart: The use of integrated multimodality imaging," *European Heart Journal*, vol. 33, pp. 949–960, 8 2012.

[3] C. Petitjean, M. A. Zuluaga, W. Bai, J.-N. Dacher, D. Grosgeorge, J. Caudron, S. Ruan, I. B. Ayed, M. J. Cardoso, H.-C. Chen, D. Jimenez-Carretero, M. J. Ledesma-Carbayo, C. Davatzikos, J. Doshi, G. Erus, O. M. O. Maier, C. M. S. Nambakhsh, Y. Ou, S. Ourselin, C.-W. Peng, N. S. Peters, T. M. Peters, M. Rajchl, D. Rueckert, A. Santos, W. Shi, C.-W. Wang, H. Wang, and J. Yuan, "Right ventricle segmentation from cardiac mri: a collation study," *Medical Image Analysis*, vol. 19, pp. 187–202, 1 Jan. 2015.

[4] J. Peters, O. Ecabert, C. Meyer, H. Schramm, R. Kneser, A. Groth, and J. Weese, "Automatic whole heart segmentation in static magnetic resonance image volumes," in *Medical Image Computing and Computer-Assisted Intervention - MICCAI 2007*, ser. Lecture Notes in Computer Science, vol. 4792, Springer Berlin Heidelberg, 2007, pp. 402–410.

[5] M. S. ElBaz and A. S. Fahmy, "Active shape model with inter-profile modeling paradigm for cardiac right ventricle segmentation.," *Medical Image Computing and Computer-Assisted Intervention - MICCAI 2012*, vol. 15, pp. 691–8, Pt 1 Jan. 2012.

[6] Y. Ou, J. Doshi, G. Erus, and C. Davatzikos, "Multi-atlas segmentation of the cardiac mr right ventricle," in *Proceedings of 3D Cardiovascular Imaging: A MICCAI Segmentation Challenge*, (Nice, France), 2012.

[7] M. Zuluaga, M. Cardoso, M. Modat, and S. Ourselin, "Multi-atlas propagation whole heart segmentation from mri and cta using a local normalised correlation coefficient criterion," in *Functional Imaging and Modeling of the Heart*, ser. Lecture Notes in Computer Science, vol. 7945, Springer Berlin Heidelberg, 2013, pp. 174–181.

[8] W. Bai, W. Shi, H. Wang, N. Peters, and D. Rueckert, "Multi-atlas based segmentation with local label fusion for right ventricle mr images," in *Proceedings of 3D Cardiovascular Imaging: A MICCAI Segmentation Challenge*, (Nice, France), 2012.

[9] W. Bai, W. Shi, D. P. O'Regan, T. Tong, H. Wang, S. Jamil-Copley, N. S. Peters, and D. Rueckert, "A probabilistic patch-based label fusion model for multi-atlas segmentation with registration refinement: application to cardiac mr images.," *IEEE Transactions on Medical Imaging*, vol. 32, pp. 1302–15, 7 Jul. 2013.

[10] C. M. S. Nambakhsh, J. Yuan, K. Punithakumar, A. Goela, M. Rajchl, T. M. Peters, and I. B. Ayed, "Left ventricle segmentation in mri via convex relaxed distribution matching.," *Medical Image Analysis*, vol. 17, pp. 1010–24, 8 Dec. 2013.

[11] D. Grosgeorge, C. Petitjean, J.-N. Dacher, and S. Ruan, "Graph cut segmentation with a statistical shape model in cardiac mri," *Computer Vision and Image Understanding*, vol. 117, pp. 1027–1035, 9 Sep. 2013.

[12] C. W. Wang, C. W. Peng, and H. C Chen, "A simple and fully automatic right ventricle segmentation method for 4-dimensional cardiac mr images," in *Proceedings of 3D Cardiovascular Imaging: A MICCAI Segmentation Challenge*, (Nice, France), 2012.

[13] O. Maier, D. Jimenez, A. Santos, and M. Ledesma-Carbayo, "Segmentation of rv in 4d cardiac mr volumes using region-merging graph cuts," in *Computing in Cardiology*, 2012, pp. 697–700.

[14] E. D. Angelini, S. Homma, G. Pearson, J. W. Holmes, and A. F. Laine, "Segmentation of real-time three-dimensional ultrasound for quantification of ventricular function: a clinical study on right and left ventricles," *Ultrasound in Medicine & Biology*, vol. 31, pp. 1143–58, 9 Sep. 2005.

[15] R. V. Stebbing, A. I. Namburete, R. Upton, P. Leeson, and J. A. Noble, "Data-driven shape parameterization for segmentation of the right ventricle from 3D+t echocardiography," *Medical Image Analysis*, vol. 21, pp. 29–39, 1 2015.

[16] P. S. Niemann, L. Pinho, T. Balbach, C. Galuschky, M. Blankenhagen, M. Silberbach, C. Broberg, M. Jerosch-Herold, and D. J. Sahn, "Anatomically oriented right ventricular volume measurements with dynamic three-dimensional echocardiography validated by 3-tesla magnetic resonance imaging," *Journal of the American College of Cardiology*, vol. 50, pp. 1668–76, 17 Oct. 2007.

[17] G. Leibundgut, A. Rohner, L. Grize, A. Bernheim, A. Kessel-Schaefer, J. Bremerich, M. Zellweger, P. Buser, and M. Handke, "Dynamic assessment of right ventricular volumes and function by real-time three-dimensional echocardiography: a comparison study with magnetic resonance imaging in 100 adult patients," *Journal of the American Society of Echocardiography*, vol. 23, pp. 116–26, 2 Feb. 2010.

[18] H. B. van der Zwaan, W. a. Helbing, J. S. McGhie, M. L. Geleijnse, S. E. Luijnenburg, J. W. Roos-Hesselink, and F. J. Meijboom, "Clinical value of real-time three-dimensional echocardiography for right ventricular quantification in congenital heart disease: validation with cardiac magnetic resonance imaging," *Journal of the American Society of Echocardiography*, vol. 23, pp. 134–40, 2 Feb. 2010.

[19] A. M. Crean, N. Maredia, G. Ballard, R. Menezes, G. Wharton, J. Forster, J. P. Greenwood, and J. D. Thomson, "3d echo systematically underestimates right ventricular volumes compared to cardiovascular magnetic resonance in adult congenital heart disease patients with moderate or severe rv dilatation.," *Journal of Cardiovascular Magnetic Resonance*, vol. 13, p. 78, 1 Jan. 2011.

[20] A. Dragulescu, L. Grosse-wortmann, C. Fackoury, and L. Mertens, "Echocardiographic assessment of right ventricular volumes : a comparison of different techniques in children after surgical repair of tetralogy of fallot," *Journal of the American Society of Echocardiography*, pp. 596–604, 2012.

[21] E. Ostenfeld, M. Carlsson, K. Shahgaldi, A. Roijer, and J. Holm, "Manual correction of semi-automatic three-dimensional echocardiography is needed for right ventricular assessment in adults; validation with cardiac magnetic resonance," *Cardiovascular Ultrasound*, vol. 10, 1 Jan. 2012.

[22] F. Orderud, "A framework for real-time left ventricular tracking in 3d+t echocardiography, using nonlinear deformable contours and kalman filter based tracking," in *Computers in Cardiology, 2006*, IEEE, 2006, pp. 125–128.

[23] J. Hansegård, S. Urheim, K. Lunde, S. Malm, and S. Rabben, "Semi-automated quantification of left ventricular volumes and ejection fraction by real-time three-dimensional echocardiography," *Cardiovascular Ultrasound*, vol. 7, p. 18, 1 2009.

[24] J. Hansegård, F. Orderud, and S. I. Rabben, "Real-time active shape models for segmentation of 3d cardiac ultrasound," in *Computer Analysis of Images and Patterns*, ser. Lecture Notes in Computer Science, vol. 4673, Springer Berlin Heidelberg, 2007, pp. 157–164.

[25] K. Y. E. Leung, M. van Stralen, M. M. Voormolen, N. de Jong, A. F. W. van der Steen, J. H. C. Reiber, and J. G. Bosch, "Improving 3d active appearance model segmentation of the left ventricle with jacobian tuning," in *Proc. SPIE 6914, Medical Imaging 2008: Image Processing*, vol. 6914, 2008.

[26] B. Georgescu, X. Zhou, D. Comaniciu, and A. Gupta, "Database-guided segmentation of anatomical structures with complex appearance," in *Computer Vision and Pattern Recognition, 2005. IEEE Computer Society Conference on*, vol. 2, 2005, 429–436 vol. 2.

[27] F. Orderud and S. I. Rabben, "Real-time 3d segmentation of the left ventricle using deformable subdivision surfaces," in *Computer Vision and Pattern Recognition, 2008. IEEE Conference on*, Norwegian Univ. of Sci. & Technol., Trondheim, IEEE, Jun. 2008.

[28] J. Bersvendsen, J. O. Beitnes, S. Urheim, S. Aakhus, and E. Samset, "Automatic measurement of aortic annulus diameter in 3-dimensional transoesophageal echocardiography.," *BMC Medical Imaging*, vol. 14, 1 Sep. 2014.

[29] T. Heimann and H.-P. Meinzer, "Statistical shape models for 3d medical image segmentation: a review," *Medical Image Analysis*, vol. 13, pp. 543–63, 4 Aug. 2009.

[30] P. Radau, Y. Lu, K. Connelly, G. Paul, A. J. Dick, and G. A. Wright, "Evaluation framework for algorithms segmenting short axis cardiac mri," *The MIDAS Journal - Cardiac MR Left Ventricle Segmentation Challenge*, vol. 7, 2009.

[31] C. Swingen, R. T. Seethamraju, and M. Jerosch-Herold, "An approach to the three-dimensional display of left ventricular function and viability using mri," *The international journal of cardiovascular imaging*, vol. 19, pp. 325–36, 4 Aug. 2003.

[32] J. Røislien and E. Samset, "A non-parametric permutation method for assessing agreement for distance matrix observations," *Statistics in Medicine*, vol. 33, pp. 319–329, 2 2014.

[33] D. Barbosa, D. Friboulet, J. D'hooge, and O. Bernard, "Fast tracking of the left ventricle using global anatomical affine optical flow and local recursive block matching," *The MIDAS Journal*, Oct. 2014.

[34] E. Smistad and F. Lindseth, "Real-time tracking of the left ventricle in 3d ultrasound using kalman filter and mean value coordinates," *The MIDAS Journal*, Oct. 2014.

[35] Y. J. Shimada, M. Shiota, R. J. Siegel, and T. Shiota, "Accuracy of right ventricular volumes and function determined by three-dimensional echocardiography in comparison with magnetic resonance imaging: a meta-analysis study," *Journal of the American Society of Echocardiography*, vol. 23, pp. 943–53, 9 Sep. 2010.

Paper IV

Robust Spatio-Temporal Registration of 4D Cardiac Ultrasound Sequences

Proc. SPIE 9790, Medical Imaging 2016: Ultrasonic Imaging and Tomography

Jørn Bersvendsen [1,2,3], Matthew Toews [4], Adriyana Danudibroto [1,5], William M. Wells III [6], Raúl San José Estépar [6], Stig Urheim [7] and Eigil Samset [1,2,3]

[1]GE Vingmed Ultrasound AS, Horten, Norway
[2]Dept. of Informatics, University of Oslo, Oslo, Norway
[3]Center for Cardiological Innovation, Oslo, Norway
[4]École de Technologie Supérieure, Montreal, Canada
[5]University of Leuven, Leuven, Belgium
[6]Brigham and Women's Hospital, Harvard Medical School, Boston, USA
[7]Oslo University Hospital, Oslo, Norway

Abstract

Registration of multiple 3D ultrasound sectors in order to provide an extended field of view is important for the appreciation of larger anatomical structures at high spatial and temporal resolution. In this paper, we present a method for fully automatic spatio-temporal registration between two partially overlapping 3D ultrasound sequences. The temporal alignment is solved by aligning the normalized cross correlation-over-time curves of the sequences. For the spatial alignment, corresponding 3D Scale Invariant Feature Transform (SIFT) features are extracted from all frames of both sequences independently of the temporal alignment. A rigid transform is then calculated by least squares minimization in combination with random sample consensus. The method is applied to 16 echocardiographic sequences of the left and right ventricles and evaluated against manually annotated temporal events and spatial anatomical landmarks. The mean distances between manually identified landmarks in the left and right ventricles after automatic registration were (mean ± SD) 4.3 ± 1.2 **mm compared to a ground truth error of** 2.8 ± 0.6 **mm with manual registration. For the temporal alignment, the absolute errors in valvular event times were** 14.4 ± 11.6 **ms for Aortic Valve (AV) opening,** 18.6 ± 16.0 **ms for AV closing, and** 34.6 ± 26.4 **ms for mitral valve opening, compared to a mean inter-frame time of 29 ms.**

IV.1 Introduction

Ultrasound is the image modality of choice for assessing the heart in clinical routine, offering high frame rate imaging of the beating heart. As 3D ultrasound is being more widely studied, new applications for imaging, visualization and quantification of the heart are emerging.

Registration of 3D ultrasound images has many potential uses, including motion estimation and extended field of view. Several methods have been proposed using elastic registration to study the motion of the heart walls, which can be used to estimate the strain in the myocardium [1]–[4]. As 3D ultrasound images are typically acquired in smaller sectors, to maintain adequate spatial and temporal resolution, registration can be used to fuse multiple 3D sectors together. This extends the field of view, allowing the quantification of larger structures while preserving resolution. Methods for spatial registration of 3D ultrasound include optical flow [5], feature-registration such as Scale Invariant Feature Transform (SIFT) [6], voxel-wise similarity measures such as Normalized Cross-Correlation (NCC) [7], and similarity measures based on local orientation and phase [8].

Ni *et al.* used 3D SIFT features to create a panorama image from several 3D ultrasound images by rigid registration [6]. This work was extended by Schneider *et al.* who used efficient rotation-variant features to provide a transform between consecutive frames in real-time during acquisition [9]. This can be useful for compensating for slight movement of the probe during acquisition, or to cancel movement of anatomy.

Because the heart undergoes a complex contraction that is non-linear with respect to changes in the heart rate, establishing a temporal correspondence between sequences is important for accurate registration. Temporal registration for cardiac images often relies heavily on external recording from ECG. Utilizing image based measurement allows the registration to be independent from this external measurement.

Perperidis *et al.* used Normalized Cross Correlation (NCC) over time for temporal alignment and normalized mutual information for spatial alignment to provide a free-form spatio-temporal registration between MRI sequences [10]. Expanding on this, Zhang *et al.* used a similar approach for 3D ultrasound to MRI registration, using NCC over time for temporal alignment and 3D SIFT features for spatial alignment [11].

There are many aspects of ultrasound image processing that present challenges compared to other medical imaging modalities. Ultrasound often contain artifacts such as acoustic shadows, speckles, and reverberations. This means that several of the intensity-based matching methods used for registering images of other modalities are less appropriate for ultrasound processing. Furthermore, acquisitions can have very different gain settings, temporal and spatial resolutions, and can be acquired from different locations depending on the patient, in order to improve the acoustic window.

In this paper we present a method of registering two partially overlapping 3D cardiac ultrasound sequences in space and time. The main contribution of this work is to solve both the spatial and temporal alignment problems for 4D ultrasound, and to solve the spatial alignment with no user interaction and without any a priori assumptions on either the temporal or spatial alignment of the sequences. The temporal alignment is solved by aligning the NCC-over-time functions of the floating and reference sequences. We then use corresponding 3D SIFT features between all frames, without any assumptions on the temporal alignment, to extract a single rigid transform for the whole cardiac cycle by minimizing a least squares problem using Random Sample Consensus (RANSAC). The method was validated by registering 3D sectors of the left and right ventricles in 16 clinical cases.

IV.2 Methods

Given a reference image sequence [

$$\mathcal{I}_r(x,y,z,t) = \left\{ I_{r,i}(x,y,z) \right\}, \tag{IV.1}$$

and a floating sequence

$$\mathcal{I}_f(x,y,z,t) = \left\{ I_{f,i}(x,y,z) \right\}, \tag{IV.2}$$

the objective of the registration method is to find a transform $\mathcal{T}$ such that any voxel in the transformed sequence $\mathcal{T}\left(\mathcal{I}_f\right)$ coincides with the corresponding voxel in $\mathcal{I}_r$.

Following the approach used by others [10], [11], we decouple the registration problem into spatial and temporal domains and solve these separately. We first solve the temporal alignment using the NCC over the cardiac cycle, before extracting a spatial transform from 3D SIFT feature correspondences between all frames.

IV.2.1 Temporal Registration

The heart undergoes a complex contraction during the cardiac cycle. Because this contraction is slightly different for each beat and non-linear with changes of heart frequency, different acquisitions will generally not be synchronized, even if performed within a relatively short period of time without external influences.

The NCC over time has been shown to be a characteristic function describing the events of the cardiac cycle in a consistent manner, and has been used for temporal alignment of MRI sequences [10] and between ultrasound and MRI [11]. In both of these studies, the temporal alignment was achieved by first detecting key cardiac events in the NCC-over-time function, which involves calculating its second order derivative.

However, our experiments indicate that the second order derivation is unstable in ultrasound images of high frame rate, because of the inherently low signal-to-noise ratio and the presence of artifacts such as acoustic shadows, speckles and reverberations. This is specially apparent for images of the right ventricle which generally has lower image quality than the left ventricle, due to the challenging acquisition [12]. We therefore propose to solve the temporal registration by aligning the NCC-over -time functions with an optimization problem.

The temporal transform $\mathcal{T}_{\text{temporal}}$ is modeled as a linear global transform $\mathcal{T}^{\text{global}}_{\text{temporal}}(t) = \alpha t + \beta$ used to scale the sequences to the same length and compensate for global phase shift, and a local transform $\mathcal{T}^{\text{local}}_{\text{temporal}}(t)$ used to adjust for non-linear difference in the contraction pattern of the sequences. The local transform is modeled as a 1D B-spline

$$\mathcal{T}^{\text{local}}_{\text{temporal}}(t) = \sum_{i=1}^{N_t} b_i\left(\frac{t}{T}\right)\tau_i\,, \tag{IV.3}$$

where T is the length of the sequence, and b_i and τ_i are the B-spline basis functions and control time displacements respectively. The combined transform is given by

$$\mathcal{T}_{\text{temporal}}(t) = \mathcal{T}^{\text{local}}_{\text{temporal}}(t) + \mathcal{T}^{\text{global}}_{\text{temporal}}(t)\,. \tag{IV.4}$$

The control time displacements τ_i of the local temporal deformation are calculated by solving the minimization problem

$$\tau = \arg\min_{\tau} \left| f_r(t) - f_f\left(\mathcal{T}_{\text{temporal}}(t)\right)\right|^2\,, \tag{IV.5}$$

where f_r and f_f are the NCC functions of the reference and floating sequences. The optimization problem is solved numerically by sequential quadratic programming. By constraining $\mathcal{T}_{\text{temporal}}$ to be monotonically increasing, we guarantee that the frame order remains unchanged.

Because 3D cardiac ultrasound is gated by electrocardiography in almost all clinical cases, all image sequences were ordered such that the first frame corresponded to the QRS complex. We therefore assumed a zero phase shift, $\beta = 0$ in $\mathcal{T}^{\text{global}}_{\text{temporal}}$. Figure IV.1 shows the NCC functions before and after temporal alignment in an example case.

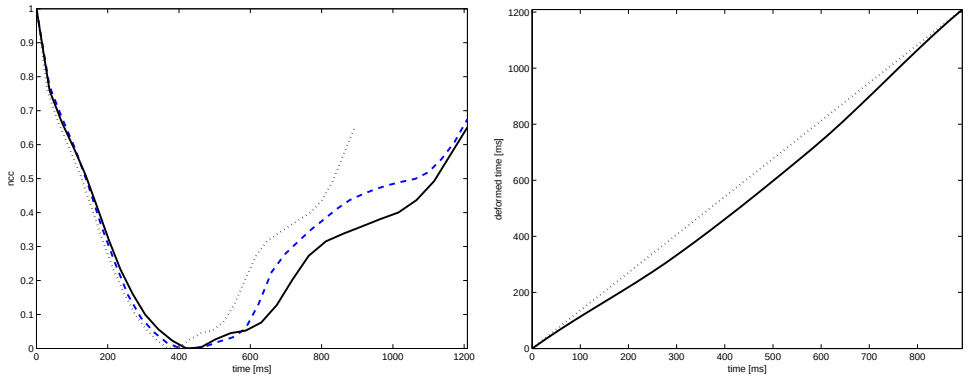

(a) (b)

Figure IV.1: The normalized cross-correlation over time for a reference (dashed) and floating sequence before (dotted) and after (solid) temporal alignment (a), resulting temporal registration (b).

IV.2.2 Time-Independent Spatial Registration

When registering sequences of the same patient during the same exam without external influences, it is fair to assume that the true spatial transform between the sectors of two ultrasound sequences is rigid and constant over the cycle. The spatial transform between frames of the reference and floating sequences $\mathcal{I}_r$ and $\mathcal{I}_f$ at similar points in the cardiac cycle can thus be assumed to be approximately rigid. This assumption leads a novel time-independent feature-based alignment (FBA) method [13], involving 3D SIFT feature extraction and matching.

First, a set of position-scale pairs $\{\mathbf{p}_i, \sigma_i\}$ are extracted in all 3D image frames of each sequence by identifying local maxima and minima of the difference-of-Gaussian function,

$$\{\mathbf{p}_i, \sigma_i\} = \text{local}\arg\max_{\mathbf{p},\sigma} \left| f(\mathbf{p}, \kappa\sigma) - f(\mathbf{p}, \sigma) \right| \tag{IV.6}$$

where $f(\mathbf{p}, \sigma)$ is the convolution of the image with a Gaussian kernel of variance σ^2 and κ the scale sampling rate. Following detection, an orientation is assigned to each feature using local gradient orientation information, and finally an appearance descriptor is generated from the patch of voxels within the image region defined by $(\mathbf{p}_i, \sigma_i)$. Appearance descriptors are normalized according to image intensity and local geometry, and can thus be used to compute image-to-image correspondences in a manner invariant to monotonic intensity shifts and global similarity transforms.

For time-independent matching, each sequence is modeled as an unordered bag of features with spatial but no temporal information. The FBA method [13] is then used to estimate a set of highly probable sequence-to-sequence feature correspondences. Briefly, a set of nearest-neighbor feature correspondences are identified based on the $\mathcal{L}_2$ distance

between appearance descriptors, resulting in a set of corresponding feature positions $\mathcal{C} = \{\mathbf{p}_{f,i}, \mathbf{p}_{r,i}\}$. We then apply RANSAC to solve the minimization problem

$$\mathcal{T}_{\text{spatial}} = \arg\min_{\mathcal{T}_{\text{spatial}}} \sum_i \left|\left|\mathbf{p}_{r,i} - \mathcal{T}_{\text{spatial}}(p_{f,i})\right|\right|^2, \tag{IV.7}$$

while simultaneously rejecting outlier correspondences.

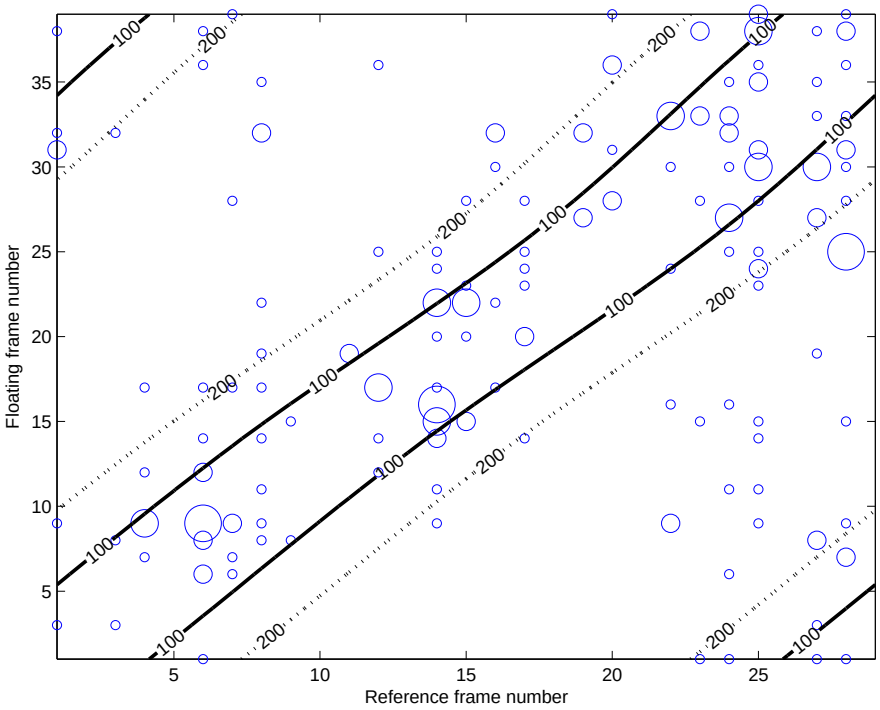

Figure IV.2: Correspondence density of feature matching between all reference and floating frames in one case. The size of each circle is proportional to the number of correspondences for a single frame pair. The black lines are contour lines of the time displacement, in milliseconds, after temporal alignment, illustrating the deformable temporal alignment.

IV.3 Validation

The registration method was evaluated on 3D transthoracic echocardiographic studies of 16 clinical cases of patients with aortic insufficiency. Each case had two acquisitions showing the left and right ventricles in different sectors with varying degree of overlap,

both acquired from an apical position. All images were recorded on a Vivid E9 scanner using a 4V-D transducer (GE Vingmed Ultrasound AS, Horten, Norway). Each sequence contained a single heart cycle acquired using multi-beat during breath hold, containing on average 38 frames.

The Mitral Valve (MV) and Aortic Valve (AV) opening and closing events were manually tagged for each recording by an experienced cardiologist. Anatomical landmarks were identified in the MV opening and MV closing frames. These included the AV, MV and Tricuspid Valve (TV) center points, and the AV-MV junction.

IV.4 Results

IV.4.1 Temporal alignment

The signed temporal alignment error between the key cardiac events were (mean ± SD) 4.9 ± 18.2 ms for AV opening, -2.0 ± 24.9 ms for AV closing and -5.9 ± 44.0 ms for MV opening. The corresponding absolute errors were 14.4 ± 11.6 ms, 18.6 ± 16.0 ms, and 34.6 ± 26.4 ms. For reference, the inter-frame time was 29 ± 5.1 ms.

IV.4.2 Spatio-temporal alignment

The average euclidean distance between corresponding manually identified anatomical landmarks under the automatic registration was 4.3 ± 1.2 mm, compared to an average distance of 2.9 ± 0.7 mm under a ground truth Procrustes alignment between all manual landmarks.

Figure IV.1(a) shows an example of the NCC curves before and after the temporal alignment, as well as the resulting temporal transform. Figure IV.1(b) illustrates the densities of 3D SIFT correspondences across the cardiac cycle. It is clear that, although no assumption is made on the temporal alignment, correspondences are more frequent in temporally aligned frames. Finally, examples of the resulting spatio-temporal alignment are shown in figure IV.3.

IV.5 Discussion

In this paper, a spatio-temporal registration method for 3D cardiac image sequences has been presented and evaluated on ultrasound images. The method performed close to manual registration in both time and space, while requiring no manual user input.

The temporally aligned valve events were all close to the ground truth, and within clinically acceptable values. The temporal errors were noticeably larger for the MV opening event compared to AV opening and closing, which is expected as MV opening is the last valvular event in the cardiac cycle and thus furthest from the ECG-gated first frame. For the spatial alignment, the aligned anatomical landmarks were close to the ground truth,

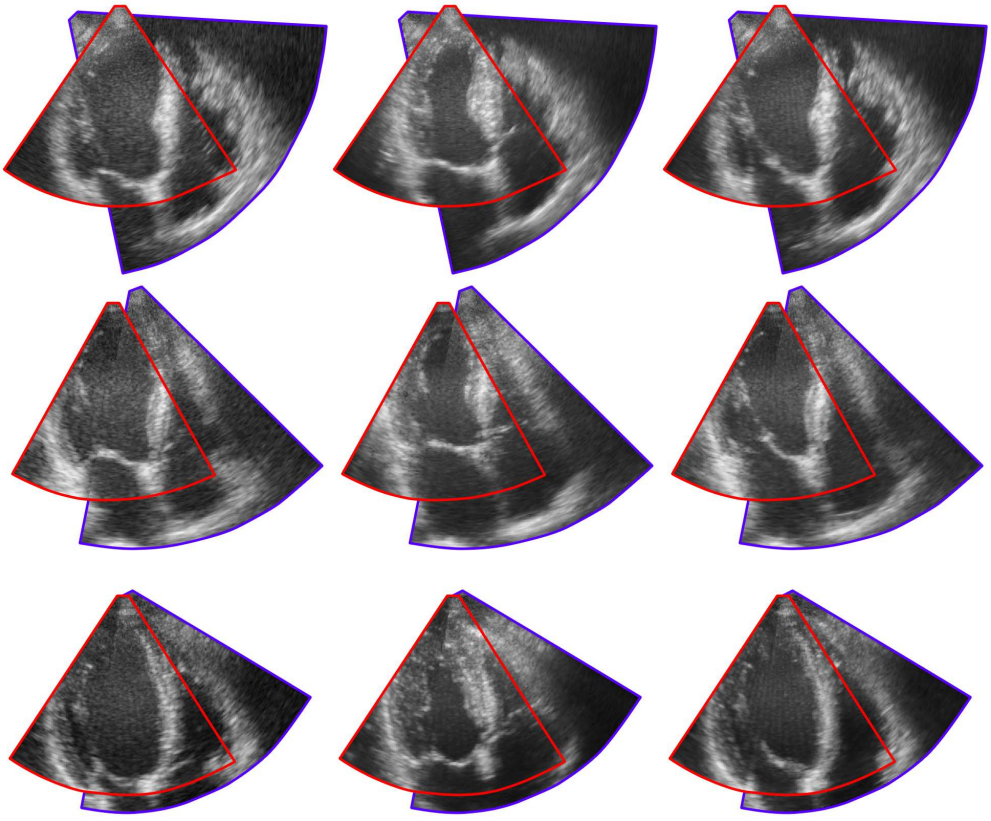

Figure IV.3: Resulting rigid registration for three sequences across the cardiac cycle. Each row three frames from a single case throughout the cardiac cycle.

and comparable to values reported by others for similar feature-based ultrasound to MRI registration [11].

Our experiments indicate that even with near perfect temporal alignment, a rigid transform between 3D SIFT feature correspondences of temporally aligned frame pairs was not robust in all cases. However, by combining all correspondences across the cardiac cycle in a time-independent manner and utilizing the assumption that inter-frame deformations are negligible, the registration was highly robust and accurate in all cases, despite the deformable contraction of the heart. This usage of correspondences can be justified by the following considerations: Firstly, the extracted features inherently contain some temporal information, as feature scale and appearances tend to fade in and out of existence at certain parts of the cardiac cycle. This can be seen in fig. IV.2, as the majority of the feature correspondences are found on temporally aligned frames. Secondly, although some spurious matches between unrelated points in the cardiac cycle will arise, they will bear no spatial consistency. Furthermore, as the heart's motion is cyclical, feature correspondences between deformed points during contraction will tend to be canceled out when the heart relaxes. Finally, by employing RANSAC and least squares optimization, we are estimating a rigid transform in a very robust manner.

One of the strengths of the presented method is that it requires no prior information on the spatial relationship between the acquisitions. This means that the method could be used for registering different views, such as apical, parasternal or subcostal, allowing the sonographer maximum freedom to find the best acoustic window.

References

[1] M. Ledesma-Carbayo, J. Kybic, M. Desco, A. Santos, M. Suhling, P. Hunziker, and M. Unser, "Spatio-temporal nonrigid registration for ultrasound cardiac motion estimation," *IEEE Transactions on Medical Imaging*, vol. 24, pp. 1113–1126, 9 2005.

[2] A. Elen, H. F. Choi, D. Loeckx, H. Gao, P. Claus, P. Suetens, F. Maes, and J. D'hooge, "Three-dimensional cardiac strain estimation using spatio-temporal elastic registration of ultrasound images: A feasibility study," *IEEE Transactions on Medical Imaging*, vol. 27, pp. 1580–1591, 11 2008.

[3] G. Kiss, D. Barbosa, K. Hristova, J. Crosby, F. Orderud, P. Claus, B. Amundsen, D. Loeckx, J. D'hooge, and H. Torp, "Assessment of regional myocardial function using 3d cardiac strain estimation: Comparison against conventional echocardiographic assessment," in *Ultrasonics Symposium (IUS), 2009 IEEE International*, 2009, pp. 507–510.

[4] M. De Craene, G. Piella, O. Camara, N. Duchateau, E. Silva, A. Doltra, J. D'hooge, J. Brugada, M. Sitges, and A. F. Frangi, "Temporal diffeomorphic free-form deformation: application to motion and strain estimation from 3d echocardiography.," *Medical Image Analysis*, vol. 16, pp. 427–50, 2 Feb. 2012.

[5] A. Danudibroto, O. Gerard, M. Alessandrini, O. Mirea, J. D'hooge, and E. Samset, "3d farnebäck optic flow for extended field of view of echocardiography," in *Functional Imaging and Modeling of the Heart*, ser. Lecture Notes in Computer Science, vol. 9126, Springer International Publishing, 2015, pp. 129–136.

[6] D. Ni, Y. Qu, X. Yang, Y. P. Chui, T.-T. Wong, S. S. M. Ho, and P. A. Heng, "Volumetric ultrasound panorama based on 3d sift," in *Medical Image Computing and Computer-Assisted Intervention - MICCAI 2008*, ser. Lecture Notes in Computer Science, vol. 5242, Springer Berlin Heidelberg, 2008, pp. 52–60.

[7] H. W. Mulder, M. van Stralen, H. B. van der Zwaan, K. Y. E. Leung, J. G. Bosch, and J. P. W. Pluim, "Multiframe registration of real-time three-dimensional echocardiography time series," *Journal of Medical Imaging*, vol. 1, p. 014 004, 1 2014.

[8] V. Grau, H. Becher, and J. A. Noble, "Registration of multiview real-time 3-d echocardiographic sequences," *IEEE Transactions on Medical Imaging*, vol. 26, pp. 1154–1165, 9 2007.

[9] R. J. Schneider *et al.*, "Real-time image-based rigid registration of three-dimensional ultrasound.," *Medical Image Analysis*, vol. 16, pp. 402–14, 2 Feb. 2012.

[10] D. Perperidis, R. H. Mohiaddin, and D. Rueckert, "Spatio-temporal free-form registration of cardiac mr image sequences," *Medical Image Analysis*, vol. 9, pp. 441 – 456, 5 2005.

[11] W. Zhang, J. A. Noble, and J. M. Brady, "Spatio-temporal registration of real time 3d ultrasound to cardiovascular mr sequences," in *Medical Image Computing and Computer-Assisted Intervention - MICCAI 2007*, ser. Lecture Notes in Computer Science, vol. 4791, Springer Berlin Heidelberg, 2007, pp. 343–350.

[12] E. R. Valsangiacomo Buechel and L. L. Mertens, "Imaging the right heart: The use of integrated multimodality imaging," *European Heart Journal*, vol. 33, pp. 949–960, 8 2012.

[13] M. Toews and W. M. Wells III, "Efficient and robust model-to-image alignment using 3d scale-invariant features," *Medical Image Analysis*, vol. 17, pp. 271–282, 3 2013.